Design and Implementation of Processes and Components for Optical Beam Forming Networks

Design and Implementation of Processes and Components for Optical Beam Forming Networks

By Dylan E. Genuth-Okon,

A Thesis Submitted to the School of Graduate Studies in the Partial Fulfillment of the Requirements for the Degree Master of Applied Science

McMaster University

Master of Applied Science (2023)

Hamilton, Ontario (Department of Engineering Physics)

TITLE: Design and Implementation of Processes and Components for Optical Beam Forming Networks

AUTHOR: Dylan E. Genuth-Okon (McMaster University)

SUPERVISOR: Dr. Andrew P. Knights

NUMBER OF PAGES: xvii, 121

Abstract

Optical beamforming networks (OBFNs) are a strong contender for phased array operation, especially using microwave photonics (MWP), with advantages in size, weight, power efficiency and cost. Applications for such systems range from satellite to cellphone communication. The use of OBFNs require multiple components to up-convert, down-convert and process radio frequency (RF) signals in the optical domain. In this thesis, these components and a photonic packaging solution were designed and tested. For the OBFN itself, the modulation for up-conversion was performed with a micro-ring modulator, which was able to perform 1.11 V forward bias modulation at 500 MHz with a modulation depth of 21 dB. A true time delay optical ring resonator (ORR) was designed and characterized, yielding 784 ps delay at 3.33 V heater bias, tunable to any value below this. An accessible, low-cost photonic packaging approach was developed, which achieved an optical coupling loss of 2.8 dB per facet. In conjunction with the photonic packaging was an electromagnetic interference (EMI) enclosure, which was able to block unwanted external RF signals.

Acknowledgements

Firstly, of course, I would like to thank my supervisor, Dr. Andrew Knights. He has given me the chance to work in his research group since my 2^{nd} year, almost 7 years ago, and gave me the chance to show what I had to offer. I learned so much from all the projects throughout the years, and had the chance to partake in so many opportunities, this thesis only covers the final 2 of those years.

CMC Microsystems and the SiEPIC program are to be thanked for making photonics accessible. CMC makes fabrication possible for students like me, giving us real-world experience on actual software and chips from foundries. SiEPIC courses managed by Dr. Lukas Chrostowski, this program and the textbook it follows are extremely useful.

I would like to thank my friends and colleagues in the Knights group, Arthur Méndez-Rosales, Michael Gao, Ranjan Das, Yanran Xie, Keru Chen, Gregory Thomas, and Feng Guo. I have fond memories of us preparing for group meetings, complaining about lab equipment, and doing measurements together. Special thanks go to Yu Jiang and Xin Xin, who have helped with some photonic packaging development and optical measurements respectively. Thanks also go to Doris Stevanovic for her help whenever needed.

Thanks to the "Grad Lads", Arthur, Jay and Colin, who have also chosen the path of most resistance. Thanks to the Engineering Graduate Society as well, being part of it really has added to my first year in graduate school.

Thank you to Claudia, changing my life for the better, and making me excited for the future.

Finally, I would like to thank my dad, my brother, and my step-mom, for always being there for me and having a place for me to call home.

Contents

List of Figures

List of Tables

List of Abbreviations and Symbols

APD Avalanche Photodetector

BOX Buried Oxide

CAD Computer-aided Design

CMOS Complementary Metal-oxide-semiconductor

DC Direct Current

DRC Design Rule Check

DRIE Deep Reactive Ion Etcher

DUT Device Under Test

EBL Electron-beam Lithography

EDFA Erbium Doped Fiber Amplifier

EMI Electromagnetic Interference

ER Extinction Ratio

ESA Electrical Spectrum Analyzer

FDM Fused Deposition Modeling

FDTD Finite-difference Time-domain

FSR Free Spectral Range

FWHM Full-width At Half Maximum

GPIB General Purpose Interface Bus

HF Hydrofluoric Acid

MEMS Micro-electro-mechanical Systems

MPW Multi-project Wafer

MWP Microwave Photonics

MZ Mach-Zehnder

NA Numerical Aperture

OBFN Optical Beamforming Network

ORR Optical Ring Resonator

PCB Printed Circuit Board

PIC Photonic Integrated Circuit

PL Photolithography

PLA Polylactic Acid

PVD Plasma Vapor Deposition

Q factor Quality Factor

RF Radio Frequency

RIE Reactive Ion Etcher

SFDR Spurious-free Dynamic Range

SLA Stereolithography

SMF Single Mode Fiber

SNR Signal-to-noise Ratio

SOI Silicon-on-insulator

TE Transverse Electric

TEC Thermo-electric Cooler

TIR Total-internal-reflection

TM Transverse Magnetic

UV Ultraviolet

VNA Vector Network Analyzer

WDM Wavelength Division Multiplexing

Declaration of Authorship

I, Dylan E. Genuth-Okon, declare that this thesis titled, "Design and Implementation of Processes and Components for Optical Beam Forming Networks" and the work presented in it are my own. I confirm that:

The modelling, simulation, and analysis of experimental data, as well as figures, tables and this thesis were performed primarily by myself. Some of the data acquisition and design was performed by others.

- In Chapter 4, a chapter written for this thesis: I simulated and gathered data described in the chapter. The ring modulator design was an example of the SiEPIC library. Ranjan Das and Xin Xin helped with data acquisition.

- In Chapter 5, a chapter written for this thesis: I designed systems and gathered data described in the chapter. Yu Jiang made some 3D models. Ranjan Das and Yu Jiang helped with data acquisition.

Chapter 1

Introduction

1.1 Optical Telecommunications

Telecommunications (telecom) aims for information to be transferred in as short amount of time as possible. Information through telecom can be transmitted via many avenues, nowadays leveraging electrical signals, radio signals, and optical signals. All these different avenues have their respective advantages, but optical signals have surpassed all others for high-bandwidth telecom purposes for a few reasons: (a) Optical signals can move at the speed of light in the medium it is travelling in, meaning almost instantaneous information transfer, and millisecond latency across the globe; (b) Optical signals can be transmitted in an affordable long-distance medium, and guided to its desired destination easily and securely; (c) Optical signals can be modulated at very high speeds, and a wide variety of wavelengths can be used for multiplexing, extending total bandwidth; (d) The devices used for transmitting, producing, detecting and processing optical signals can be made at low-cost, while being highly integrated and compact.

Recently, glass optical fiber manufacturing has become refined enough to permit extremely low-loss transmission through many kilometers, paving the way to transcontinental intercommunication via marine cabling. This opened the gates to using optical fibers and light, for telecommunication not only locally, but internationally [1]. The first transatlantic fiber optic cable was laid in 1988, between North America and Europe, and was able to carry 280 Mbit/s of data [2]. Now, fiber optic speeds have hit highs at 46Tbit/s [3] in research settings, and achieved 150Mbit/s bandwidths average per client worldwide [4].

To achieve higher capacity, one can transmit multiple channels through a singular fiber, where each channel can be associated with a distinct wavelength. For communications purposes, one can multiplex (or join multiple signals through a medium) the channels before transmission, and they can be de-multiplexed when received. The act of multiplexing using wavelengths is called wavelength division multiplexing (WDM). A popular WDM approach is Dense-WDM (DWDM), in which one obtains more than 40 channels instead of the limited 8 channels of Coarse-WDM (CWDM). The common wavelength range for DWDM is the "conventional" C-band, traditionally between 1530 nm to 1565 nm. This wavelength range coincides with the erbium doped fiber amplifier (EDFA) range [5], a popular choice as an optical amplifier. Different modulation formats exist that can often squeeze higher datarates out of the WDM bands, which are ultimately limited in the number of wavelengths that can be carried.

1.2 Integrated Optics

The miniaturization of the transistor using complementary metal-oxide-semiconductor (CMOS) processing over the last six decades led to an exponential increase in the number of transistors in an integrated circuit. A general trend in the increase of transistor count is displayed in Figure 1.1, which demonstrates an approximate doubling every two years. The increase in transistor count and therefore density has also led to proportional computational power increase, and reduction in cost per transistor.

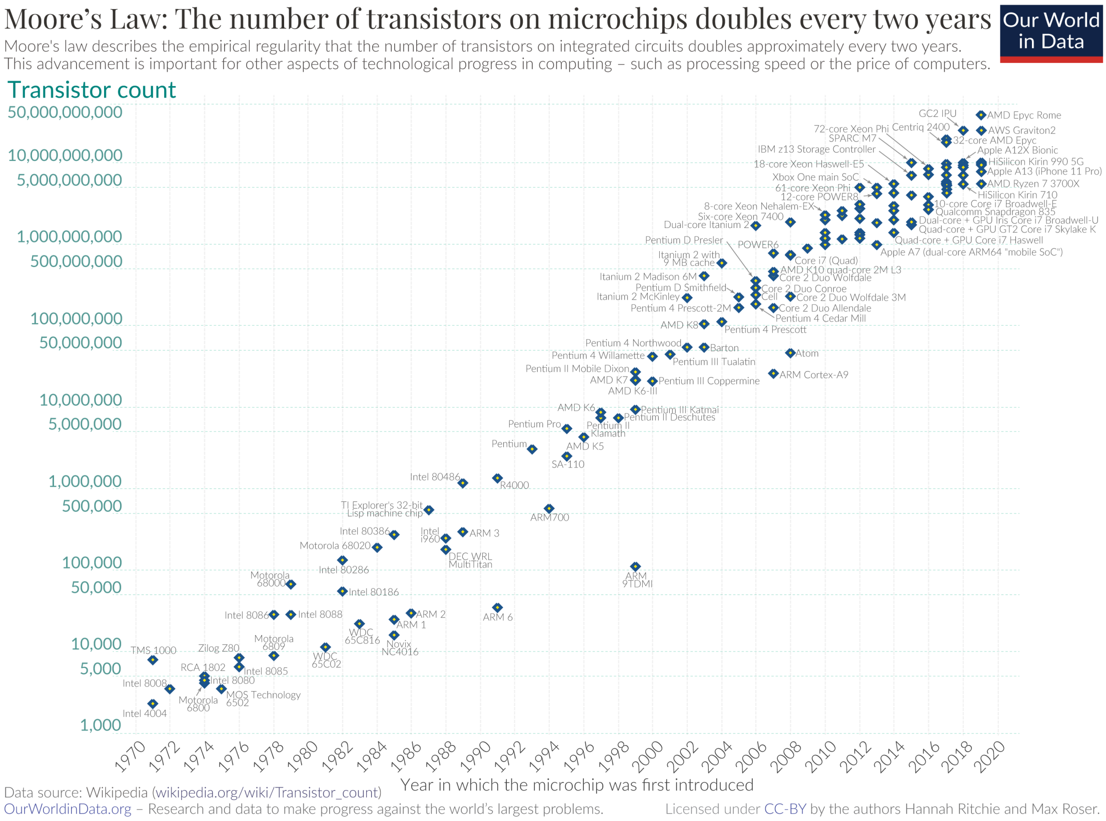

Figure 1.1: Moore's law demonstrating exponential densification in transistor count in central processing [6]. Reproduced under Creative Commons license.

The miniaturization of components has inevitably led to integration. Integration of various components is essential to reduce the footprint of devices. The reduction of device footprint is fueled by cost reductions, power efficiency, and faster speed requirements. Integrated optics refers to manipulating light within a single device, meaning, all or most components that are involved in the creation, processing, and detection of light are within one system. Systems that utilize integrated optics are often called a photonic integrated circuit (PIC).

The most popular materials for PIC manufacture are silicon or silicon-on-insulator (SOI), indium phosphide, and silicon nitride. Other materials such as lithium niobate ($LiNbO_3$) are also being pursued (lithium niobate has been popular specifically because of its strong Pockels electro-optic effect for modulation [7]) but are not as prevalent due to integration and manufacturing issues.

Of specific interest in this work is SOI which is completely CMOS compatible, is very well understood, and works well for most requirements except light emission. The best qualities of indium phosphide are its direct bandgap, and high electron mobility, which allows for fast detection, modulation, and integration of lasers in the platform [8]. Advantages of silicon nitride include its low propagation loss, somewhat good CMOS compatibility, and ability to work with high-power light [9]. Further properties of these material platforms can be seen in Figure 1.2.

	Silicon-on-insulator	**Silicon nitride**	**Indium phosphide**
Refractive index	3.5	2.1	3.1
Waveguide refractive index contrast (%)	>100	>25	10
Bending radius (μm)	5-100	50-150	100
Loss (dB cm^{-1})	0.1-3	0.01-0.2	1.5-3
Nonlinear index (m^2 W^{-1})	4.5×10^{-18}	2.6×10^{-19}	1.5×10^{-17}
Two-photon absorption (cm GW^{-1})	0.25	Negligible	60
Modulator technology (maximum speed)	Free-carrier plasma dispersion (30 GHz)	With graphene (30 GHz) With PZT (33 GHz)	QCSE-EAM (55 GHz)
Detector	Ge (50 GHz)	N/A	40 GHz
Laser output power	N/A	N/A	>20 mW
Fibre-to-chip coupling loss (dB)	2	0.5	3
CMOS compatibility	Excellent	Good	N/A
Optical amplification	N/A	N/A	>20 dB

EAM, electro-absorption modulator; PZT, lead zirconate titanate; QCSE, quantum-confined Stark effect. N/A, not applicable.

Figure 1.2: Material platforms used in microwave photonic chips with specifications [10]. Reproduced with permission from Springer Nature.

1.3 Silicon Photonics

With 5.3 billion users online in 2023 [11], well into the "Zettabyte Era", it is easy to see the need for high bandwidth communication. Low-cost and mass-scale implementation of integrated optics is paramount if industry is to keep up with demand. Silicon is the only platform in which CMOS manufacturing can be fully leveraged and allows for integration to electronic fabrication facilities. Businesses are not blind to the success and promise silicon photonics offers, with the market size expected to reach 4.6 billion USD in 2027 [12].

Silicon's largest advantage is economic. Because of its very easy integration into CMOS fabrication, most of the existing silicon electronic manufacturing is transferable. Etching solutions exist, such as using hydrofluoric acid (HF) for selective anisotropic etching of oxide, or use of a deep reactive ion etcher (DRIE) for creating trenches, slabs and walls in silicon employing the Bosch process [13]. Oxide growth can be done via deposition or following the well-known Deal-Grove model for thermal oxidation [14]. Ion implantation is a standard in CMOS processing, and so are metal vias connecting to those implanted regions. Germanium is often used in silicon photonics as a medium of detection, which is also standard in any facility that deals with silicon-germanium in its processes. The only differences between electronic and photonic fabrication is the creation of the wafer itself. The same Czochralski process is followed for silicon wafer manufacturing, but an extra step is needed for SOI.

SOI has become standard in silicon photonics because of the ability to create a waveguide that confines light horizontally and vertically (oxide or air cladding), including the bottom of the waveguide, thanks to the buried oxide (explained in detail in Section 2.1.1). The fabrication of SOI uses a technique developed in 1997, called SmartCut [15]. The dimensions can be made of any thickness, but for silicon photonics, industry has settled on a buried oxide of 2 µm, and the silicon top layer of 220 nm.

Silicon has additional strengths beyond manufacturing. Firstly, its propagation loss is about 2.4 dB/cm [16], which in a PIC is almost negligible (except for some specific applications such as true time delay). Silicon also has two means for modulation of the refractive index, one being the somewhat slow but highly efficient thermo-optic effect, and another being the faster but somewhat lossy plasma dispersion effect [17]. These allow for modulation and tuning of various photonic components. Silicon is a very weak absorber of light at 1550 nm, making it a good waveguide material, but not ideal for detection. Implanting impurities into the silicon [18] to create deep traps allows for the silicon to absorb into the 2-micron regime [19]. Alternatively, germanium, can be epitaxially grown on silicon, to detect wavelengths up to 1850 nm [8]. The only large drawback of silicon is its inefficiency as a light emitter, a process which is near impossible due to silicon's indirect band-gap. An external laser must be thus coupled into the silicon PIC to achieve a photonic system.

1.4 Photonic Packaging

A standalone PIC cannot relay any useful information without connection to the outside world. Optical and electrical interconnections should be created to interface with the PIC. Photonic packaging is the method through which the photonic chip is interfaced. Generations of packaged photonic systems and boards are envisioned in Figure 1.3, where each leads to more integration. The culmination is a packaged solution with optical connections replacing electrical ones (which reduce latency), and a small but densely packed board with integrated light emitters and multiple PICs.

Electrical connection to a photonic chip has traditionally relied on wire bonding (seen in Figure 1.4a), a technique that spans a length of wire between the silicon chip (photonic or electronic), and a circuit board, connecting to other devices. This interconnect while straightforward to implement, leads to parasitic inductance and is therefore limited in bandwidth of well under 100GHz [21]. Embedded-chip techniques (seen in Figure 1.4b) provide methods for fitting the chip within a board and connecting in a levelled top, making the length of the interconnects much shorter. This is more complex than wirebonding as special boards are needed for the specific chip to be used, but speeds and

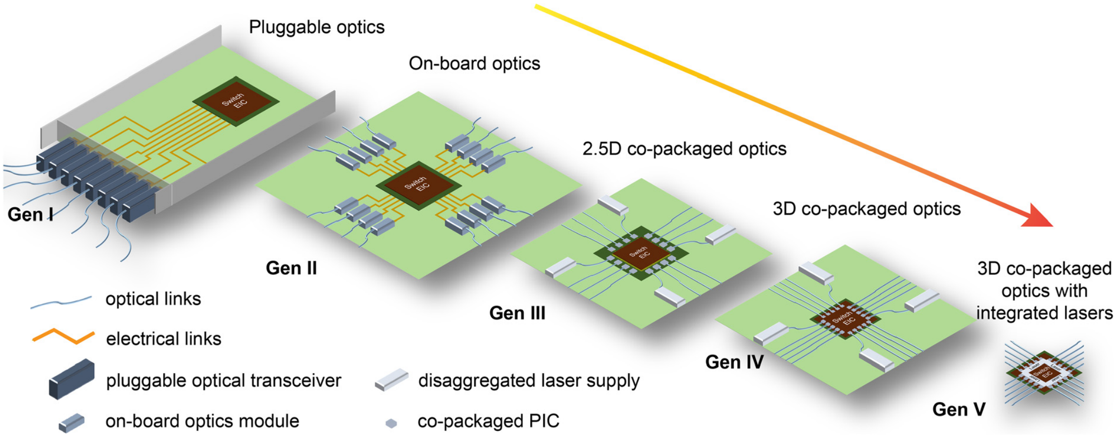

Figure 1.3: Packaging generations in order of level of integration. Reprinted from [20], with the permission of AIP Publishing.

bandwidth do increase [22]. A method that has gained a lot of traction and is considered state-of-the-art is flip-chip bonding (seen in Figure 1.4c). This method creates small spheres of metal interconnect, a chip with contact pads is flipped on these spheres, all aligned, and the whole system heated to ensure the connection. Flip-chip leads to bandwidths of over 500GHz [23], and very low signal latency as distances are short. Furthermore, this leads to the possibility of moving toward the 3-dimensional integration realm.

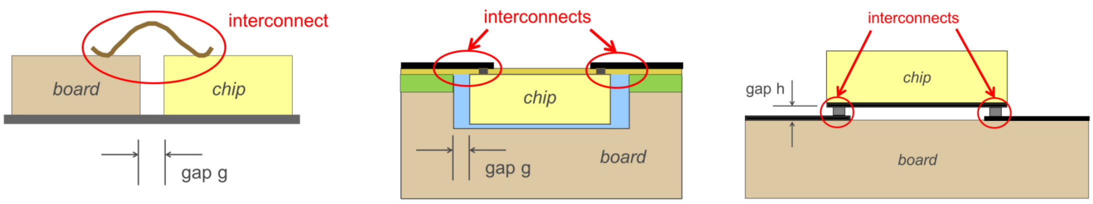

(a) Wire bonding (b) Embedded chip (c) Flip chip

Figure 1.4: Different approaches to make electrical interconnects. Reproduced from [23], under Creative Commons License.

Packaging in photonics involves not only the somewhat mastered techniques of electronic chip packaging, but it must involve optical connections as well, which is challenging. The optical connections have different requirements than those of electronic connections. In electronic packaging, merely connecting a conductive wire between the chip and a printed circuit board (PCB) is enough for direct current (DC) and even megahertz connection bandwidth. An optical connection on the other hand, must have the light pass from one medium to another (and sometimes through a third medium), as the mode expands. Simply adhering a fiber to a PIC is not possible as epoxy hardens and shifts as it cures, and misalignment by just a micrometer can lead to devastating optical loss. More information on optical coupling is given in Section 2.1.2, but specific existing approaches are provided here. Approaches sometimes include modifying the photonic chip itself, or employing special fabrication methods for creating a permanent optical coupling solution. Embedded mirrors in the chip for example can be used to couple light into a waveguide from a vertical direction [24], looking down at the chip, which allows for less precision when aligning the fiber to the waveguide. These mirrors require specialized fabrication, which only a few facilities can accommodate. Other approaches require special self-alignment structures, such as photoresist domes for fiber ferrules [25], which allow for alignment of fibers toward grating couplers. This technique removes the requirement for any fiber alignment, which is usually most tedious for grating-coupled devices. Other methods of photonic packaging include adiabatic couplers that use silicon nitride as a medium between the SOI waveguides and polymer waveguides, as developed by IBM [26]. Some of the most successful approaches include another by IBM process, where in 5 seconds, fibers can be automatically aligned onto a v-groove array within the desired chip with a 1.3dB loss [27]. All these techniques often require a specialized PIC, or specialized expensive equipment. There is no, one solution to simply couple light into a chip as of now.

1.5 3D Printing

Prototyping is extremely important in engineering and science. Every field is faced with the need to create quick and disposable parts or devices. Three-dimensional (3D) printing allows for prototyping objects in space that would otherwise be more complex or costly. The two most popular 3D printing types are lithography-style printing (which include stereolithography (SLA)) and fused deposition modeling (FDM) [28]. Lithography-style printers usually have a vat of liquid resin and polymerize the bottom layer by exposing it to ultra-violet light, and shift upward, once per layer, to create a 3D object by exposing multiple layers. SLA printers use a laser and a rotating and shifting mirror to expose a specific point on the base layer on an X-Y plane, with a resolution of the spot size of the laser. FDM printing on the other hand uses a spool of solid plastic filament, usually polylactic acid (PLA), which is fed into a hot-end and through a nozzle at about 200 °C. The nozzle deposits material, also layer-by-layer, in any position required in the X-Y Cartesian plane. Most consumer 3D-printers are FDM, and are extremely accessible at affordable prices.

In research, 3D printing has allowed for an incredible amount of possibilities. In photonic packaging, some solutions have already started to emerge. One technique allows for lensing of the light from a fiber into a chip using microspheres 3D printed onto the cross sectional interface of a waveguide, which also allows for less precision with a strong input power [29]. Another packaging approach that uses 3D printing is the creation of photonic wire bonds [30]. Much like with traditional electrical wire bonds, these connect a fiber to an exposed waveguide directly, and further allows for device integration. These techniques leverage a type of SLA 3D printing, called 2-photon stereolithograhpy [31]. This type of 3D printing has become extremely popular in fields dealing with nano and micro devices (such as in micro-electro-mechanical systems (MEMS)) as, instead of polymerizing resin layer-by-layer using one laser, one can use the two-photon absorption effect to focus intersecting laser beams onto one point. The minimum resolution is either the laser beam spot size, or the wavelength of light used (due to diffraction), whichever is larger. The problem with using two-photon stereolithography is that it requires very expensive and specialized printers.

Another interesting area of research involving 3D printing is for the electrical aspect of photonic and electronic systems alike. Radio frequency (RF) band-pass filters were created by 3D-printing base structures and then coating them with metal [32] including a ground plane [33]. RF filters, which are often of extremely high cost, are highly susceptible to noise from electromagnetic interference (EMI). EMI shields could be created with 3D printed components acting as a "Faraday Cage". The research that exists in this area, is in creating a custom filament for EMI shields, mixing PLA and electrically conducting material, and printing a cage [34], but this approach is hard to manufacture and is not accessible to most. Joining the two ideas could allow for custom EMI shields for RF electronic and photonic devices alike, as most institutions have access to a consumer 3D printer and a metal deposition system.

1.6 Microwave Photonics

Microwave photonics (MWP) is the use of high-speed RF (microwave frequencies) for modulating, processing, and detecting in a photonic platform. The advantages of processing RF signals in a PIC are many. Photonic chips and optical fibers are usually much smaller, lighter, lower-cost, lower attenuating, less prone to EMI, lower dispersion, and higher bandwidth than the equivalent electrical RF counterparts [35].

MWP PICs work by modulating an input light (laser) source (either modulating the laser itself to create pulses, or modulating an external continuous-wave laser source) at RF speeds. In silicon MWP chips, the optical source is a discrete off-chip component. The modulation is ideally done on-chip, as this leverages the benefits of integration.

The most popular and effective on-chip modulators in PICs are Mach-Zehnder (MZ) interferometers, because of their modulation speeds and linearity [36]. However, ring modulators are of interest due to their small footprint and reduced power requirements [37].

The RF signal is up-converted as a modulated optical signal. The optical signal is then processed using a myriad of possibilities, depending on the application. To down-convert back to the electrical RF domain, after processing, and maybe after transmitting the signal through a long stretch of optical fiber, a photodetector can be utilized. The most common photodetector in silicon PICs is a germanium p-i-n detector, which is capable of high speeds, high responsivity, and has a small footprint [38]. It was mentioned in Section 1.3 that silicon can be implanted to create deep traps and enable it to detect, forsaking germanium in the silicon photonic platform fabrication entirely, and further lowering costs [18].

A PIC is able to process RF signals, such as serving as an RF filter, analog-to-digital converter, and arbitrary waveform generator [35]. An interesting use of MWP is that of an Application Specific PIC [39], which can act as a field-programmable gate array (FPGA), but in the the photonic realm, using many MZ interferometers processing the RF signal as needed [40]. Another very useful MWP application is optical beamforming, which is able to create a phased-array on a PIC for ease of wireless communication [41].

1.7 Optical Beamforming Networks

The purpose of an optical beamforming network (OBFN) is to create phase delays at different antennas which are arranged in a manner so that the radial or spherical waves emitted by such antennas, together, form a planar wave towards an intended direction. This is the basis of a phased-array, changing the angle of a signal, in a solid state device rather than physically needing to rotate any elements. The development of 5G cellular technologies in the millimeter-wave frequency realm has provoked a spike of interest in the OBFN in a PIC, as it can be lower in cost, lighter, and most importantly, more power efficient than the alternatives [42]. Another application of OBFN is for satellite communication, as PICs provide imperative advantages over electronics for space, such as reduced size and weight, as well as being less prone to EMI [43].

An optical ring resonator (ORR) can provide enough of a delay to produce a substantial phase difference, and these are tunable using integrated heaters. A network of multiple ORRs can be arranged in OBFNs [44] to produce a phased-array at the detector output, by either adding more rings at different branches of the network, or tuning each ring by different amounts. Figure 1.5 demonstrates an OBFN using ORRs on different branches, but receiving a signal rather than emitting it.

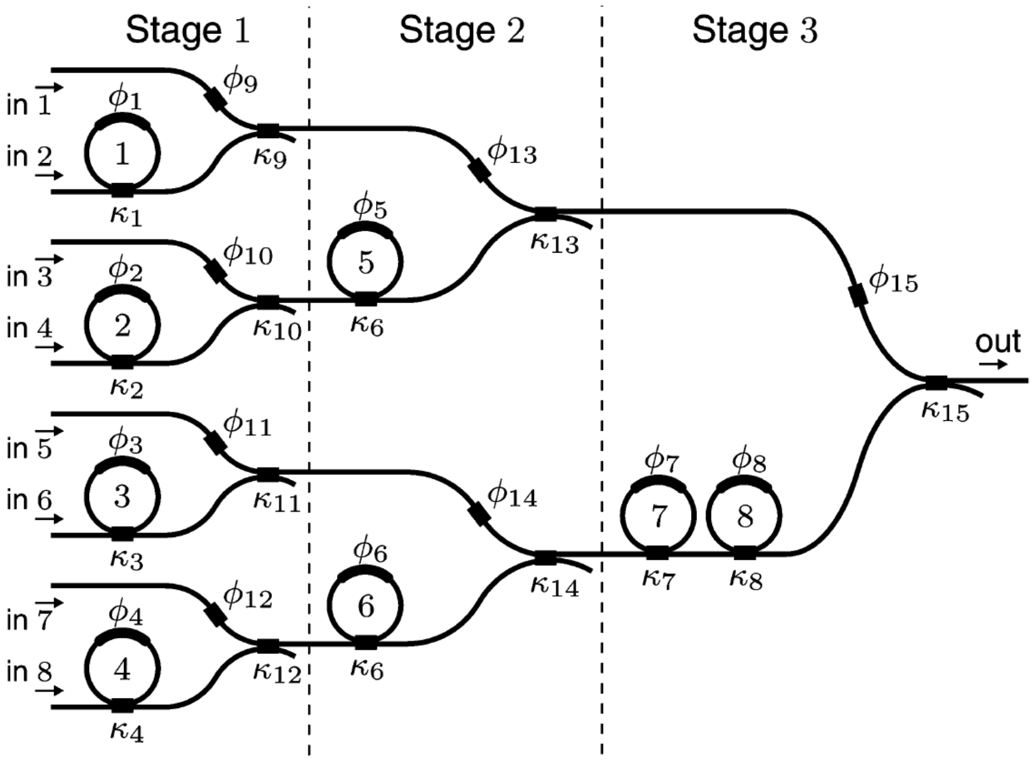

Figure 1.5: OBFN with antennas modulating a signal and joining it, with multiple rings and heaters [45]. © [2010] IEEE.

While much effort was put into understanding singular components of the OBFN, less has been done to put together a system, including all the necessary components integrated on a single PIC: the modulator, the delay ORR, and the detector. No research has been done on the use of ring modulators in such a system. This system would yield many benefits, including increased power efficiency, but also reduced chip footprint, weight, and cost. This approach does come with challenges, which will be explored further in Section 2 and Chapter 4.

1.8 Research Objectives

The work reported in this thesis had two main objectives. The first objective was to employ existing optical components to create one branch of the OBFN. The system uses ring modulators and delay ORRs. The second was to design a low-cost PIC packaging approach using highly accessible 3D printing. The approach should be capable of adding electrical integration of a PCB, and leveraged to build a low-cost EMI enclosure for such system.

Chapter 2

Theoretical Considerations

Photonic integrated circuits (PICs) require multiple components to complete their desired functions. These components can be divided into several categories, and in this thesis, they are waveguides, passive components, and active components.

2.1 The Optical Waveguide

A waveguide is a component that "guides" electromagnetic waves. The simplest waveguide is a planar waveguide as it only varies in one spatial dimension. The symmetric planar waveguide is a stack of one material sandwiched with another material on top and beneath it, seen in Figure 2.1. Light travelling in the sandwiched material is confined within the layer. The energy distribution of light is called a mode. This energy distribution can be represented by the intensity (I), which is in turn dependent on the electric field ($\mathbf{E}$) of the electromagnetic wave ($I \propto |\mathbf{E}|^2$). The electric field can be described by the wave equation [46], described by:

$$\nabla^2\mathbf{E} = \mu_m\varepsilon_m\frac{\partial^2\mathbf{E}}{\partial t^2} \tag{2.1}$$

where μ_m is the permeability of the material the wave is in (magnetic property), and ε_m is the permittivity (electric property). The mode described by Equation 2.1 is of transverse electric (TE) polarization (s-polarization), where transverse magnetic (TM) polarization (p-polarization) is the magnetic variant. This terminology states that the named transverse field only exists perpendicular to the plane of incidence when encountering a boundary. Because TE and TM modes are orthogonal, we can here (for the purposes of mathematical development) ignore one of these and focus on the other. In this thesis, the TE polarization will be that of interest.

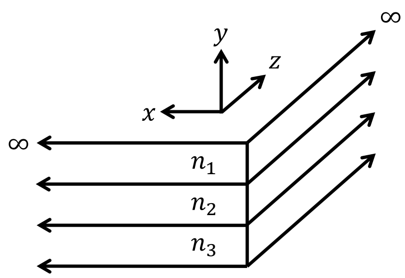

FIGURE 2.1: Planar waveguide, symmetric if n_1 and n_3 are equal.

Since in the wave equation, the constant term is equal to $1/\nu^2$, ν being the velocity, one can make a material property that defines the speed of light in the medium. This material property is the refractive index n of a material, seen in:

$$n = \frac{c}{\nu} = \frac{\sqrt{\mu_0 \varepsilon_0}}{\sqrt{\mu_m \varepsilon_m}} = \sqrt{\mu_r \varepsilon_r} \tag{2.2}$$

where c is the speed of light in a vacuum, μ_0 and ε_0 are the permeability and permittivity in a vacuum, and from that, $\mu_r = \mu_m/\mu_0$ and $\varepsilon_r = \varepsilon_m/\varepsilon_0$ are the relative permeability and permittivity of the material. A requirement for a waveguide is to support total-internal-reflection (TIR), whereby the core material is of higher refractive index than that of the surrounding cladding material, causing all light at a certain launch angle to reflect. This is expanded upon later.

If one only takes the TE mode into account, the field vector will be perpendicular to the plane of incidence. Aligning the wave so that light propagates in the z-direction, and the waveguide changes materials throughout the y-direction, then the x-axis is perpendicular to the plane of incidence, **j** and **k** vector indices in the Laplacian in Equation 2.1 can be cancelled. Furthermore, since the waveguide being dealt with is planar, the x-component of the electric field will always be uniform and non-variant. Applying the Laplacian and all the assumptions discussed, one can obtain:

$$\nabla^2 \mathbf{E} = \left(\frac{\partial^2 E_x}{\partial y^2} + \frac{\partial^2 E_x}{\partial z^2}\right)\mathbf{i} = \frac{\partial^2 E_x}{\partial y^2} + \frac{\partial^2 E_x}{\partial z^2} = \frac{1}{\nu^2}\frac{\partial^2 E_x}{\partial t^2} \tag{2.3}$$

The electric field solution can be described by:

$$E_x = E_x(y)e^{-i\beta z}e^{i\omega t} \tag{2.4}$$

written as an exponential to satisfy the differential equation. β is a propagation constant, ω is the angular frequency at which the wave sinusoidally changes in time.

Differentiating Equation 2.4 with respect to z and t, later substituting back into Equation 2.3, one obtains:

$$\frac{\partial^2 E_x}{\partial y^2} = E_x\left(\beta^2 - \frac{\omega^2}{\nu^2}\right) = E_x(\beta^2 - k^2n^2) \tag{2.5}$$

where k is the wavevector ($k = k_0$ in free space, otherwise $k = nk_0$), $k_0 = \omega/c = 2\pi/\lambda_0$, β is often known as $\beta = n_{\text{eff}}k_0$, with n_{eff} being an effective index of the several media the light propagates through (a type of weighted average of phase velocity of the mode through all media it goes through), k is related to phase ϕ via $\phi = kz \pm \omega t$.

The solution to Equation 2.5 depends on from where in space one is observing the wave function. If being looked at in the cladding (surrounding regions), it is known that the tails must go to 0, otherwise infinite energy exists. This is satisfied with an exponential decay. In the core (center) of the waveguide however, this is different. Because the wave function must be continuous in value and derivative, one must pay close attention to the interfaces of the materials, as at these boundaries the field must be equal. This means that boundary conditions can be declared at the interfaces, setting the fields and their derivatives equal to each other respectively. The solution within the core leads to a sinusoid, but there is an infinite number of allowed crests and troughs within the region, which leads to an infinite number of modes being allowed (these are different eigen-values that solve Equation 2.5). In reality, the refractive indices and dimensions of the waveguide are what determine its effectiveness, and how many modes can be "fit" (how many will not immediately attenuate) in addition to the lowest order mode. As the dimensions and refractive indices change, so do the effective indices. Each mode has a different effective index for the same waveguide.

One important aspect of optical waveguides formed in silicon (and in common with all optical waveguides) is that the mode is not fully confined within the silicon waveguide core, but rather, there is an evanescent portion of the field outside, leaking into the silicon dioxide cladding surrounding it, as seen in Figure 2.2. This evanescent field is described by the solution of Equation 2.5, where an exponential decay of the field is observed outside the boundary of the waveguide core. This evanescent field can couple into adjacent waveguides that are close enough to it, and leak the whole mode toward the other waveguide after some distance. This leaking of the waveguide into another is a form of mode coupling.

A component commonly used which exploits this principle is the directional coupler, whereby two waveguides are close enough to couple and split guided optical power. The coupling coefficient is κ:

$$\kappa^2 = P_{\text{cross}}/P_0 = \sin^2(CL) \tag{2.6}$$

a function of the coupling coefficient C (dependent on dimensions of the waveguides, materials, and distance between waveguides) and coupling length L. This function is sinusoidal, such that the field goes from one waveguide to the other, and can fully come back to the original waveguide (t being the through power coefficient, where $\kappa^2 + t^2 = 1$) given the length of coupling is sufficient. This process is in principle lossless, as the light is fully coupling into adjacent waveguides and not radiating away.

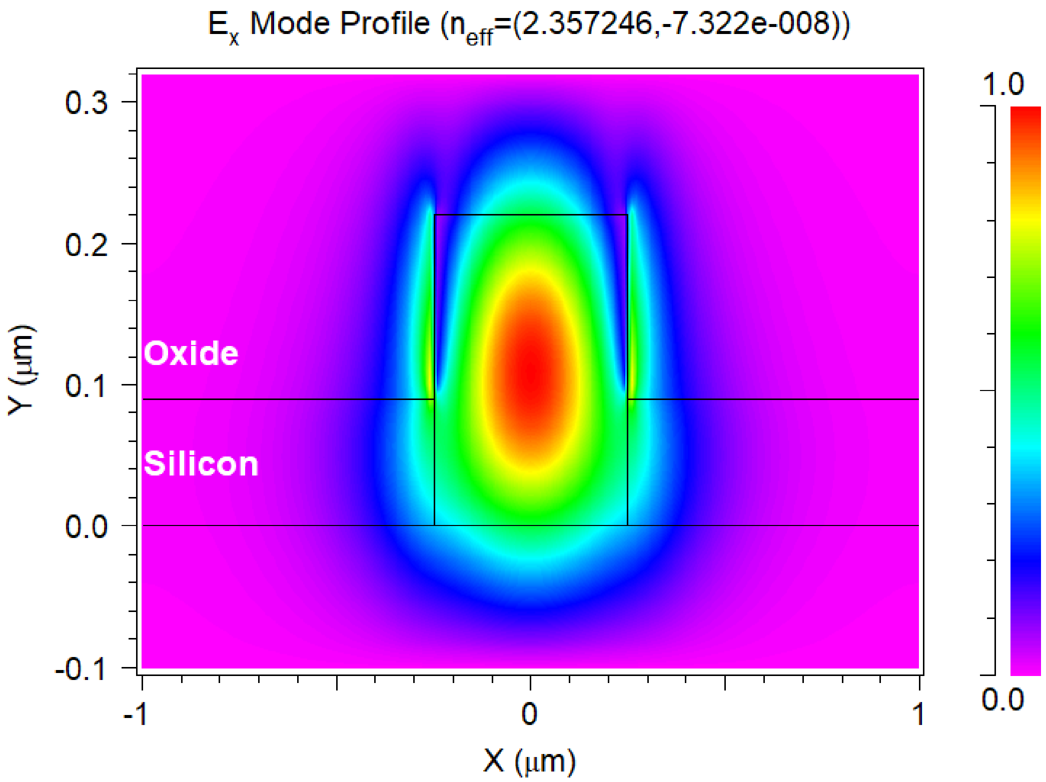

FIGURE 2.2: Mode evanescence into oxide in a rib waveguide.

Discussed above is the wave approach to optical waveguiding, which is capable of describing the modes within a waveguide. A simpler (but more macroscopic) approach is to treat the waveguide as two parallel mirrors that reflect light back and forth, causing TIR. Figure 2.3 demonstrates light reflecting within a medium. According to the Fresnel equations, one can calculate the reflected portion of a light beam when at an angle from one medium to another:

$$r_{TE} = \frac{E_r}{E} = \frac{n_1 \cos\theta_1 - n_2 \cos\theta_2}{n_1 \cos\theta_1 + n_2 \cos\theta_2} \tag{2.7a}$$

$$r_{TE} = \frac{E_r}{E} = \frac{n_1 \cos\theta_1 - \sqrt{n_2^2 - n_1^2 \sin^2\theta_1}}{n_1 \cos\theta_1 + \sqrt{n_2^2 - n_1^2 \sin^2\theta_1}} \tag{2.7b}$$

With the aid of Snell's law, $n_1 \sin\theta_1 = n_2 \sin\theta_2$, one can substitute and get 2.7b, which only depends on refractive indices and the original angle of the light beam.

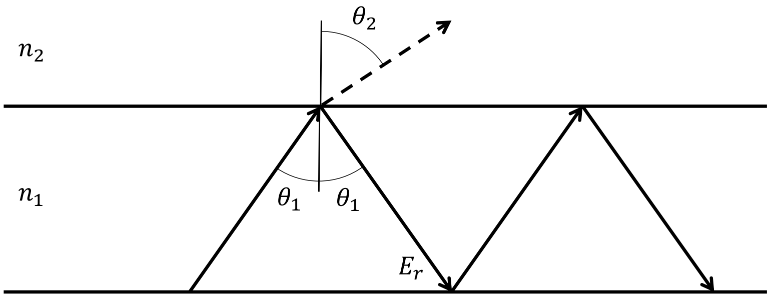

FIGURE 2.3: Reflection and TIR behaviour.

From Equation 2.7b, one can see that TIR happens when a critical angle ($\theta_c = n_2/n_1$) is met, dependent on the refractive indices of both the core and the cladding material. This is evident when viewing Figure 2.3, the angle of the dashed transmitted ray can reach a certain point in which θ_2 becomes larger than 90°, in which case TIR happens. Using the ray approach, a value known as the numerical aperture (NA) can be extracted. This value is commonly used in optical fibers, being waveguides themselves, but cylindrical in nature rather than the planar model discussed above. The NA value relies on the acceptance angle of the optical fiber ($n_a \sin\theta_a = n_1 \sin(90° - \theta_c)$, where n_a is the refractive index of the medium outside the fiber, usually air, and θ_a is the acceptance angle). The NA:

$$\mathrm{NA} = n_a \sin\theta_a = \sqrt{n_1^2 - n_2^2} \tag{2.8}$$

is important as it determines what light can and cannot couple into or out of a fiber.

Optical fibers, just like planar waveguides, can carry a limited number of modes, depending on their diameter, materials, and wavelength used. This is given by:

$$m_{\max} \approx \frac{2n_1 d \cos\theta_c}{\lambda} \tag{2.9}$$

where n_1 represents the refractive index of the core, d is the height of the waveguide. This equation yields an integer number of maximum allowed modes ($m_{\max}$+1), rounding down to the nearest integer, starting from the 0^{th} (or lowest order mode) [47]. The smaller the waveguide, the lower the effective index of the waveguide, and therefore the index mismatch between core and cladding reduces. Such a decrease in effective index leads to radiation loss as the mode is not as confined. The effective index also increases with size of a waveguide (as most of the mode is in the core and does not evanescently leak into the cladding), which is why small waveguides cannot fit more than one mode within them. This gives rise to the single mode fiber (SMF), which is designed to only carry one mode and attenuate all others along the stretch of the fiber.

2.1.1 The Silicon-On-Insulator (SOI) Waveguide

A silicon-on-insulator (SOI) wafer is ideal for silicon waveguide manufacturing. The reason for this is that it includes a buried oxide (BOX) underneath a thin silicon layer. This allows for light to be confined within the silicon ($n_{\text{Si}} \approx 3.5$) as it has a very large index mismatch to the BOX ($n_{\text{SiO}_2} \approx 1.5$) underneath and cladding (that be air or also oxide) on top ($n_{\text{air}} \approx 1$). Shown in Figure 2.4, the standard SOI wafer has a 2-micron thick BOX layer, and most photonics foundries use a 220 nm thickness for the top silicon layer [17].

Larger waveguides allow for more modes to fit within them. As seen in Equation 2.9, d can determine how many modes of a specific wavelength can fit in a waveguide of index

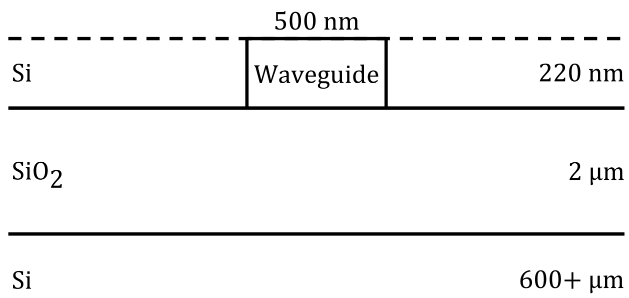

Figure 2.4: SOI cross section with fabricated strip waveguide.

n_1. This means that in the x and y directions, one can engineer a rectangular waveguide to transport as many modes as one wishes within it, by adjusting the dimensions in that axis. The 220 nm thickness is just below the single TE mode cutoff at 1550 nm wavelength [17]. If one would want the waveguide to support more modes in the y-direction, the thickness of silicon would need to be modified. The thickness of layers for non-custom multi-project wafer (MPW) runs are set by the foundry as to lower cost, upscale, and ease production.

The width of the waveguide also determines how many modes will fit within it. The waveguide width is usually not determined by the fabrication facility, but rather, the designer themselves, who can modify widths and lengths with limits. Foundry services can guarantee up to a certain resolution for each layer. For fabrication facilities, it is easier to control thicknesses (as etching and deposition tools have nanometer resolution), than widths and lengths (as masking processes in entry-level photonics fabrication usually have minimum features of over 100 nm [48] for UV photolithography, or over 40 nm [49] for electron-beam lithography). This limitation imposed on the designer is one factor that leads to waveguides having to be wider than their thickness, a usual number being 500 nm. The value of 500 nm is just above the single mode cutoff for TE polarized light at 1550 nm. The two dimensions of 220 nm and 500 nm are in the ideal range for lowest loss in waveguides while maintaining single-mode operation.

The waveguide discussed above is a strip waveguide (shown in Figure 2.5 on the right). These waveguides are simple rectangles of silicon. Rib waveguides can also be used. These waveguides have a silicon slab region (usually 90 nm in height compared to the 220 nm of the waveguide), which extends to whatever distance necessary (shown in Figure 2.5 on the left), and modifies the effective index of the mode. Compared to a strip, the rib waveguide mode elongates horizontally in the bottom slab. The slab region is usually used to make electrical connections and/or make doped regions for active devices. It must be noted that rib waveguides, because of the slab, will have a different coupling coefficient and coupling ratio than an equivalent pair of strip waveguides as the mode profile differs from that of a strip waveguide.

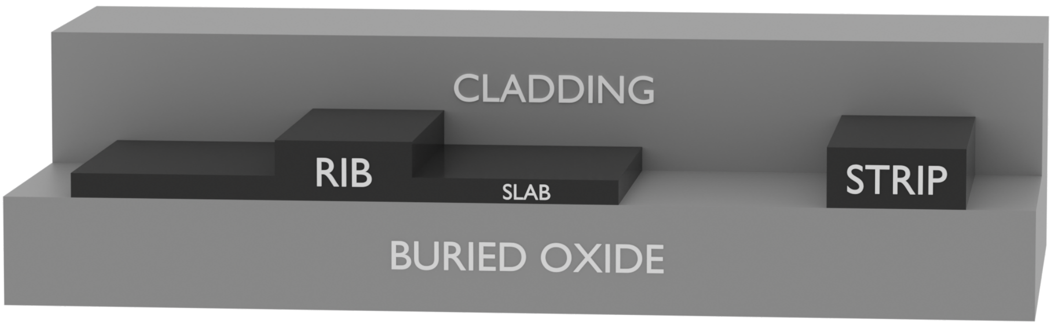

Figure 2.5: Waveguide types in an SOI PIC. A rib waveguide on the left with slab regions on either side, a strip waveguide on the right, both surrounded by cladding and buried oxide below.

2.1.2 Fiber to Chip Coupling

Coupling light into a photonic device is a challenging necessity for silicon photonics, as it requires very careful alignment from a fiber to a waveguide in the chip. There are two main types of coupling into PICs, grating and edge coupling. Grating coupling is useful as it can allow for coupling anywhere on the surface of a chip, enabling better use of chip real estate. This type of coupling though, necessitates a rather cumbersome angle for coupling (8 degrees from normal to the chip surface), and can interfere with electrical components throughout the surface, as well as leading to relatively high coupling loss. Edge coupling allows the optical fiber to be parallel to the chip surface, normal to the edge. This eases coupling (usually x and y direction need to be changed, z direction being the axis of propagation), can be packaged more conveniently, and enables electrical interfacing to metallic pads along the surface of the chip. The work described in this thesis is exclusively edge coupling based.

Coupling loss refers to the optical loss experienced from a fiber to a chip, or the other way around. It is essential to understand the NA of an optical fiber, given by Equation 2.8, in order to appreciate how coupling is so complex and sensitive to deviation. Using Equation 2.8, one can use the refractive indices of core and cladding, or the listed NA of an SMF. The specific fiber used in this example is SMF-28-J9, with an NA of 0.14 [50]. Setting n_a to ≈ 1 as the medium between fiber and chip is usually air (not always the case, index matching fluid can be used), one can find θ_a, the acceptance angle, which is a half-angle of the acceptance cone. The half-angle $\theta_a \approx 8°$, therefore an acceptance cone of 16°. This small angle may seem limited, and it is, but it is exacerbated by the fact that the waveguide one is coupling to is usually 500×220 nm in size. The usually gaussian output from the 0^{th} order mode of a laser (through an SMF to remove all other modes) will have a diameter of 2.8 µm at a 10 µm distance. The gaussian nature of the mode needs to be factored in, which peaks in the center and quickly decreases near the edges. This 2.8-micron diameter must align with the small waveguide leaving a 1.4 µm radius. But the 1.4-micron tolerance can cause a large loss if shifted by just a micron, as it follows the gaussian profile of the mode. This is why coupling is complex to do in practice, as positioning in the x, y and z directions needs to be very precise, and any angles between the normal of the fiber tip and the waveguide facet must be eradicated.

For ease of coupling as well as for minimizing coupling loss, many labs use tapered or lensed fibers, which are able to focus light from and to the fiber, maximizing its

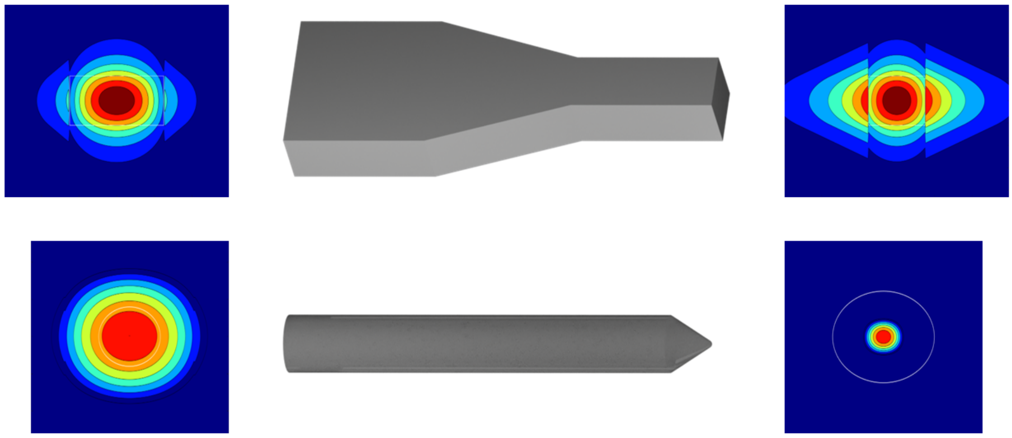

FIGURE 2.6: Tapered waveguide and fiber, with input and output modes.

focusing to a specific focal point, which is ideally aligned to the waveguide in question. Another possibility is to enlarge the mode that enters or exists the waveguide. Because the waveguide mode is so constricted and small in cross-section (it is ideal for it to be this way inside a device as it minimizes attenuation and cross-talk) in its standard definition of 500×220 nm, tapered waveguides also exist to increase this mode size. The mode size can be enlarged by simply making the waveguide smaller. Modes resized by tapered waveguides and fibers can be seen in Figure 2.6. By making the silicon core smaller, the effective index becomes smaller as well, forcing the mode out into the cladding. The waveguide tapering can be done near the edge of PICs, easing the transition between waveguide and fiber, enlarging the mode to match the mode field diameter of the SMF itself [50]. Other options exist whereby a polymer waveguide is placed around a tapered silicon waveguide, and it essentially absorbs the mode and expands it [51]. The polymer can be deposited and fabricated on an existing SOI PIC, but alignment of the mask must be performed, and the process is not complementary metal-oxide-semiconductor (CMOS) compatible, must be done as a post-processing step [52], but does ease optical packaging, especially when co-packaging using flip-chip integration.

2.2 Passive Optical Components

PICs do not only transport light from one point to another, as this is what a simple optical fiber could achieve. Photonic chips process light in many ways, and there is a multitude of components that serve several different functions. Passive components are components that do not require power for achieving their purpose, they work by simply existing. There is a very large variety of passive components (including waveguides), but only the components relevant to this thesis will be outlined in this section.

2.2.1 Micro-Optical Ring Resonator

An optical ring resonator (ORR) is a very useful device in the arsenal of a photonic chip designer. The basic ring resonator consists of two half-loops of waveguide connected to create a circular ring, or race-track ring (where for the race-track straight lengths exist to connect the half-loops) as seen in Figure 2.7. More complex structures exist in order to change certain parameters, and be able to couple light in and out, such as an add-drop versus all-pass ORR, where the former places an extra waveguide on the other side it is coupled into to drop part of the signal. The ORR is essentially a resonant cavity that can store energy by maintaining light within it. The resonant cavity lets the ORR perform as a spectral filter, being able to resonate with some wavelengths and destructively interfere with their transmission. The resonance condition is determined by the round-trip optical path length, a function of the waveguide index and physical path length (L_{rt}) of the stretch of waveguide in the loop. The round-trip length is given by $L_{rt} = 2\pi r + 2L_c$, where r is the radius of the loops, and L_c is the race-track coupler length, which is 0 when the ring does not have a race-track structure. The transmission spectrum of a ring resonator is given by:

$$\frac{E_{\text{thru}}}{E_{\text{in}}} = \frac{te^{-i\phi_{rt}} - \sqrt{A}}{e^{-i\phi_{rt}} - \bar{t}\sqrt{A}} \tag{2.10a}$$

$$\phi_{rt} = \beta L_{rt} \tag{2.10b}$$

$$A = e^{-\alpha L_{rt}} \tag{2.10c}$$

where ϕ_{rt} is the round-trip phase and A is the power attenuation the light experiences, given in Equation 2.10b and Equation 2.10c ($t = \sqrt{1-\kappa^2}$ is the through power coefficient, $\bar{t}$ is its complex conjugate, α the absorption coefficient, and β the propagation constant of the mode) [17].

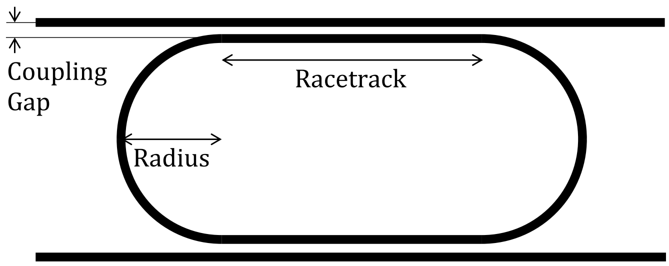

FIGURE 2.7: Racetrack add-drop ORR.

A naturally occurring phenomenon with resonant cavities, as an integer multiple resonances exist, is a frequency comb. In optics, the free spectral range (FSR) describes the frequency or wavelength gap between each successive resonance. The FSR is:

$$\text{FSR} = \frac{\lambda^2}{n_g \Delta L} \tag{2.11}$$

where ΔL is the path length difference or L_{rt} in a ring resonator, n_g is the group index of the light through the waveguide. n_g depends on various factors, like effective index, but at 1550 nm, a strip waveguide has an $n_g \approx 4.2$ and a rib waveguide has an $n_g \approx 3.9$ (using standard waveguide dimensions discussed in Section 2.1.1).

The quality of the resonance is of utmost importance when it comes to resonant cavities, as it denotes how good of a filter the ORR is at that specific wavelength. Some figures of merit of a ring resonator transmission spectrum are shown in Figure 2.8. One important term is the extinction ratio (ER), this is the notch depth in transmission power at the resonance relative to the power off-resonance. Extinction ratio is often denoted in decibels (dB), a relative logarithmic measure. The ER is not the only metric that is used to describe a resonance as it misses many important features. The quality factor (Q factor) is a metric that takes care of this deficiency, a value that represents how selective a transfer function is, is given by $Q = \omega_0/\Delta\omega$, where $\Delta\omega$ is the full-width at half maximum (FWHM) of the resonance. This metric clearly paints a good picture at how narrow a transfer function is at any given frequency. What this means physically is how much energy is stored versus how much is lost in the cavity. The quality factor is dependent on the internal quality factor (Q_i) and external/coupling quality factor (Q_c), one being the propagation loss within the ring (from surface roughness, bend radius, defects, and more), and the other being related to coupling to the ring from the waveguide bus, respectively. Q_i and Q_c are given by:

$$Q_i = \frac{2\pi n_g}{\lambda \alpha_{\text{avg}}} \tag{2.12a}$$

$$Q_c = \frac{2\pi c}{\lambda \kappa} \tag{2.12b}$$

where $\alpha_{\text{avg}} = -\log(\alpha)/L_{rt}$ is the average loss per distance. The total Q is dependent on both ($1/Q = 1/Q_i + 1/Q_c$) [53]. Because part of the Q factor is dependent on gain (coupled light) and loss (attenuation), and since it is a measure of energy stored, then one can say that the highest Q has the perfect ratio of light gain and loss. The highest Q happens at critical coupling, if a ring is over or under coupled however, the Q factor decreases.

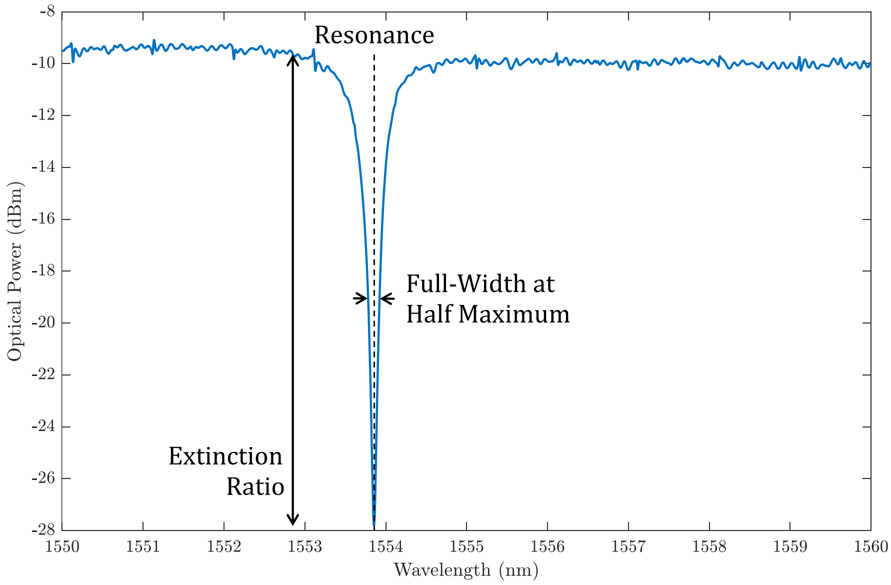

FIGURE 2.8: Transmission spectrum of an ORR.

The resonance of an ORR can be tuned by using the thermo-optic effect, exploiting silicon's relatively large thermo-optic coefficient. With this, one can obtain [17]:

$$\frac{\mathrm{d}\lambda}{\mathrm{d}T} = \frac{\lambda}{n_g}\frac{\mathrm{d}n_{\mathrm{eff}}}{\mathrm{d}T} = \frac{\lambda}{n_g}\frac{\mathrm{d}n_{\mathrm{eff}}}{\mathrm{d}n}\frac{\mathrm{d}n}{\mathrm{d}T} \tag{2.13}$$

The change in wavelength versus change in temperature $\mathrm{d}\lambda/\mathrm{d}T$ is the change in index of the silicon as a function of temperature $\mathrm{d}n/\mathrm{d}T$. This is because the change in silicon's refractive index changes the effective index of the medium. This leads L_{rt} to effectively change as temperature increases (increase as temperature increases), which changes the resonant wavelength, tuning the ring transmission spectrum. This effect is commonly used to tune ORRs with heaters, a resistive element (usually TiN or TiW) patterned and deposited a few microns above the silicon layer (with oxide cladding in-between). The heating is simply created by running a current through the resistor where power is converted to heat energy, and dissipates in the PIC. A certain power threshold can yield a π-phase shift in the wavelength transmission spectrum. The thermo-optic effect is efficient, but its implementation with integrated heaters has three large drawbacks: 1. the heat energy is not easily contained and thermal cross-talk between elements can exist, 2. the thermal switching is a slow process, limiting the speeds to the megahertz range, and 3. the transmission spectrum and resonances can only be red-shifted, and not blue-shifted, as the heating elements cannot be used for cooling.

2.2.2 Optical Delay Elements

Modulation of ORRs results not only in magnitude modulation of their transfer function, but the phase modulation as well. Phase modulation leads directly to a group delay (i.e. a delay in information transfer). A formulation to describe the group delay time τ_g is found:

$$\tau_g(f) = \frac{\kappa \tau_r}{2 - \kappa - 2\sqrt{1-\kappa}\cos(2\pi f \tau_r + \phi)} \tag{2.14}$$

where all variables have been previously defined. Here, the power coupling coefficient κ and the phase shift ϕ can be easily tuned with integrated heaters [54]. Equation 2.14 is a derivative of the phase response versus frequency. With this equation, one finds that the group delay can be modified with a change in coupling coefficient. One can therefore design ORRs to add delay (up to a point), and continuously tune it at will. This opens the door to optical beamforming network (OBFN), to delay different parts of a network and create a phased-array.

2.3 Active Components

Passive components, while useful for many applications, do not leverage the electronic nature of PICs, that be III-V materials or silicon. This is why, to really move forward the field of photonics and create useful devices, some components must exist to serve purposes required for applications such as modulation, detection, and more. An active component is a device that consumes power to modify a transfer function and therefore produce an output. This allows for much more customization and use than with a passive component. The more active components can be put on a PIC, the less external devices or instrumentation is needed, further integrating and miniaturizing photonics. Again, there are many active components that exist in PICs, but only the ones relevant to this thesis will be discussed.

2.3.1 Optical Ring Modulator

The optical ring modulator is a ring resonator with a pn-junction integrated. As discussed above, the thermo-optic effect in silicon, while efficient, has a low-speed limit when it comes to modulation, due to the relatively slow dissipation of heat. Another option for modulation in silicon is the plasma dispersion effect. Plasma dispersion modifies the refractive index of light in silicon, dependent on the concentration of charge carriers (that be n-type or p-type). The change in the real part of refractive index Δn and change in the imaginary part (absorption) $\Delta\alpha$ (given in cm^{-1}) are given by:

$$\Delta n(\lambda) = -3.64 \times 10^{-10}\lambda^2\Delta N - 3.51 \times 10^{-6}\lambda^2\Delta P^{0.8} \tag{2.15a}$$

$$\Delta\alpha(\lambda) = 3.52 \times 10^{-6}\lambda^2\Delta N + 2.4 \times 10^{-6}\lambda^2\Delta P \tag{2.15b}$$

These equations are dependent on both wavelength and carrier concentration [17]. This means that refractive index can be modified by changing the potential at the junction, as charge carriers are dependent on the electric field one applies. This can lead to high speed modulation. Changes in loss lead to a change in extinction ratio and Q factor, Q_i specifically, as the loss within the ring is modulated as well as the real component of the refractive index.

The rib waveguide (Figure 2.5) can support a pn-junction, usually laterally. Often, the pn-junction is located in the center of the waveguide, creating a depletion region, which can be thought of as void of free carriers. The depletion region width when a bias is applied W_{bias} is given by [8]:

$$W_{\text{bias}} = \sqrt{\frac{2\varepsilon_0\varepsilon_r(V_0 - V)}{q}\left(\frac{1}{N_a} + \frac{1}{N_d}\right)} \tag{2.16}$$

In Equation 2.16, V_0 is the built in contact or diffusion potential of the diode given by:

$$V_0 = \frac{kT}{q}\ln\left(\frac{N_aN_d}{n_i^2}\right) \tag{2.17}$$

where V is the applied voltage, q is the elementary charge (charge of an electron in coulombs), N_a and N_d are the acceptor and donor impurity densities respectively, and n_i in Equation 2.17 is the carrier concentration of intrinsic silicon in thermal equilibrium.

A typical representation of silicon waveguide doping is seen in Figure 2.9. The high doping connected to the metal contacts is used for an ohmic response (ohmic contact) at the silicon-metal junction.

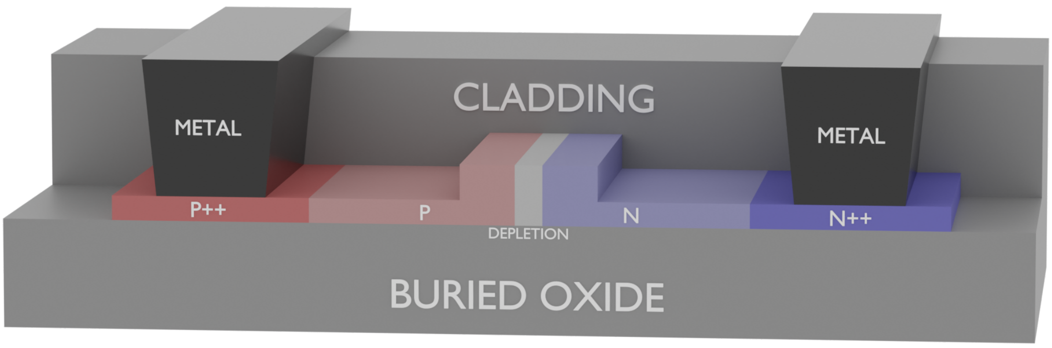

FIGURE 2.9: A pn-junction through a rib waveguide, with metal contacts on either side. A depletion region forms in between p and n regions.

The change in refractive index in the silicon waveguide yields a change in effective index for the mode, and therefore yields a phase shift with respect to an unbiased structure. This phase shift is responsible for a shift in resonance with respect to the original transmission spectrum of the ring resonator.

An aspect of significance for modulators is speed. With the help of plasma dispersion, one can modulate much quicker than with the thermo-optic effect. The modulation is done by selecting a wavelength, tuning the ring modulator to resonate at or near that wavelength (most times the wavelength used for modulation is the spot in the spectrum with highest slope for linearity purposes), and then modulating using a small signal (a slight ΔV). The 3 dB cut-off frequency f_c is given by the RC time constant of the circuit, where $f_c = 1/2\pi RC$. Here, R is the resistance of the diode dependent on the sheet resistances of the n and p doped regions (including slab regions), and C is the capacitance at the depletion region using the thickness of the rib of the waveguide (220 nm). Longer diodes induce larger capacitance, and therefore lower frequency.

Ring modulators are special cases in modulators, as f_c depends not only on the RC time, but also the photon lifetime τ_p ($1/f_c^2 = 1/f_{\tau_p}^2 + 1/f_{RC}^2$). It is important to know how long a photon exists in the ring cavity (i.e., how long the cavity stores energy), where $f_{\tau_p} = 1/2\pi\tau_p$. The Q factor is dependent on how much energy is trapped in the cavity, in the ring resonator, and therefore, one can say that $\tau_p = Q/\omega_0$, where ω_0 is the optical frequency. This leads to an interesting design choice between Q factor and modulation speed. One cannot have a very good extinction ratio at a very high speed, as Q increases, f_c decreases.

Forward bias generally yields a better modulation depth due to larger resonance shift, and with that, a reduction in small-signal voltage, or a much larger difference in signal power at the same small-signal voltage compared to reverse bias [55]. This can drastically improve signal-to-noise ratio (SNR), a very important figure for many applications, including OBFN. There are however drawbacks to forward bias operation in ring modulators. Firstly, the modulator must be designed with forward bias in mind, which limits its use in reverse bias operation. Secondly, forward bias induces significant current through the pn-junction diode, given in the Shockley diode equation:

$$I = I_s \left(e^{V/nV_T} - 1\right) \tag{2.18}$$

where I is the current through the diode, V is the voltage applied, $V_T = kT/q$ is the thermal voltage, I_s is the saturation current and n is the ideality factor, both of which are diode-specific and are usually fitted. The current in forward bias being larger, leads to higher power dissipation. Finally, the main issue with forward biased modulators is the limit in bandwidth. As discussed before, τ_p and τ_{RC} were limiting factors for ring modulators, but a much larger value of τ_n (non-radiative recombination time constant) exists in forward bias, which was negligible in reverse bias. The recombination time (or carrier lifetime) in silicon depends on doping, but usually lay between the millisecond and nanosecond range, leaving the possible 3 dB switching frequency to be below 1 GHz. There are several applications that prefer the improved SNR over bandwidth, such as satellite communication.

Ring modulators are non-linear in nature. If one were to modulate a sinusoid in a ring modulator, the modulated signal would not be a perfect tone. To reduce non-linearity, the modulation (small signal input) is applied at the point of highest slope of the transmission spectrum (transfer function) of the ring modulator. This usually ensures the most linear transmission as the slope is approximately constant, any curvature in the response would add distortion to the output. A higher Q factor generally yields better linearity, and as mentioned previously, better extinction ratio, but also worse bandwidth (in reverse bias). Furthermore, in reverse bias, the capacitance of the pn-junction can induce a non-linear effect, which is not present in forward bias [56]. A measure of the non-linearity distortion is the spurious-free dynamic range (SFDR), which compares the distortion to the noise floor of the signal.

2.3.2 Photodetector

A photodetector is crucial for a PIC. Although external photodetectors exist, an internal photodetector makes the whole package much smaller and integrated, with minimal loss induced. The photodetector detects an optical signal and converts it to an electrical signal.

Most photodetectors are diodes, pn-junctions, which create an electron-hole pair for collection (charge separation). Photodetectors can be designed in multiple ways, so understanding and measuring their performance is key to figuring out which is best. Responsivity R is one of these metrics, $R = I/P$, where I is the current generated by the detector, and P is the optical power input. The responsivity is therefore how many amps of current one obtains from a particular watt of incident optical power, a measure of efficiency. Quantum efficiency η is also proportional to R, where $R = \eta q\lambda/hc$, h is Planck's constant. A perfect efficiency for a traditional photodetector would yield 1.25 A/W, at a wavelength of 1550 nm, but this is not necessarily a limit, as discussed later.

Another metric of performance is bandwidth. As with modulators, the RC time may act as a bandwidth limit, as the pn-junction forms a capacitor. Carrier extraction/transit time is also important for bandwidth, the electron and hole mobility determine how quickly information gets from the detected light at the waveguide, to the metal contact and up the electrical instrumentation connected. Mobility (μ_e and μ_h for electrons and holes respectively) determines charge velocity, along with electric field applied, up to a point, at which the velocity is saturated. The saturated velocity of the carriers, along with the distance they have to travel determine the maximum transit time, and therefore, transit frequency.

An important performance parameter is dark current, a measure of current when there is no photocurrent produced. Dark current contributes noise, and thus the lower, the better. There are two sources of dark current. One is bulk generation, which comes from defects within the detector volume and only increases with applied field (applied voltage). A way to mitigate this is by growing higher quality layers of material for detection. The second source is surface generation, which is in-part due to dangling bonds at the surface of the device. The surface defects can be reduced with the help of surface passivation, for example, growing or depositing an oxide layer to stop surface recombination. Normally, bulk generation is much larger than surface generation due to it having an extra dimension's worth of defects to work with.

The most common type of detector is a p-i-n detector as seen in Figure 2.10, a pn-junction with an intrinsic (undoped) region in the center. The intrinsic region increases the responsivity as light produces electron-hole pairs in it rather than be absorbed by the doped p and n regions. These e-h pairs are drifted away by the electric field and sent to their respective p and n doped material, to the electrodes. These types of detectors can be vertical in p-i-n structure instead of horizontal, depicted in Figure 2.10, and can include germanium.

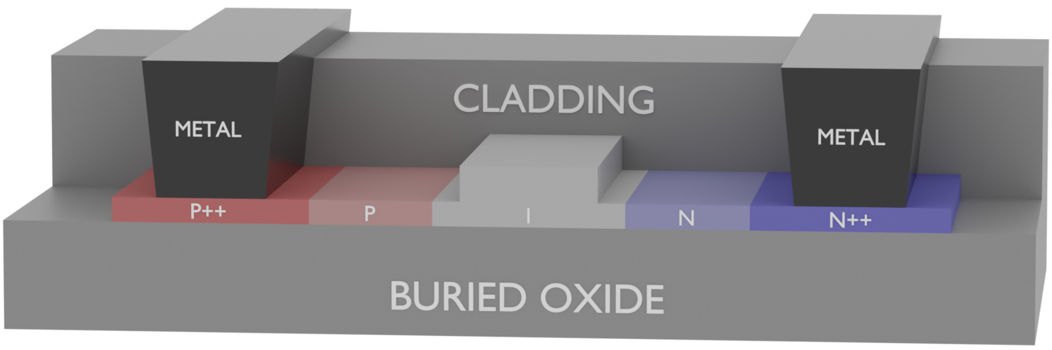

Figure 2.10: A p-i-n detector, with an intrinsic region spanning the waveguide.

Avalanche photodetectors (APDs) can obtain higher responsivities (even higher efficiency than $\eta = 1$) by employing carrier avalanching. APDs get their name from avalanche breakdown, where in high reverse bias, impact ionization occurs due to the strength of the field. This induces a chain reaction, where one carrier will create more electron-hole (e-h) pairs, not only photons. This allows for the signal created by one photon to have gain, a multiplication factor M, which serves as an internal amplifier, and therefore obtains much higher responsivity than traditional photodetectors. M goes to infinity when the diode reaches its breakdown voltage. The avalanching process creates its own noise, and transit time. The APD transit time not only depends on one e-h pair created by a photon to reach the electrodes, but in avalanche mode, e-h pairs creation is continuous. An effective carrier transit time τ_{eff} can be found, $\tau_{\text{eff}} = N\tau(\alpha_p/\alpha_n)$, where τ is the original e-h carrier transit time, N is a value dependent on the ionization coefficient ratio, and α_n and α_p are impact ionization coefficients for electrons and holes respectively [57]. With the effective carrier transit time, a new bandwidth can be calculated, found that it is smaller than in non-avalanche operation.

In regards to materials, PIC photodetectors are usually silicon, germanium, or III-V materials. III-V semiconductors are not compatible with silicon or the CMOS platform, and will therefore be ignored here. Germanium photodetectors are the most common in silicon photonics as they can be made very small due to their high responsivity in the desired wavelength of 1550 nm (germanium bandgap absorbs this), and can obtain high bandwidths of many 10's of GHz. The lattice mismatch between silicon and germanium does cause lattice defects in this material system, adding to unwanted noise. An alternative material system is defect mediated silicon, in which deliberately introduced defects help create e-h pairs.

This perfectly CMOS compatible silicon APD utilizes the strengths of the p-i-n and avalanche photodetector. The p-i-n is designed so that the intrinsic region overlaps the waveguide. The detection region can also be made longer (an advantage of waveguide detectors) to increase responsivity further but this has the drawback of reducing the bandwidth due to *RC* time. The detector design has an oxide window opening through the cladding on top of the waveguide, which allows for ion implantation to take place. The defects (an inert ion at low dose) allow for defect enhanced detection, which increases detection [19]. These defect mediated waveguide detectors use a defect trap energy state that lies between the conduction and valance band in order to generate e-h pairs even outside the silicon band-gap energy limit [58]. These detectors were shown to detect at 20 GHz bandwidth [59] at wavelengths of 2 µm [19].

Chapter 3

Methodology

3.1 3D Printing

3D printing technology (certainly with minimum feature size of several microns) has matured significantly over the past 10 years, and has become accessible to consumers with lower entrance cost bringing prototyping to the masses. There have been several efforts to 3D-print at the micro and even nano-scale, and while these technologies are promising, they are still relatively expensive and inaccessible. Macro-scale 3D printing can still have a very important role in a photonics lab, including experimental set-up manufacture.

Choosing an appropriate printer for this work involved deciding between the two main options, fused deposition modeling (FDM) and stereolithography (SLA). Many factors contribute to the choice of printer, the first and most important is simplicity. The ease of use of the printer is paramount for an academic setting, where user turnover (student turnover) is rather quick (Master's students done in 2 years, PhD students in 4 years, not to mention undergraduate students that might need to use the device for a summer). In this aspect, FDM was an deemed a better choice, as the polylactic acid (PLA) filament is non-toxic, there is little cleanup to do, and prints can be larger and their design can be simpler. SLA printing uses a UV-curable resin, which requires latex or nitrile gloves to touch safely and emits toxic fumes. This type of printing is liquid-based, and because of this, is vulnerable to splashes and leaks leaving a mess that requires careful cleanup, as well as a post-print curing process. Furthermore, design of prints usually requires extra care to add drains in closed regions as to not have liquid pooling resin stuck inside the finalized print. Therefore, FDM printing is much more welcoming to new and hardened users alike.

One of the most welcome outcomes from the progress in 3D printing is the variety in choice a consumer has when it comes to printer brands. There are multiple different options available. The ease of use is paramount for an academic lab, but so is cost and reliability. Reliability and ease of use are on opposite ends of the spectrum to cost when it comes to availability, as most low-cost printers are somewhat unreliable, while the very expensive ones are locked-down (not modifiable, proprietary parts, hard to service) but work much more reliably due to this. A balance between these requirements is found in the Prusa Mini+. This printer was chosen for its reliability, user-friendliness, quality, software integration, features, open-source nature, and price. For a cost of about $400 USD, the semi-assembled FDM printer was purchased and set up.

The basic mechanism of a 3D printer, seen in Figure 3.1, is that it draws plastic filament (PLA in this case) from a spool, pushed by an extruder mechanism. There are two types of mechanism in FDM printers, direct-drive and bowden, based on where the extruder stepper motor is placed. The Mini+ is a bowden extruder printer, so the filament is fed directly into it. The extruder motor (and gear) pulls the filament from the spool, all the way to the hot-end through a "bowden tube". These tubes are often Polytetrafluoroethylene (PTFE), and have a very smooth surface and provide less friction for the filament to pass. When the filament reaches the hot-end, the temperature starts to rise due to the heating elements. The heaters are in charge of bringing the temperature

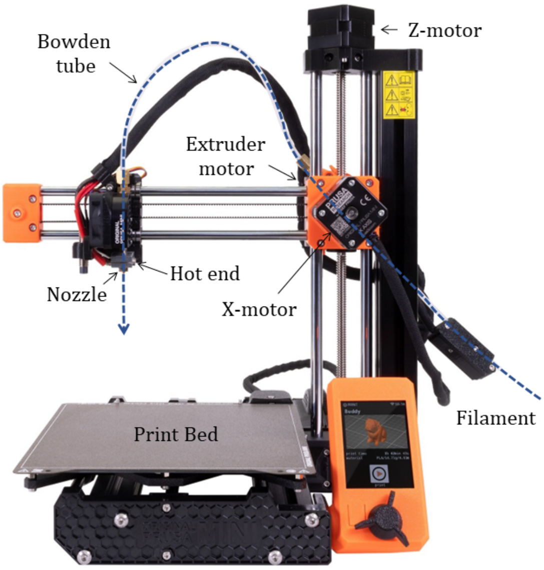

FIGURE 3.1: The Prusa Mini+ with filament path and labelled parts [60].

to about 200 °C, and melt the incoming filament. The liquid filament then goes through the nozzle, which narrows down the liquid to a 0.4 mm diameter (dependent on nozzle size). The hot-end assembly is moved in Cartesian coordinates (x-y-z) with another three stepper motors (the y direction is often the print surface itself that moves). The x and y directions are moved using timing belts and pulleys, while the z direction uses a lead screw rod and therefore achieves sub-0.1 mm layer thicknesses. For the first layer, all material expelled by the nozzle should meet the print surface (bed), which is often heated, for better adhesion.

Unlike injection-molded plastic (for example), 3D printing is an additive manufacturing process, meaning material is placed layer on layer, upwards. Thus overhangs are not possible unless arrangements are made for support material. Design of process is critical for the printing process. For example, it was found on multiple occasions that as extrusion happens, walls become slightly thicker than expected, and therefore material is slightly more than designed. This causes parts with low tolerance, such as screw threads

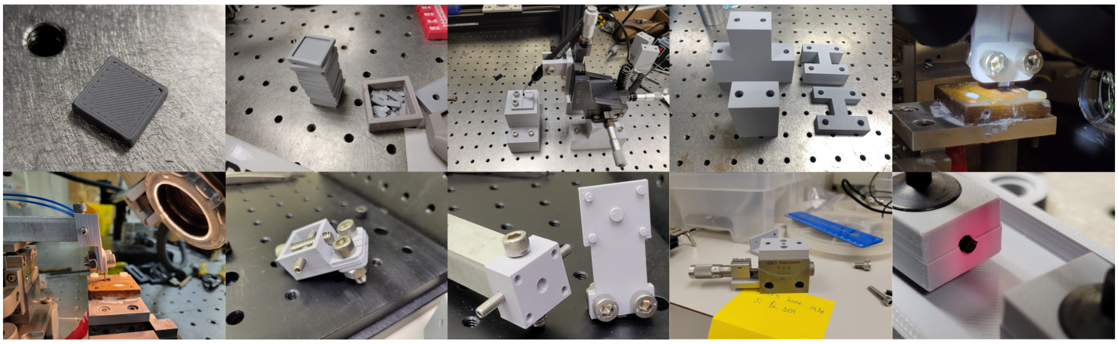

FIGURE 3.2: Examples of parts designed in gray, printed and used in the lab. First row from left to right: surface testing, epoxy test stages, xyz stage and vacuum tweezer holder, packaging stages, fiber array holder. Second row from left to right: side-view of fiber array holder, new version of fiber array holder, old version of fiber array holder, goniometer screw adapter, plastic fiber V-groove prototype

(especially internal threading), to be smaller than anticipated. Designs were made in computer-aided design (CAD) software, Autodesk FUSION360 [61], similar to INVENTOR [62], but lighter and less feature-rich, but more than adequate for 3D printing. Models are created parametrically in this software, where each dimension is specified. An `.stl` or `.3mf` 3D model file is exported from the CAD software and is later imported to a slicer. Slicers convert 3D models to `.gcode`, a file that is essentially a set of instructions, taking the exact printer and its limitations in mind, as well as many other parameters the user intends to set. The term slicer is used as it slices the model into several layers in order to be printed. The slicer used is PRUSASLICER [63], but UltiMaker CURA [64] was also tested. These slicers allow for several settings to be tweaked, knowing the printer and having experience with it are key to understanding what settings will and will not work. The defaults can work well in some situations, but to save time, filament, and obtain better print quality, custom settings should be adopted. Several parts were printed throughout the Master's, all of which served a purpose in the lab. Just some of these can be seen in Figure 3.2.

3.2 Silicon Photonic Chip Fabrication

The photonic chip fabrication was touched on in Chapter 1, but more details will be covered here. In general, chips are not fabricated at McMaster, but at a professional photonic fabrication facility (fab). This is considered best practice in modern chip manufacturing, ensuring high quality chip fabrication, and restricting researcher effort to design, simulation and test. Even so, below is a broad description of a general fabrication flow.

The first step in any silicon fabrication is to obtain the silicon wafer. Silicon wafers (and some other materials) are usually created with a process called the Czochralski method, which involves growing a long boule (a cylinder) of mono-crystalline silicon. This process is done by melting silicon and placing in the melt a "seed crystal", which is slowly pulled up from the molten silicon. The positioning (angle) of the seed is imperative, as it determines what crystal orientation the silicon wafers will grow. The parameters of growth can be set to make the boule be of different diameters. Doping can also be induced during the growth process in order to make wafers p or n-type. The boule is sawn into multiple wafers of the same diameter, at a desired thickness. They are then polished on the top side for minimal surface roughness.

Silicon-on-insulator (SOI) wafers are mainstream in photonics, and are created with the SmartCut process. This process involves a silicon wafer (one created with the Czochralski process described above) oxidized [14] with the thickness that one wants for the buried oxide (BOX) layer (usually 2 µm). After this, a hydrogen ion implantation is performed through the SiO_2 layer at a depth of slightly more than 220 nm, and a handle wafer (a normal silicon wafer) is bonded to the oxide side. Flipping the wafer with the handle area in the bottom, the temperature is increased to create microcavities from the previous implant, weakening the wafer and separating the top side [15]. Polishing is done where the separation occurred, and a wafer is left, with a 220 nm thick silicon layer on a 2 µm BOX layer, all sitting on a silicon handle wafer (usually around 600 µm, but dependent on wafer diameter).

With the wafer created, device fabrication is performed using a combination of masking and either etching or depositing. Each layer in a silicon PIC is essentially a mask. This determines which areas will get etched or deposited with material, and which will not. There are two options for masking. Photolithography (PL) uses ultraviolet (UV) light (deep UV in some circumstances) to expose certain parts of a photoresist. This requires a mask to be made for every layer desired, usually a glass mask with chromium on one side. Because of the limited wavelength of light used, diffraction becomes an issue, limiting resolution, and therefore, minimum feature size. But, because of the possibility to expose a whole wafer at once (or large parts at a time), this type of lithography is known as parallelized, making it a good fit for a high-throughput. Another option in lithography is electron-beam lithography (EBL). This has an electron beam that focuses on an electron-sensitive resist, for example PMMA (Poly-methyl methacrylate). The beam must go through the whole wafer to expose all desired areas. Because of this, it is often called a serialized type of lithography, which may not fit mass-manufacturing, but good for prototyping as no masks need to be developed. Electrons have a much smaller wavelength than UV light, which means the process resolution can be significantly improved.

The layers created by exposing and developing the organic resists stay during processing, as they are usually able to withstand etching and deposition. Post-process, the layers are removed through exposure to acetone.

The first layers to be created in a silicon PIC are the silicon waveguides. There are two layers that are dealt with, the silicon slab, and the silicon ridge. The fabrication process of waveguide creation can be seen in Figure 3.3. The silicon ridge is a layer that is left intact, this is where the full 220 nm will be left. The silicon slab regions are etched down by 130 nm to leave a 90 nm thickness. The rest is etched all the way to the oxide. These etching processes are done via deep reactive ion etcher (DRIE), following the Bosch process [13]. Extreme care must be taken with these layers as light is guided through them, surface roughness can cause drastic propagation losses. The DRIE is a type of reactive ion etcher (RIE) that is able to make much deeper trenches than traditional RIE systems. The Bosch process itself is often employed as it switches between standard plasma etching using SF_6 and adding a passivation layer to existing sidewalls, allowing for vertical walls rather than sloping walls.

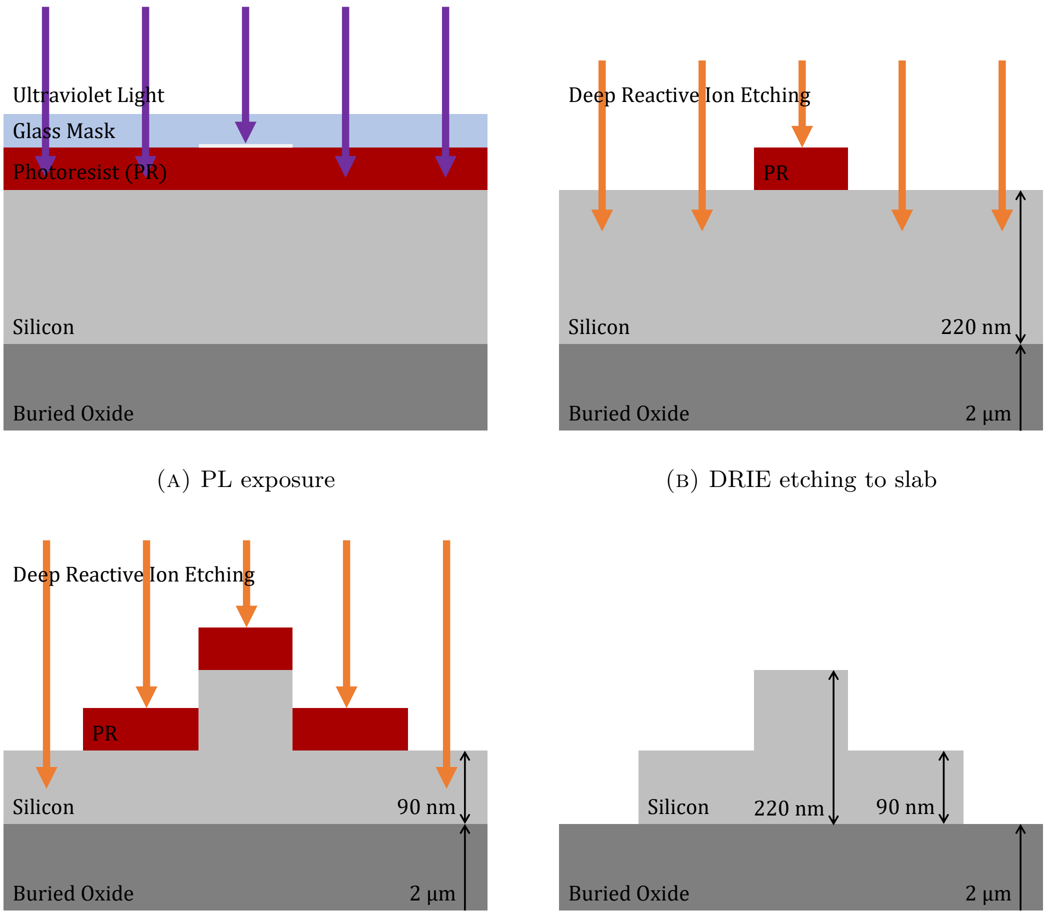

(A) PL exposure

(B) DRIE etching to slab

(C) DRIE to BOX

(D) Final rib waveguide

Figure 3.3: Fabrication process to create a rib waveguide.

After the silicon layer formation, doping is done. A PIC is said to have active components when such devices utilize doping. Doping of the silicon layers (both slab and ridge) is possible via ion implantation. Ion implantation accelerates ions of different species towards a target (the masked silicon wafer in this case), varying speed to determine depth (voltage or accelerating potential energy eV) and amount or concentration (ions per centimeter cubed cm^{-3} which is given as current when implanting). Usually the ions used for implantation are boron for p-type, and phosphorous for n-type. Different layers exist for a low concentration of doping, medium concentration, and high concentration, for each of p and n-type regions. Each layer is a different mask. The fabrication process for doping is seen in Figure 3.4.

Another layer that brings challenges is germanium. Germanium works very well as a photodetector, but is somewhat tough to epitaxially grow on silicon due to the lattice mismatch of both elements. The germanium layer is often grown via plasma vapor deposition (PVD). The germanium layer can also have a highly doped region of its own, for metal contact.

One of the most important layers for active devices is the metal layer, as it allows for electrical interfacing of devices. The metal layers often come in two, connected to each other, a low-level via that contacts down to the silicon, and a high-level via which serves as a contact pad and reaches the surface. One of the metal layers is often of very low resistivity, the other slightly higher. Furthermore, metal heaters exist, not touching the silicon layer itself, but sufficiently close to affect the temperature of the silicon near it. The heater layer is also another metal layer, but usually has much higher resistivity (for creating heat by consuming power) and is connected to the top-most metal layer. The heater layer, as it is not a via, does not have much thickness, unlike the other metal layers. The deposition of metal is achieved via sputtering or PVD. To deposit such 3-dimensional via structures, and ensure the heater is "floating" on top of a waveguide

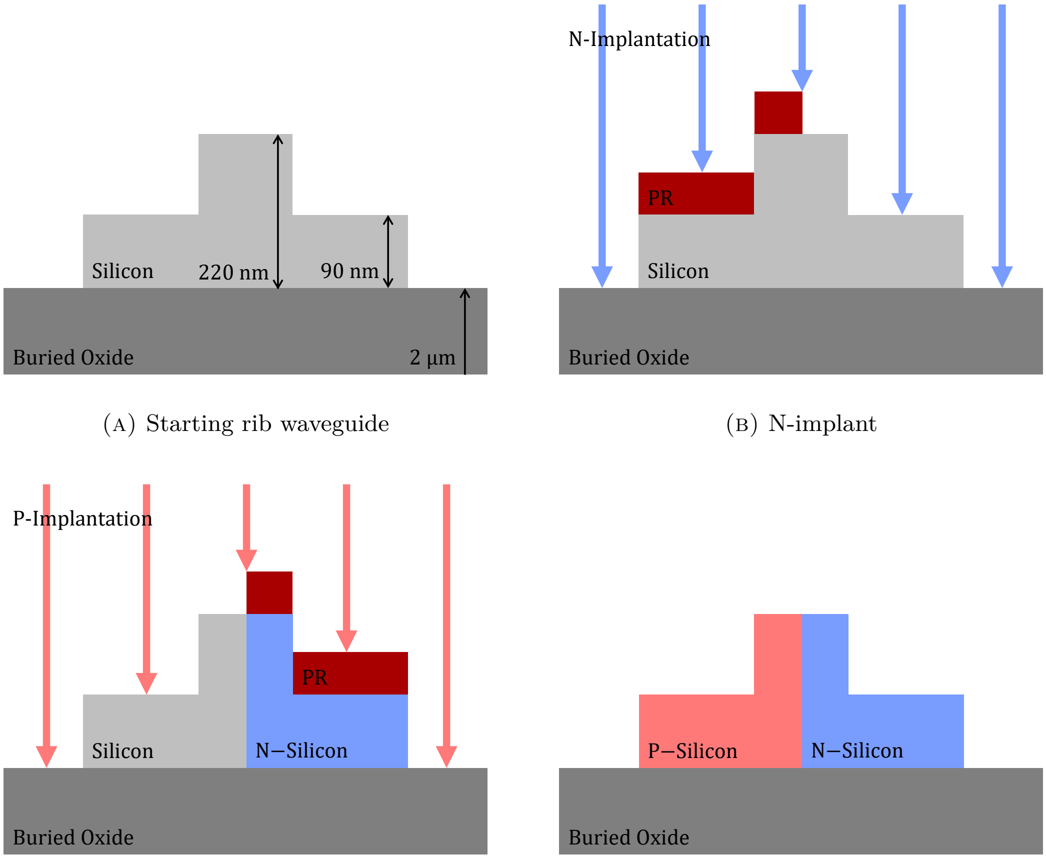

(A) Starting rib waveguide

(B) N-implant

(C) P-implant

(D) Doped rib waveguide

Figure 3.4: Fabrication process to implant a rib waveguide.

but is far enough to not attenuate light going through the silicon, SiO_2 is deposited after each layer of metal, including to fabricate the cladding of the waveguide. The creation of metal vias down to the silicon waveguide with no other metal layers can be seen in Figure 3.5.

In order to connect to the metal pads at the surface of the chip, one must open the oxide layers. This is called an oxide opening. One can also make these oxide openings down to the silicon, if one wishes to post-process the silicon layer. This oxide etching can be done using hydrofluoric acid (HF), a wet etch process, but many foundries have their own dry-etching processes for oxide as well. A more niche layer is the trench layer,

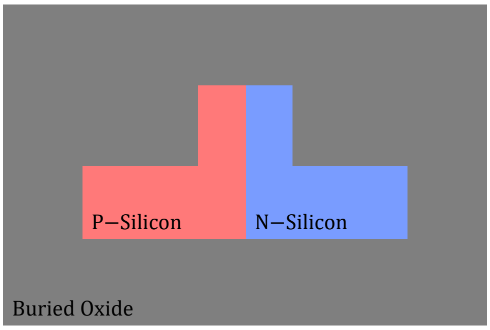

(A) Oxide cladded doped rib waveguide

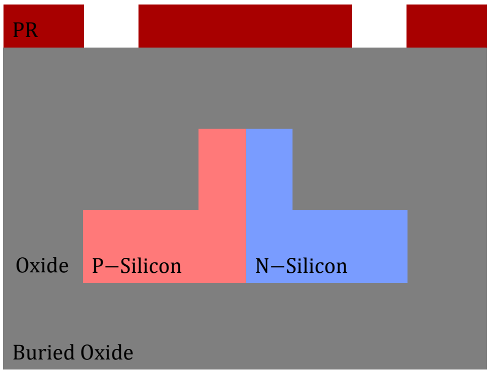

(B) Resist windows opened

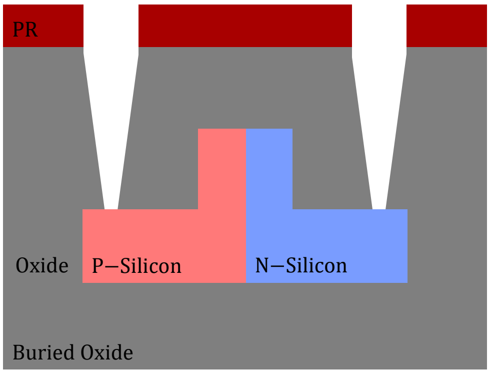

(C) Oxide etched down to waveguide

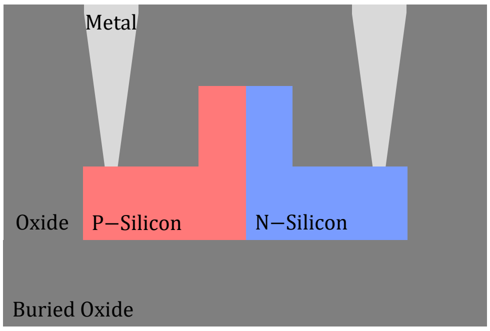

(D) Metal deposited and vias created

FIGURE 3.5: Fabrication process to create metal vias.

which essentially etches the oxide cladding, buried oxide, and any silicon. The trenches are likely made with a DRIE processes. These trenches can add thermal insulation, or can simply make it easier to dice the chip. Trenches can also be used in edge-coupling as they often create a good facet with which to couple into waveguides from a fiber.

It is important to note that all layers are masked, each mask with its own minimum feature size. Metal and trench layers have quite large minimum feature sizes, and even have minimum feature distances between themselves and other layers (exclusion distances). Metal layers also have minimum overlap so connection between them is assured. There are tolerances and limits imposed by the foundries in many of these layers, and to do anything outside the restrictions can lead to design rule check (DRC) errors. Some facilities will give the option to challenge the DRC in some aspects. One requirement some DRCs have for all chips is silicon and metal tiling. These are a pattern of squares throughout the surface of the chip in areas where the silicon or metal layers do not exist, in order to have sufficient density to ensure process uniformity.

The work presented in this thesis mostly has chips designed for fabrication via Advanced Micro Foundry (AMF) of Singapore [65]. The services provided by AMF make active devices possible, and use PL. In contrast, some devices designed throughout the degree were fabricated by Applied NanoTools Inc. (ANT) of Alberta [66], which does not dope devices and also does not give access to rib waveguides (do not create a slab), and use EBL. All fabrication runs are brokered via CMC Microsystems, a non-profit organization that enables subsidization of fabrication runs with many foundries, for companies and researchers in Canada. All fabrication runs participated in through CMC Microsystems were multi-project wafers (MPWs), driving costs down further, and also included expert advice and counseling when designing.

Once an MPW is complete, it has several chips belonging to multiple different customers. In order to dispatch the individual chips, dicing is performed. Wafer dicing is a process that involves a dicing saw, a saw blade with a small diamond grit that cuts through silicon in a straight line with a somewhat thin profile. The dicing can be performed to separate many chips after an MPW fabrication run. Dicing can be used to create facets for coupling, but can leave much to be desired in terms of facet roughness, and therefore trenching is still preferred. Once diced, the chips are ready to be shipped.

A post-processing step that was performed on several chips was wire bonding. This entails attaching the PIC onto a printed circuit board (PCB) and wire bonding from the pads on the silicon chip to the interconnects on the board beneath, soldering wires that go from the PCB to the measurement instrumentation.

3.3 Measurement

There were multiple measurement setups used in the course of this work. A brief description of all instrumentation used will be given.

3.3.1 Equipment

The most important and most-used equipment in all measurements were optical fibers. In photonics, it is imperative to see how light interacts with different components, devices and processes, and the optical fiber serves as an interconnect to move light from an output to an input. The fibers used are single mode fibers (SMFs), with FC/PC (flat) or FC/APC (angled) connectors. These connectors should ideally be matched with the type of connector it is coupled to, in order to ensure minimal loss. When fibers have connectors on both ends, they are typically called “patch cables”, which connect two devices. One can also cleave the fiber at any point to have a bare fiber exposed. This can be useful for interfacing with a chip directly, for coupling. This involves cutting through the jacket, cladding, and fiber core, and cleaving the core for a flat facet. In measurement setups, tapered or lensed fibers are used, as they focus the light to a small point and lead to lower coupling losses. Fibers are put on an x-y-z stage and edge-coupled to a device under test (DUT). In conjunction, polarization paddles are used between the laser source and the DUT, as a specific polarization can be set by the paddles, and minimize losses within the PIC.

The most commonly-used optical source was the tunable laser. The tunable laser used in these measurements was the Agilent 8164B, which has two laser outputs, and two or four InGaAs detector inputs. The tunable laser outputs a specific desired wavelength of light at a desired power output (up to 8 dBm). The device is able to sweep the wavelength setting and therefore provide a broadband view of an optical spectrum at the detector. This device, like all others listed here, allows for instruction via general purpose interface bus (GPIB), which can be interfaced with the programming language of choice; in this case Matlab.

Another well-used piece of instrumentation was the source-meter. The ones used were the Keithley 2400. This device can apply a DC voltage or current, and read the resulting current or voltage respectively. These were generally used as voltage sources, and ammeters. These devices are very useful for applying a bias to heaters, detectors, and even modulators in DC for testing.

Two devices used for radio frequency (RF) measurements were the vector network analyzer (VNA) and electrical spectrum analyzer (ESA). The VNA was used to measure the amplitude and phase of a signal. The VNA output RF signal (frequency can be set) comes out of port 1 and is encoded to see how much of it is transmitted to the input port (port 2), which can determine how much of it was reflected (amplitude) and can also determine less common measures, like phase. The transmission (gain or loss) is known as S_{21} as the signal goes from port 1 to 2, and the reflection is known as S_{11} as the signal goes from port 1 back to 1. This instrument is extremely important for optical delay measurements, but is much more accessible than an Optical VNA [67]. The ESA on the other hand is helpful in finding the frequency response of an input. It sweeps in the frequency domain and displays the output amplitude. Unlike a VNA, this device cannot measure phase as it generally does not have an RF signal output (if it does, it is not encoded), just an input. Essentially, an ESA displays absolute RF power detected, while the VNA can measure relative power and phase. The VNA used was an HP 8719C, and the ESA was a RIGOL DSA 815.

A useful device that was used in all optical delay measurements was a thermo-electric cooler (TEC). These devices can maintain the temperature of a stage, thus avoiding drifting of the resonance point of devices, especially ones that are highly susceptible or sensitive to temperature differences. The TEC used was an ILX Lightwave LDC-3742.

Useful parts for any electrical measurement are point probes. When a chip is not wire bonded, it is necessary to make contact to the small (often 75×75µm) metal contact pads. DC probes allow for x-y-z axis movement of a metal needle that can touch the metal pads on the PIC lightly. The other end of the DC probe connects to a voltage source, and a bias is applied. Each source meter needs two DC probes to connect to a chip, which can be obtrusive and crowded, so wire bonding is a good approach to removing clutter. An RF probe was also used for measurements of the ring modulator, as the DC probes are not designed to handle RF speeds. To apply a DC offset to any RF signal when connecting to a modulator, a bias tee is used, which allows for a DC and RF input to be added into a combined output, which can be fed into the RF probe.

For RF measurements, extra components can be added. An external modulator, for example, is used before the input into the chip, in order to test phase difference of the delay elements. An external photodetector allows for bypass of internal silicon or germanium photodetectors. The photodetector detects light coming out of the DUT and outputs a DC or RF signal. RF amplifiers can also be added between the photodetector and the VNA or ESA in order to increase signal power.

3.3.2 Setups

The most commonly used optical setup used light from the tunable laser passing through polarization paddles, into the DUT, and detecting it back at the laser module. A source meter can be connected to the DUT when applying a DC bias to a heater, detector or modulator (for DC operation). Figure 3.6 demonstrates this optical setup. In blue lines are the optical connections (which have directionality) made with SMFs, in orange are DC connections made with regular cables, and in green are RF connections made with coaxial cables.

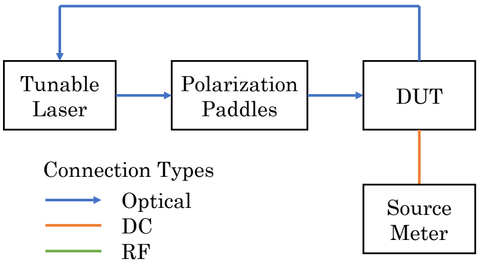

FIGURE 3.6: Optical setup with optional DC connections.

The complexity of the setup increases when measuring optical delay, not using an internal modulator, seen in Figure 3.7. This was done for delay ring phase measurements. The same output from the polarization paddles and tunable laser is input to an external modulator instead of the DUT itself. This allows for the VNA to modulate the signal going to the DUT using the external modulator rather than the internal ring modulator, and allows for the VNA to later compare the output and input RF signal. The modulated and delayed light goes from the PIC DUT into an external photodetector, and the RF output is amplified by an RF amplifier, and sent to the VNA. The external photodetector and RF amplifier require power to function. The physical setup is pictured in Figures 3.8 and 3.9.

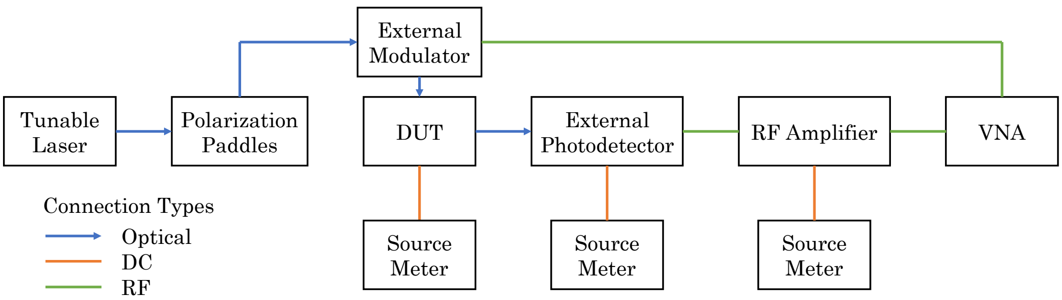

FIGURE 3.7: RF setup with VNA measuring delay ring optical delay.

The external modulator was replaced by an RF probe when the internal ring modulator was tested, shown in Figure 3.10. Here, the same setup remains, but the VNA

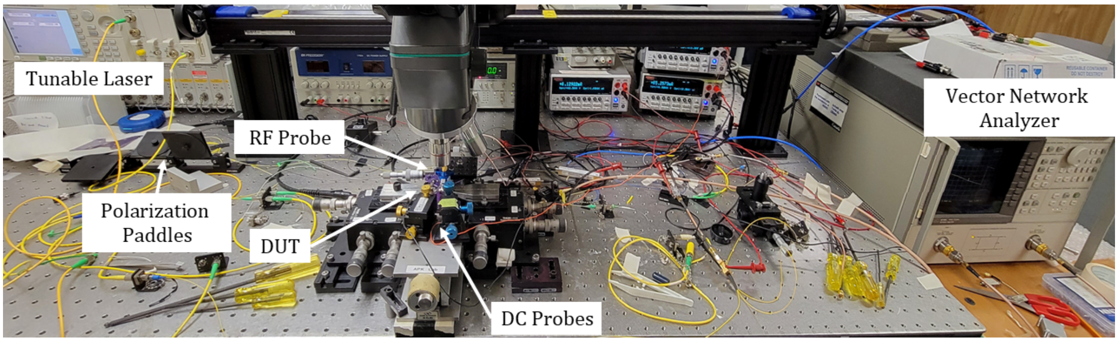

Figure 3.8: Physical RF setup with VNA.

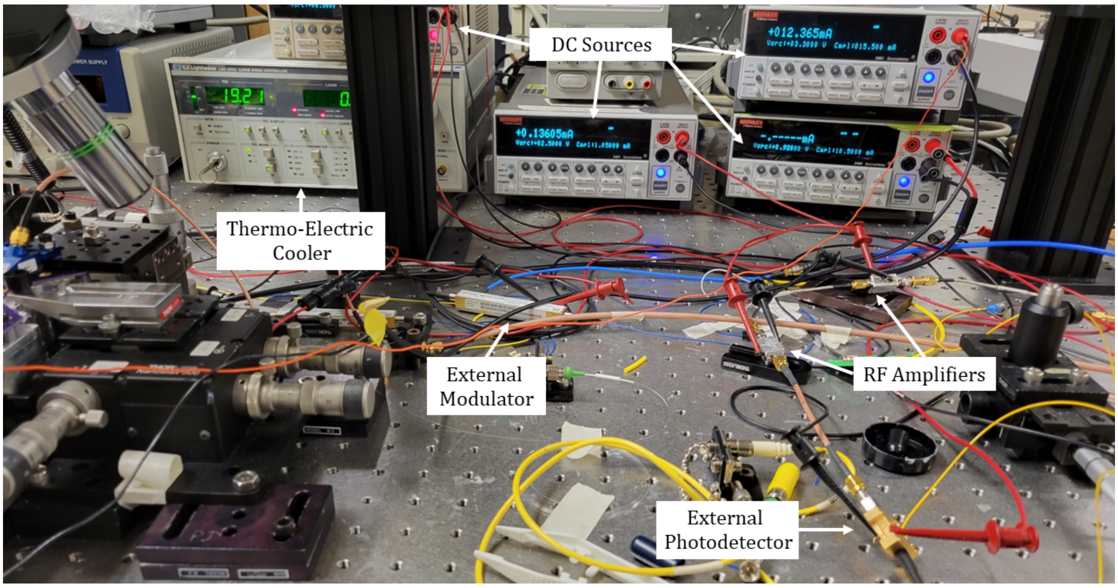

Figure 3.9: Other components used in RF setup with VNA.

sends its output through a bias tee, into an RF probe, which sits on the chip's contact pads. The bias tee combines the bias from a DC voltage source and the RF signal from the VNA to form an offset RF signal for the RF probe. This allows for the micro-ring to be modulated at any DC offset bias desired. The bandwidth of the ring modulator was tested with this setup, at different bias voltages.

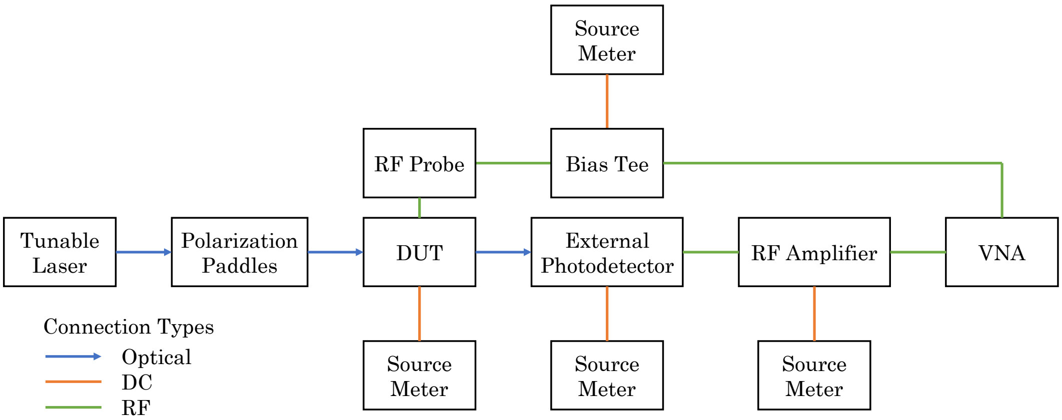

FIGURE 3.10: RF setup with VNA measuring properties of ring modulator.

The final setup shown in Figure 3.11, involves an ESA rather than a VNA to measure the RF response at different wavelengths at different biases. Here, the RF amplifier was not needed, as the photodetector output was good enough for the ESA to detect. This ESA has an output of 10 MHz for convenience.

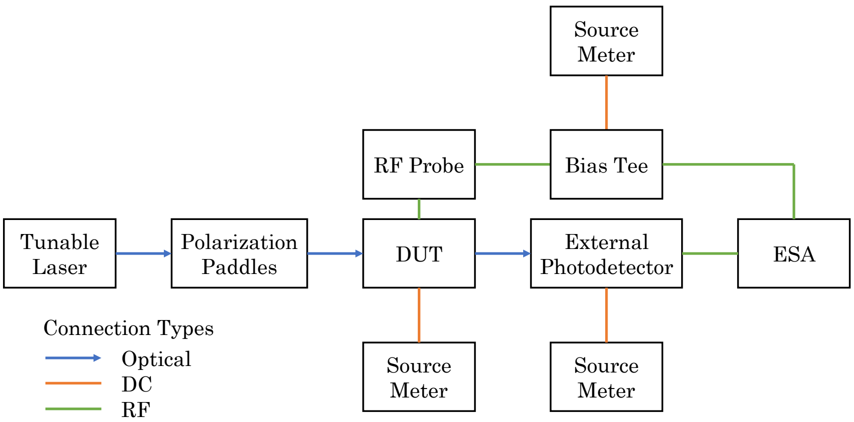

FIGURE 3.11: RF setup with ESA measuring response of ring modulator.

Chapter 4

Experimental Verification of OBFN Components

4.1 Introduction

An optical beamforming network (OBFN) is a system that utilizes photonics to add phase delays of different magnitudes at multiple output antennas. The product of such system is a phased-array, shown in Figure 4.1, which can change the resulting angle of an output signal using several antennas. Microwave photonics (MWP) OBFN systems consist of a device that up-converts the radio frequency (RF) signal to the optical domain, applies true time delay to the signal, and down-converts it back to RF [10]. The photonic integrated circuit (PIC) designed in this work is represented in Figure 4.2, and it incorporates a ring modulator for up-conversion and a delay ring for true time delay. An OBFN is usually comprised of more than one time delay in order to produce a required output signal [43], but for the purposes of this work, a single time delay device was used.

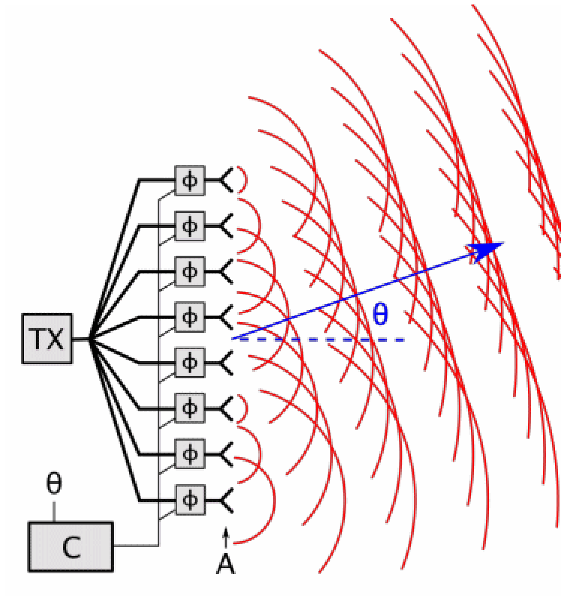

FIGURE 4.1: A phased-array of antennas, where the signal TX is delayed at every antenna by phase φ. The phase at each antenna produces an angle ϑ for the resulting planar wave produced [68]. Reproduced from Wikimedia Commons under Creative Commons license.

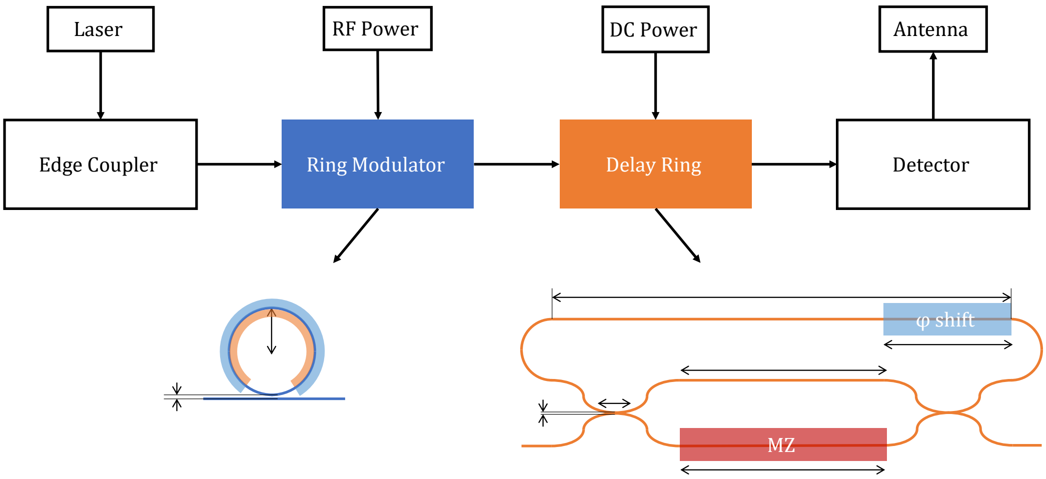

FIGURE 4.2: A schematic of the OBFN on the chip, with a ring modulator and true time delay device.

4.2 Ring Modulator for RF Generation

An important factor in an OBFN is modulation, where information is up-converted from the RF domain to optical. Modulation is key, along with detection, to determine the quality and maximum bandwidth of the signal output of the PIC and therefore phased-array. To avoid external modulation, which can be performed by somewhat large devices (compared to a silicon PIC), this component was embedded in the PIC itself, in the form of a ring modulator. The ring modulator for the purposes of OBFNs discussed in this chapter has specific requirements and performance targets, which are discussed in the design section, and tested for in the performance section.

4.2.1 Design

A micro-ring modulator was chosen to perform modulation because of its small footprint compared to alternatives. Space savings is a large driver for performing modulation on-chip. A Mach-Zehnder (MZ) structure would use millimeters of chip length as opposed to microns for an optical ring resonator (ORR) structure (not to mention the power efficiency that comes with the smaller form factor) [17].

There are a several characteristics that the ring modulator needed to satisfy for the requirements of an OBFN. Firstly, the modulator needed to provide a strong modulation depth, for the strongest signal-to-noise ratio (SNR). Forward bias operation is where this strong modulation depth usually happens [55]. Forward bias is almost unheard of when dealing with modulation, especially ring modulators due to the slower bandwidth possible, which is dependent on silicon's electron recombination time (diffusion current takes over in forward bias) [17]. Forward biased ring modulators have been modulated at speeds of 900 MHz [69] (reaching 10 Gbps with feed-forward pre-emphasis [69][70]), compared to reverse bias speeds of 128 Gbps [71]. Luckily, high-bandwidths are not necessarily required for some applications, including the specific application being pursued, satellite communication. The traditional K_u band for RF satellite downlink communication (from the satellite) lies between 10.7 - 12.75 GHz [72], but this spectrum is divided into many transponders, usually with a bandwidth of 36 MHz [73] which is able to modulate at less than 20 Mbps [74]. In contrast, commercial fiber optic communication on the server side is in the 100 Gbps range [75]. Forward bias operation also comes with higher power consumption though, as a sizeable current flows through the device as opposed to reverse bias [76]. Linearity is looked for in modulation, to preserve signal integrity. Linearity allows for the modulated signal to faithfully represent the original electrical input signal, as non-linear systems would distort the input, albeit sometimes in predictable ways [56]. This predictability can be leveraged through pre-emphasis, where certain parts or frequencies of the signal can be boosted or suppressed in anticipation of the distortion or non-linearity to correct the output.

The work here is based on a ring modulator offered as an example during the SiEPIC (Silicon Electronic–Photonic Integrated Circuits) library, which was available to all Canadian silicon photonic researchers [77]. The ring modulator design consisted of n++, n+, n, p, p+ and p++ doped regions, with the n and p regions forming the junction, located in the center of the waveguide, and the heavily-doped n++ and p++ regions making contact with metal vias placed sufficiently away from the waveguide so as to not induce parasitic optical loss.

To better understand the electrical characteristics of the doped regions at different biases, Ansys Lumerical CHARGE [78] simulations were performed. The output of the simulations provided a charge carrier concentration mesh for the cross-section of the rib waveguide, shown in Figure 4.3. Plotted logarithmically, the charge carrier profile changes drastically during forward bias, due to the diffusion current. This change in charge carriers also affects the refractive index, described by the plasma-dispersion effect given by Equation 2.15, reproduced here [17]:

$$\Delta n(\lambda) = -3.64 \times 10^{-10}\lambda^2 \Delta N - 3.51 \times 10^{-6}\lambda^2 \Delta P^{0.8}$$
$$\Delta \alpha(\lambda) = 3.52 \times 10^{-6}\lambda^2 \Delta N + 2.4 \times 10^{-6}\lambda^2 \Delta P$$

The effect allows for modulation, which shifts the ring resonant wavelength by changing the number of charge carriers within the waveguide. The charge carrier information was then imported into Lumerical MODE [79], where the index of refraction at every point of the cross-section waveguide mesh was calculated, and the optical mode was simulated versus applied bias. This mode information was subsequently imported into Lumerical INTERCONNECT [80] where device-level performance was simulated using the transfer function of the ring modulator.

The simulated ring modulator transmission spectrum at different applied biases can be seen in Figure 4.4. The simulated ER is approximately 18 dB. Furthermore, the resonance change during reverse bias is relatively weak, which is due to the small change in the number of charge carriers seen in Figure 4.3a. In forward bias, a much more drastic change is visible, especially approaching the higher-end of bias applied. The higher the bias, the higher the current passing through the device, described by the Shockley diode equation, Equation 2.18 reproduced here:

$$I = I_s\left(e^{V/nV_T} - 1\right)$$

The current determines the change in charge carrier concentration, which affects the refractive index of the silicon waveguide. The resonance shift at 1 V forward bias, is more than 0.4 nm. What is even more interesting is the extinction ratio. A combination of the absorption and refractive index allows for an ER of almost 50 dB, which would lead to a very strong SNR performance during modulation. This combination also leads

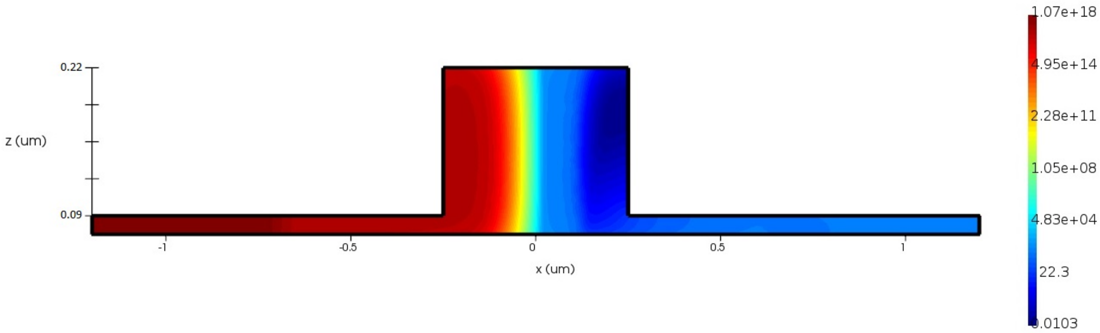

(A) 1V reverse bias

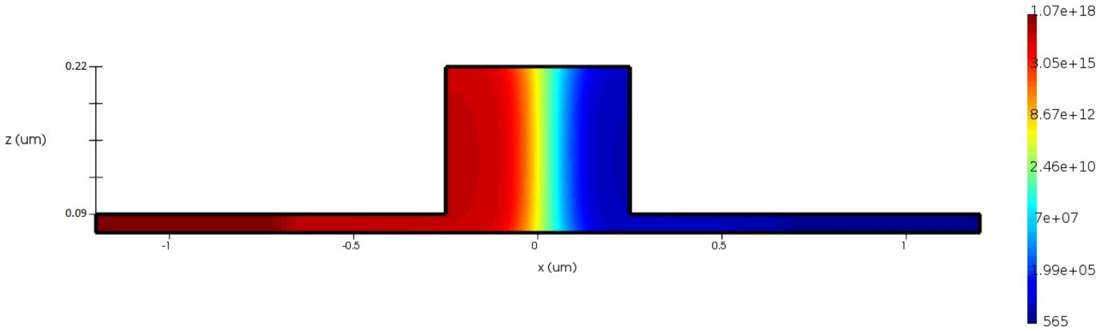

(B) 0V (no) bias

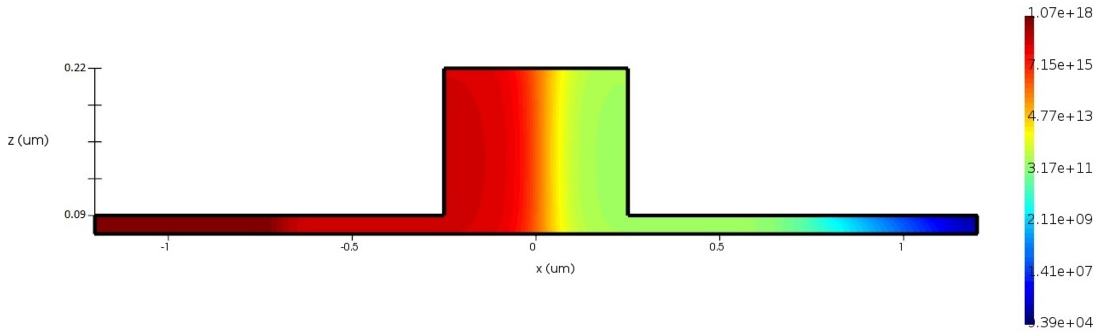

(C) 0.5V forward bias

FIGURE 4.3: Charge carrier concentrations at different applied biases.

to the fact that this ring is over-coupled at 0 V bias, and becomes critically-coupled at some point in forward bias. The over-coupling is obvious as adding loss to the ring causes a stronger ER.

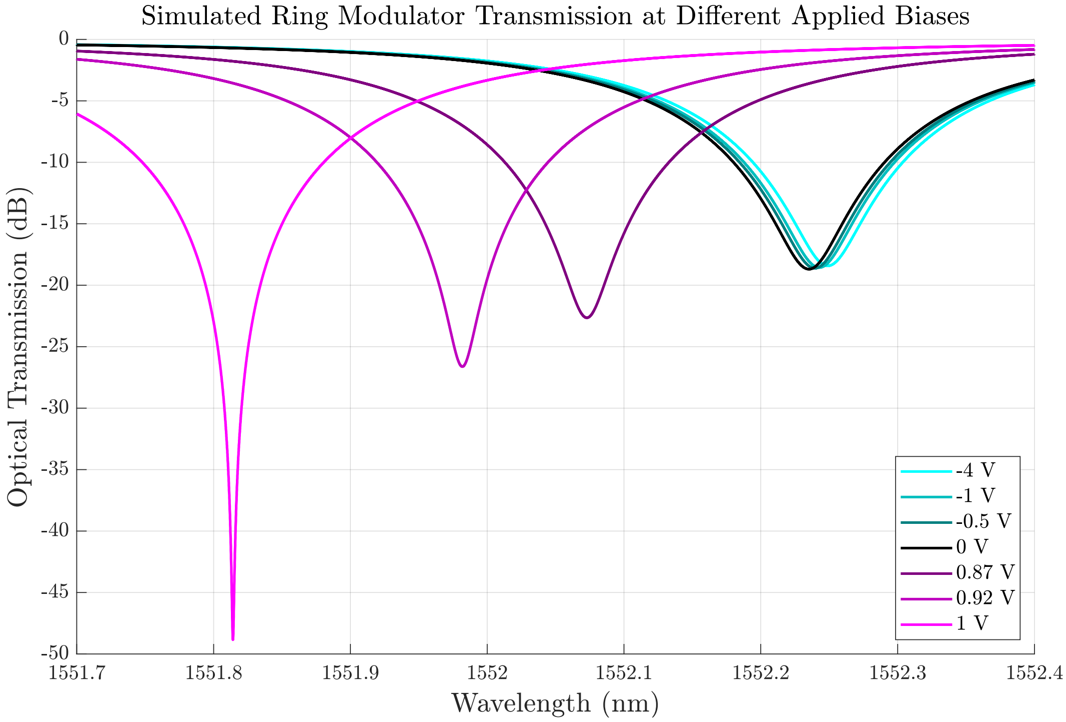

FIGURE 4.4: Simulated modulator transmissions versus differing biases.

The simulated transmission spectrum in forward bias direct current (DC) operation performed as desired. Subsequently, the bandwidth of the device in forward bias needed to be simulated. The limiting factor for bandwidth in a ring modulator electrically in reverse bias is the *RC* time (optically, it is the photon lifetime), but in forward bias, the limit becomes the recombination time for charge carriers in the silicon waveguide. The recombination time predominantly depends on the charge carrier itself (electron or hole), and the background doping of the p and n regions. Values for recombination time can vary widely, from 1 µs to 1 ns depending on these factors [81]. Figure 4.5 shows several simulations performed in Lumerical INTERCONNECT in forward bias with varying bias, modulation amplitude (peak-to-peak voltage V_{pp}), and modulation frequency. These graphs demonstrate how well a signal can be modulated with the pn regions that exist, and how frequency affects the output. Figures 4.5a, 4.5b and 4.5c show that at a forward bias of 0.5 V, and a V_{pp} of 0.1 V, there is not much difference between 100 MHz, 1 GHz

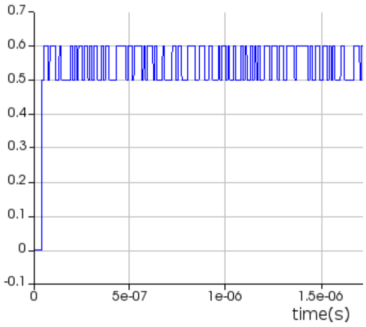

(A) B:0.5 V| A:0.1 V| f:0.1 GHz

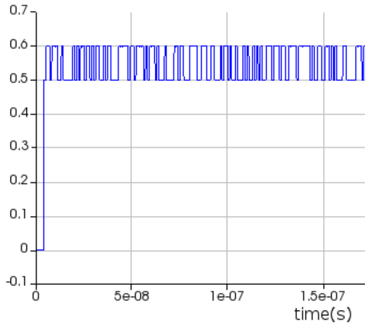

(B) B:0.5 V| A:0.1 V| f:1 GHz

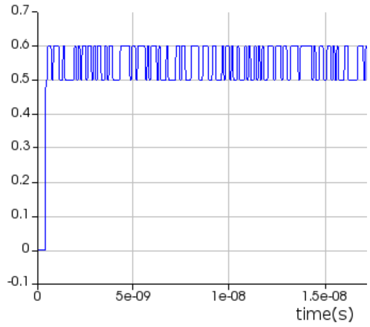

(C) B:0.5 V| A:0.1 V| f:10 GHz

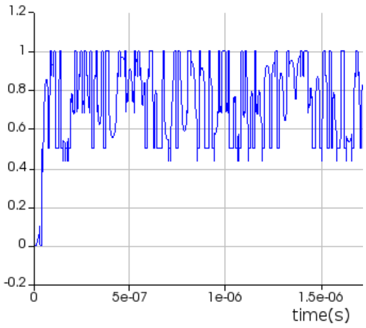

(D) B:0.5 V| A:0.5 V| f:0.1 GHz

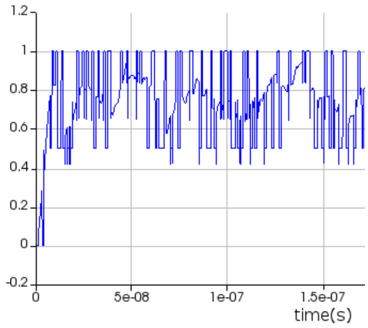

(E) B:0.5 V| A:0.5 V| f:1 GHz

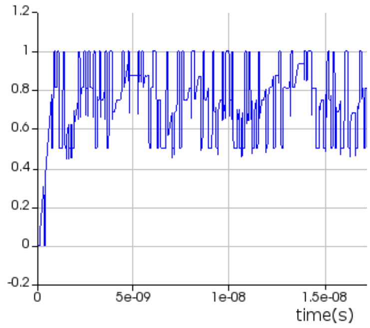

(F) B:0.5 V| A:0.5 V| f:10 GHz

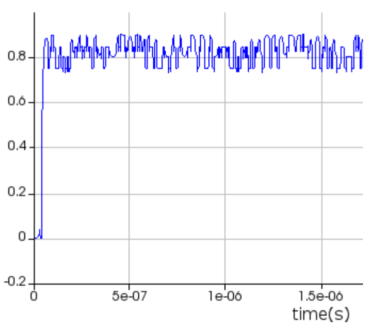

(G) B:0.8 V| A:0.1 V| f:0.1 GHz

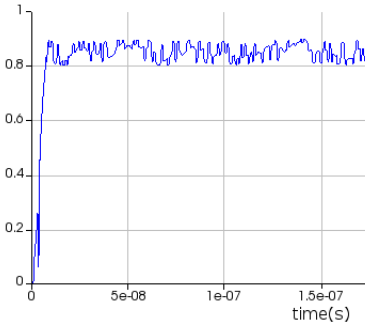

(H) B:0.8 V| A:0.1 V| f:1 GHz

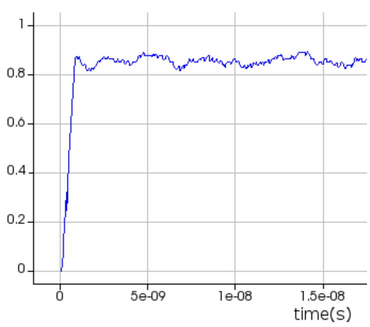

(I) B:0.8 V| A:0.1 V| f:10 GHz

FIGURE 4.5: Modulation at different biases, amplitudes, and speeds.

and 10 GHz. The modulation depth is quite minimal at 0.1 V V_{pp} at 0.5 V bias (shown in Figure 4.6 with 0.6 V represented by 0.64 V as it is close enough), and while the output signal is still quite clean at high bandwidths, it does not provide the modulation depth desired for low SNR. Figures 4.5d, 4.5e and 4.5f demonstrate the same parameters, but with 0.5 V peak-to-peak voltage, which is a large shift in resonance. With this comes problems with recombination time, as seen in all figures at this V_{pp}, the device struggles to reach 1 V. It is clear that a V_{pp} of 0.5 V is too large for forward bias. Another insight is that looking at all six results with a forward bias of 0.5 V, the bias appears to be too low to achieve much modulation depth without wildly increasing V_{pp}. A bias of 0.8 V was finally tested, at a V_{pp} of 0.1 V, shown in Figures 4.5g, 4.5h and 4.5i. This shift results in a somewhat strong modulation depth shown in Figure 4.6 (0.78 V and 0.87 V can be approximated to 0.8 V and 0.9 V respectively). It can be seen that frequency has a drastic effect on the modulation, recombination just cannot keep up with the modulation speed at 0.8 V, even at 100 MHz. From these results, the ring modulator was used, but the modulator bias and V_{pp} were kept in mind for performance measurements. A likely bias could be somewhere in the realm of 0.7 V with a 0.05 V V_{pp}.

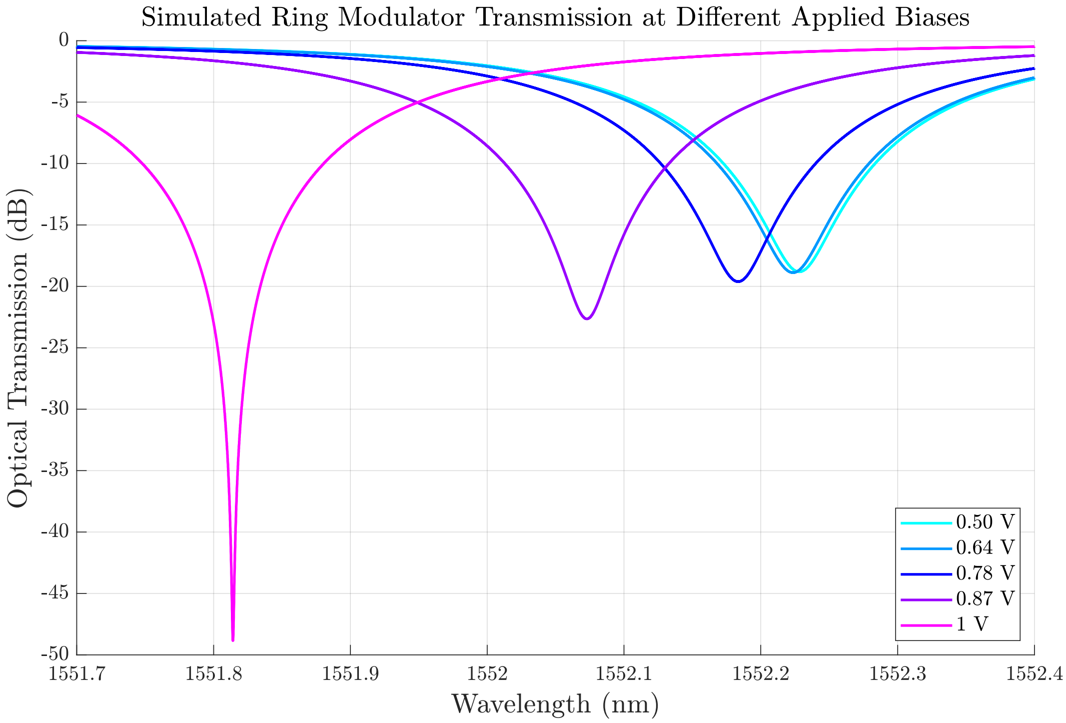

Figure 4.6: Simulated modulator transmissions at more biases.

4.2.2 Experimental Performance

The performance of the fabricated ring modulator was characterized via different methods. Firstly, the optical transfer function was measured. To test the ring modulator without the presence of the delay element (Section 4.3) transfer function overlapping, a 3 dB splitter was placed at the output of the ring modulator in the PIC, directly connected to an edge coupler.

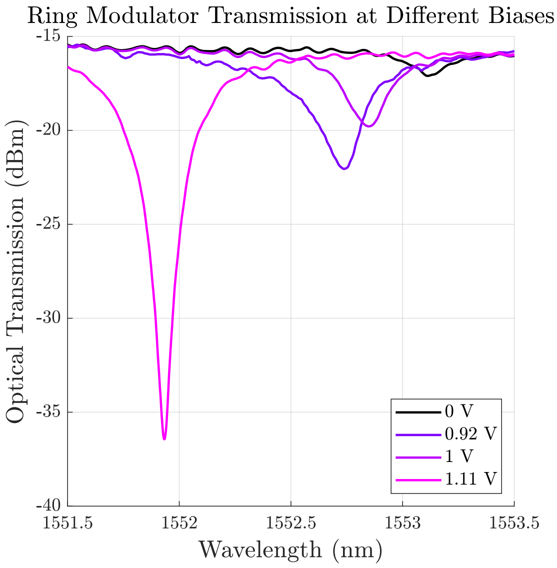

(A) Forward bias

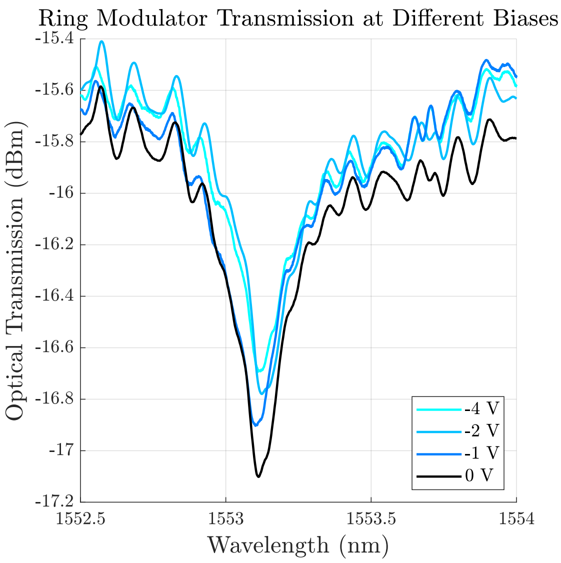

(B) Reverse bias

FIGURE 4.7: Measured transmission of ring modulator at different biases.

The measured transmission spectra of the ring modulator shown in Figures 4.7 closely resemble the pattern seen in the simulated transmission spectra shown in Figure 4.4. The idea that the ring was over-coupled and the additional absorption incurred at forward bias causing a large ER at around 1 V was verified. As with any physical measurement, the spectrum is not as clean or clear as in simulation, the noise ripple in the signal caused by the chip-length Fabry-Pérot cavity formed by the edges of the PIC [82]. The extinction ratios are also not as deep as expected, the whole spectrum is shifted by 0.8 nm, and critical coupling happens at a different bias. These discrepancies are due to lack of information in the simulation side. Temperature of the device is not the same as in simulation, and therefore the resonances are shifted (temperature was held at 19.2 °C using a temperature controller in measurements). The doping concentrations used in simulation were likely different than those used in Advanced Micro Foundry [65], which would also change where and how much ER is obtained. Internal resistance of multiple components can also cause applied biases to not reflect simulation. All these factors, among others, contribute to a mismatch with simulation, although the main trend is satisfied. As seen in Figure 4.7a, critical coupling is achieved at 1.11 V forward bias, and very small shift in resonance occurs in reverse bias shown in Figure 4.7b.

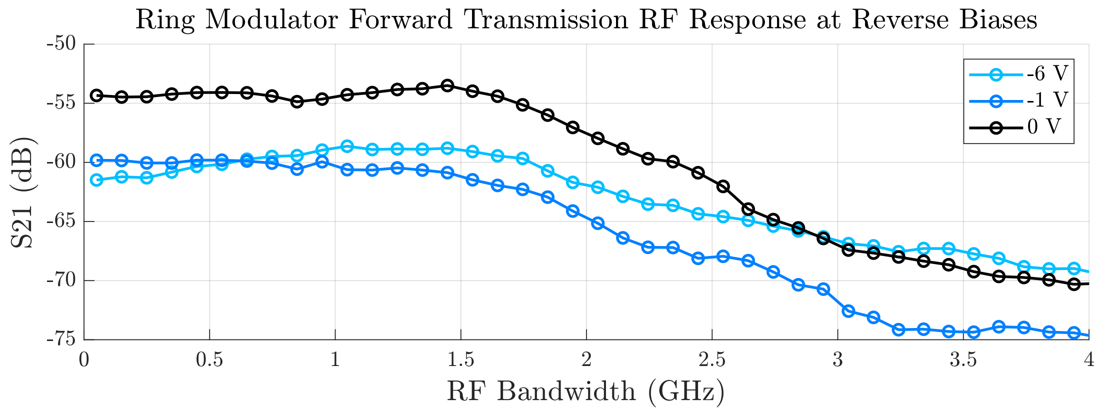

(A) Reverse Bias

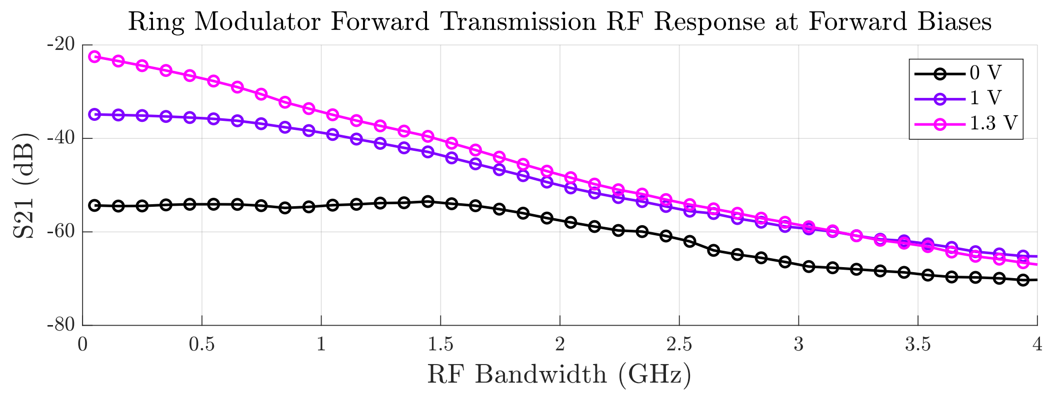

(B) Forward bias

Figure 4.8: Measured transmission of ring modulator at different biases.

Bias (V)	3 dB Bandwidth (GHz)
-6	2.5
-1	1.8
0	2.0
1	0.85
1.3	0.35

Table 4.1: RF bandwidths of ring modulator at different biases.

To better understand the electronic properties of the modulator, the 3 dB RF bandwidth was measured at different biases with a vector network analyzer (VNA). The measurements were made at the resonant wavelength of the bias being measured. The measurements can be seen in Figure 4.8 and summarized in Table 4.1. Forward bias 3 dB bandwidth collapses compared to the reverse bias counterpart. This can be attributed to the relatively long carrier recombination time. It can be seen in Figure 4.8a that the S21 measurement (forward transmission, signal comes out from port 1, through the device under test (DUT), and into port 2) returns very low power relative to input, in the -60 dB range, which is due to the very small shift in resonance at reverse bias, but also due to the very low ER at these biases. Both these add to produce low modulation depth. Nevertheless, the power remains somewhat static (hence 3 dB bandwidth too) for reverse bias till 2 GHz. Figure 4.8b shows the forward bias low-frequency RF response being larger than that of reverse bias, which is due to the deeper ER found in the ring's resonance point. However the 3 dB bandwidth is met quickly as the response worsens at earlier frequencies. From this data, the ideal operation of this ring modulator is at forward bias near 1 V, at a maximum bandwidth of 850 MHz. This bandwidth aligns with literature, also operating a ring modulator in forward bias with a 3 dB bandwidth of 900 MHz [69]. It is interpolated that between 1 V and 1.3 V, the bandwidth lies in the range of 500 MHz. This bandwidth is sufficient for the 36 MHz transponder bandwidth for the K_u band [73]. To up-convert the 36 MHz frequency up to the K_u band carrier wave of 10.7 - 12.75 GHz [72], a waveform generator and mixer can be embedded in the

PIC as well [35].

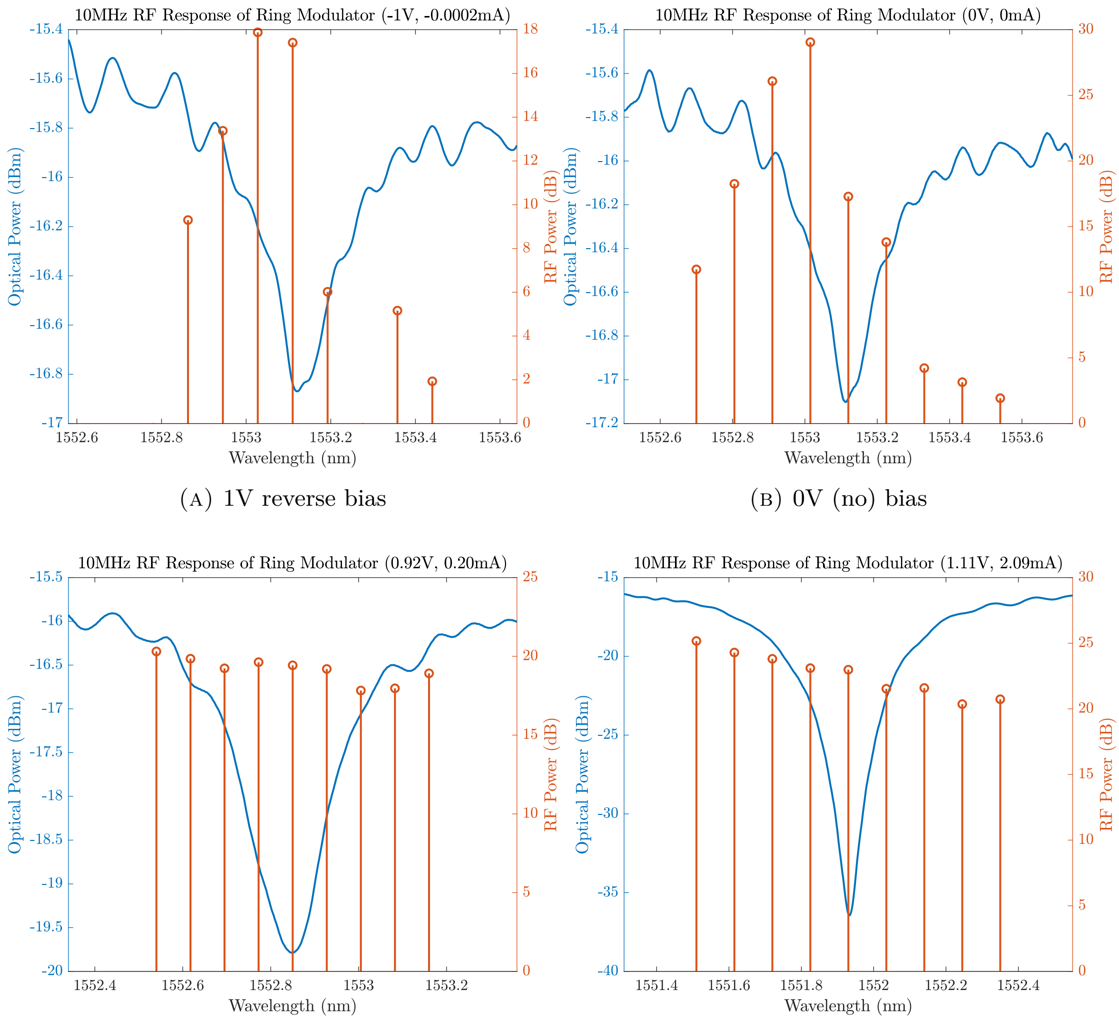

(A) 1V reverse bias

(B) 0V (no) bias

(C) 0.92V forward bias

(D) 1.11V forward bias

FIGURE 4.9: RF response at points of the optical transfer function.

An electrical spectrum analyzer (ESA) was used to characterize the RF response of the ring modulator at different bias with the modulator operated at 10 MHz. Figure 4.9 demonstrates the 10 MHz RF power (with noise subtracted) at different wavelengths on the optical transfer function. The ESA output 10 MHz sinusoid signal was $V_{pp} = 1.4\,\text{V}$. These measurements allow for understanding how well the input electrical 10 MHz sinusoid translates to the optical domain, and how well the modulator up-converts the signal. With this, the optimal modulation point on the transfer function can be found. As seen in Figures 4.9a and 4.9b, the RF power severely decreases at the red side of the spectrum, due to thermal instability (ring modulators are always modulated on the blue-side in the field [83]). Figures 4.9c and 4.9d show the forward bias measurements. There is little difference in RF power throughout the spectrum, and power values are significantly higher than in reverse bias. This is due to the large modulation amplitude, at 1.4 V, the resonance shift at forward bias is very large, so the whole of the transfer function yielded an RF response. At the same time, there should be a clear difference in RF power between the resonance point and flat transmission regions, as points at the edges of the measured regions should have little to no power difference. To understand these mechanics better, more measurements needed to be made.

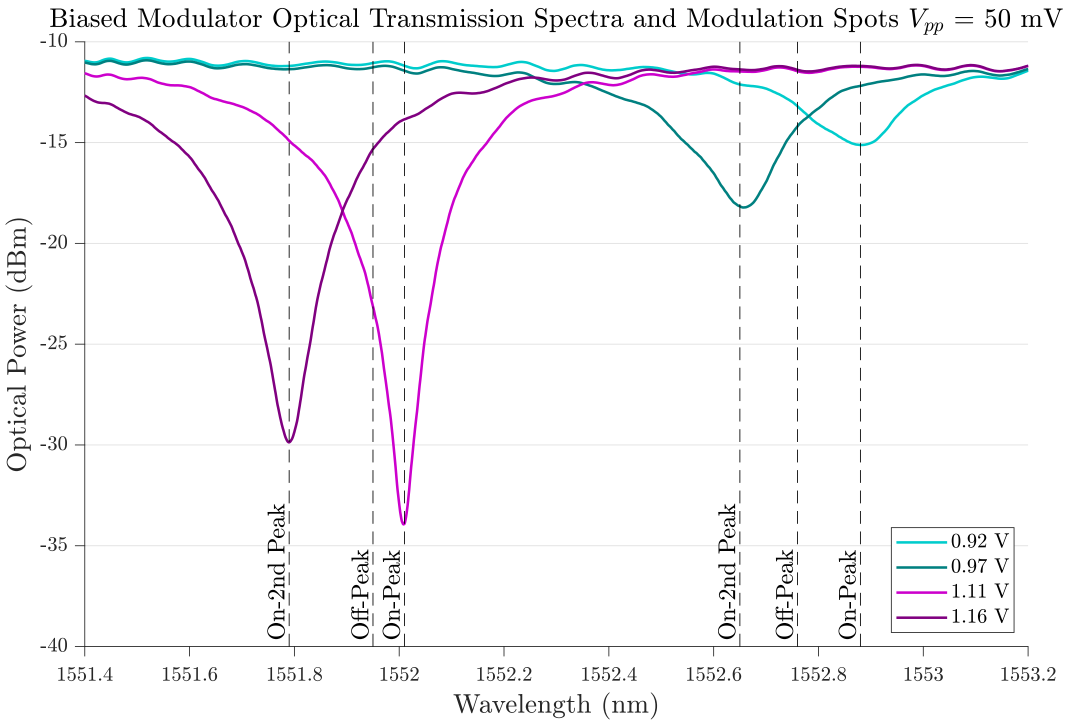

FIGURE 4.10: Modulation transmission spectra wavelength placements.

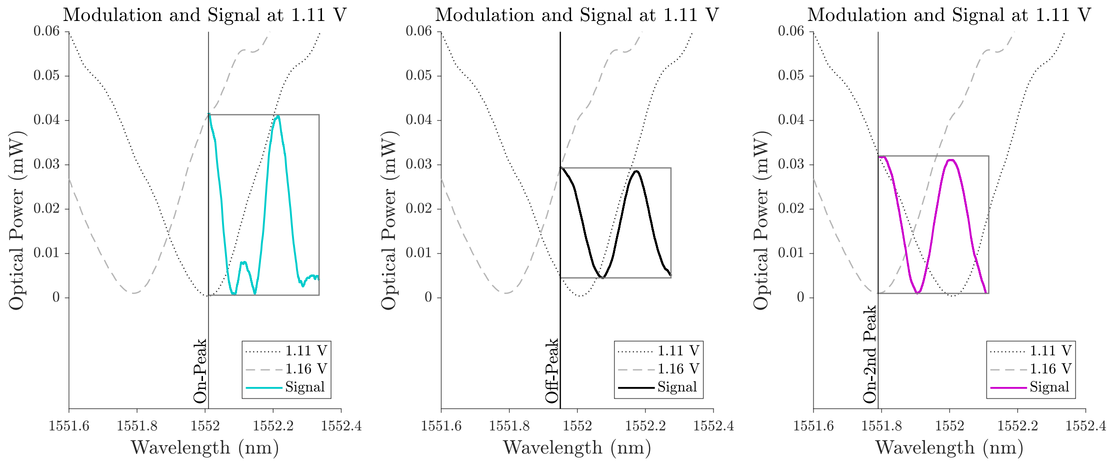

(A) On-Peak (B) Off-Peak (C) On-2nd Peak

FIGURE 4.11: Modulation and resulting output at three modulation spots.

For reference, Figure 4.10 shows different positions at which the signal was modulated with two forward biases, 0.92 V and 1.11 V. The modulation V_{pp} was 50 mV for forward biased measurements, and 1 V for reverse bias, both of which were done by using an external wave function generator (50 mV was the smallest peak-to-peak voltage possible with the function generator used). As seen, measurements were made on-peak, at the resonance point of the selected bias, off-peak, on the blue-side of the selected bias, and on-2nd peak, the resonance point of the bias plus the modulation amplitude. With the transfer functions being known, a better understanding of the movement of the transfer function can be obtained, and how any non-linearities might manifest. The input into the ESA was split and fed into an oscilloscope. Graphs in Figure 4.11 demonstrate the oscilloscope output at 1.11 V forward bias with a 50 mV V_{pp} modulation. These figures give a view of the output as modulation happens, and are plotted in linear optical power (mW) rather than logarithmic optical power (dBm), which makes it more intuitive to understand how the shifts form the output signal. The oscilloscope data is smoothed for simplicity. The raw oscilloscope data can be seen in Figure 4.12, signals DC shifted for easier comparison. Figure 4.12a shows the wavelength placement clearly affecting the output of the signal in the time domain. The on-peak function has severe distortion, does not manifest a sinusoid, and it can be clearly seen that several different frequencies are present. The off-peak measurement remedies this to a degree, and the 2nd-peak measurement almost eliminates it, although the signal does not perfectly resemble a sinusoid. A similar story can be seen in Figure 4.12b, although the optimum measurement at the 2nd-peak seems to look more like a sinusoid. It is clear that the modulation amplitude should run negative from the modulation bias, not positive. The function generator was set up to have a V_{pp} of 50 mV, and an offset of 25 mV. Instead, an offset of -25 mV should have been used for a more linear output. A measurement of reverse bias can be seen in Figure 4.12c, but comparing it with background noise demonstrates that almost no power made it into the oscilloscope. Subtracting the background signal from the others did not yield any useful data.

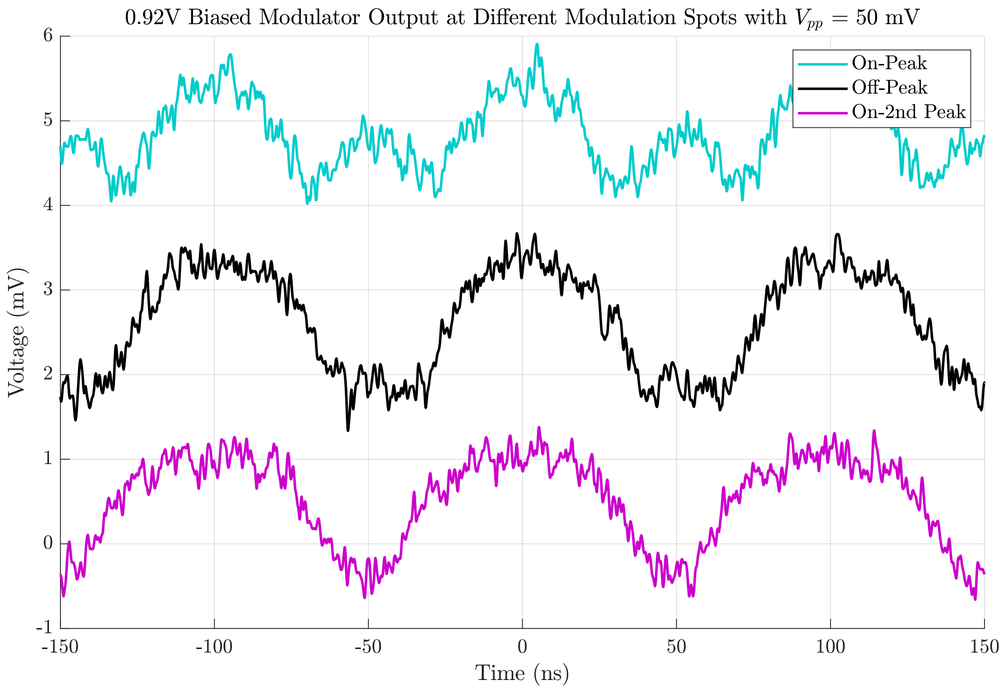

(A) 0.92 forward bias with $V_{pp} = 50$ mV

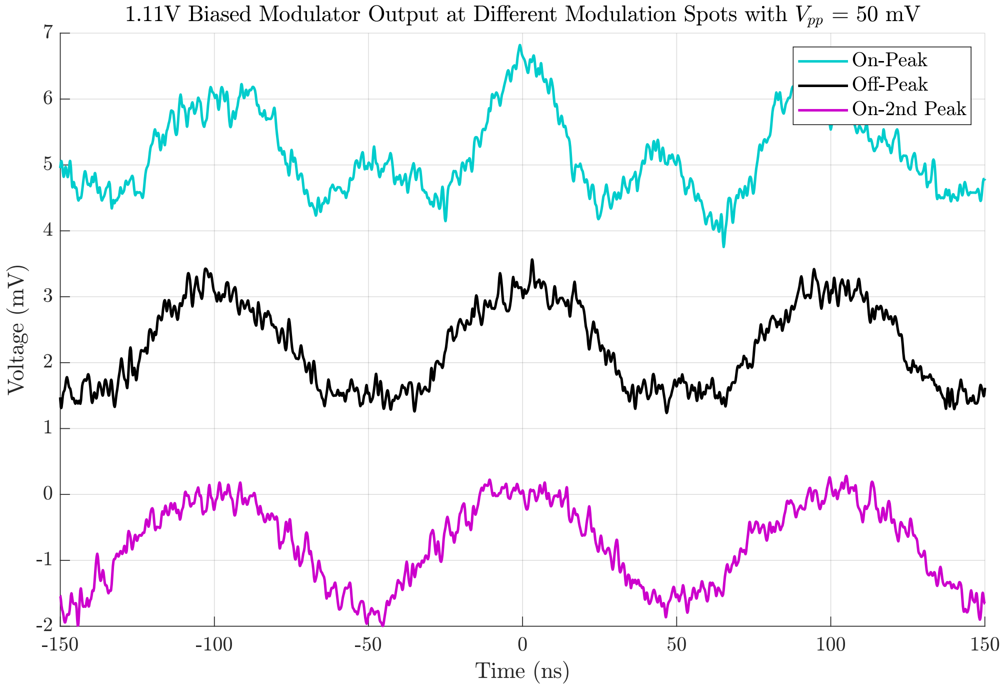

(B) 1.11V forward bias with $V_{pp} = 50\,\text{mV}$

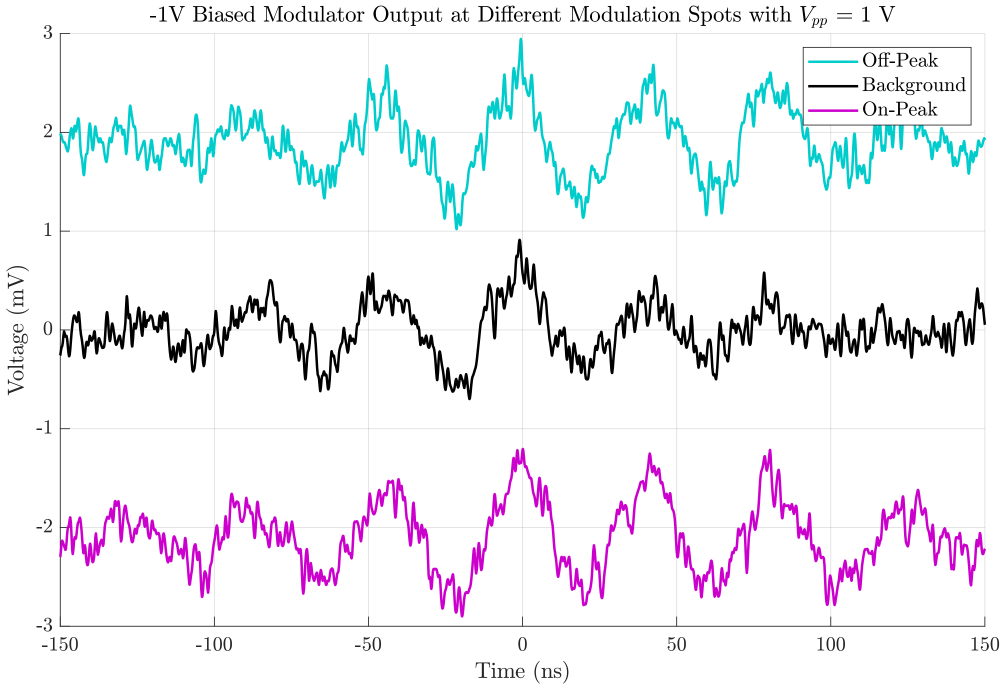

(C) 1V reverse bias with $V_{pp} = 1\,\text{V}$

FIGURE 4.12: Oscilloscope measurements of output of modulator.

The output from the ring modulator was seen in the time domain in Figure 4.12, but was also fed into the ESA for frequency domain measurements. Figures 4.13 show the ESA output from which measurements were made. In this case, the output at 1.11 V bias is shown for different wavelengths. Table 4.2 takes this information and shows 10, 20, 30 and 40 MHz frequency responses from the modulator outputs, as well as bias, amplitude, and wavelength used for modulation. Any "—" characters indicate the power was not visible over the noise floor. If an output only contains the input frequency of 10 MHz, it means little to no distortion was produced. In contrast, power seen at harmonics of 10 MHz, is due to the non-linearity of the modulation and transfer function. As seen, reverse bias operation is very linear, but very low modulation depth was achieved, and therefore the output power was very low. At forward bias, the measurements clearly demonstrate relatively strong powers at harmonics of 10 MHz. As the modulation wavelength is blue-shifted, the measurements become more linear. Furthermore, 1.11 V, the critically-coupled bias, produces the most linear output and best modulation depth. As can be seen in Figure 4.12b, the signal is similar to that of a sinusoid, but is spoiled at the trough, due to that portion of the signal being modulated at the peak of the resonance, where the transfer function is not linear. An off-peak measurement is ideal, but it should be driven by a negative modulation amplitude (as stated earlier). Furthermore, the modulation V_{pp} should be smaller than 50 mV as this value is too large for such

Bias (V)	V_{pp} (V)	Wavelength Placement	10 MHz (dBm)	20 MHz (dBm)	30 MHz (dBm)	40 MHz (dBm)
-1	1	On-Peak	-88	—	—	—
-1	1	Off-Peak	-97	—	—	—
0.92	0.05	On-Peak	-61	-59	-70	-75
0.92	0.05	Off-Peak	-51	-75	-71	-77
0.92	0.05	On-2nd Peak	-53	-64	-80	—
1.11	0.05	On-Peak	-54	-61	-69	-85
1.11	0.05	Off-Peak	-51	-69	-70	—
1.11	0.05	On-2nd Peak	-51	-70	—	—

Table 4.2: 10 MHz modulation response probed at different frequencies.

a large wavelength shift. Looking at Figure 4.10, modulation should have happened slightly to the right of the On-Peak measurement on 1.11 V bias where the signal is most linear, likely with a negative 10 mV V_{pp} to bring it down to 1 V during modulation. This would yield the most linear signal with highest modulation depth possible. Solving the problem of linearity is not commonly discussed in literature, but it is common to modulate with a small V_{pp} of 50 mV in forward bias operation [70].

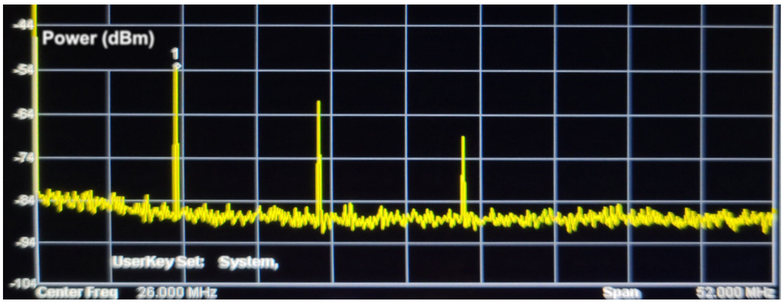

(A) On-Peak

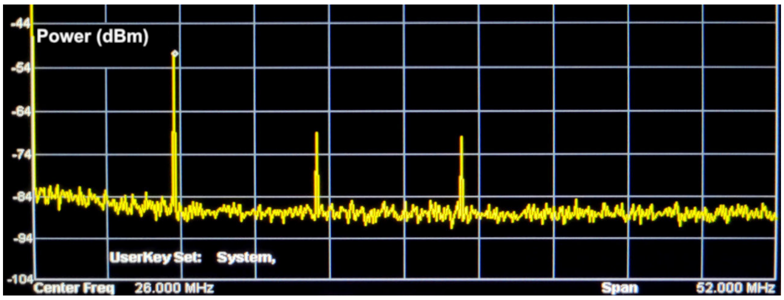

(B) Off-Peak

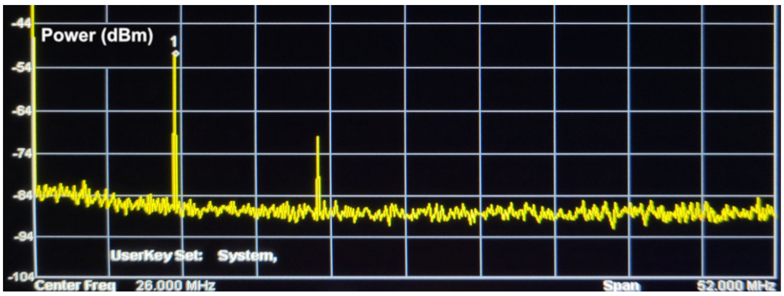

(C) On-2nd Peak

FIGURE 4.13: ESA graphs at 1.11 V bias.

4.3 True Time Delay Device

True time delay provides a method to enable an OBFN [44]. The delay in signals reaching different antennas make phased-arrays possible, as the radial or spherical waves from each add up to form a resulting plane wave, similar to point sources adding up in Hyugens principle. A phased-array is illustrated in Figure 4.1. The true time delay (usually in the range of picoseconds), adds a phase to a signal at each branch of an OBFN (each antenna output), a measurement that can be more easily described in a transfer function of an optical component [45].

A few optical components are able to add a phase shift to light. Simply increasing the path length of the light, by using a spiral for example (for highest density), can achieve this [84]. But custom delays prove to be more useful in an OBFN, at least near the end of branching, where fine tuning of the delay can steer the output. This is where an ORR can be of use [54], as they use a small footprint, and are able to be continuously tuned. The light is trapped in the ring for a certain path-length amount of time as energy is stored within the cavity [17]. As such, a delay is formed by the ORR which is modulated by the coupling into and out of the ring. The tuning of such come from two micro-heaters. This process uses the thermo-optic effect to change the refractive index (effective index) of the silicon waveguide [85], which in-turn modifies the effective path length of a waveguide by a certain amount. Having two heaters, one placed on a MZ area of the coupler (MZ heater), and another placed on the ring itself (phase heater), allows for fine control of the coupling ratio and path length respectively [86].

4.3.1 Design

The delay ring structure was based on other designs in our research group and those found in the research literature [67]. The design can be seen in Figure 4.14. Taking the ring itself (racetrack length, ring radius, MZ length), one can find the overall round-trip length, and therefore the round-trip time τ_r for light. From Equation 2.14, reproduced here [54]:

$$\tau_g(f) = \frac{\kappa\tau_r}{2 - \kappa - 2\sqrt{1-\kappa}\cos(2\pi f \tau_r + \phi)}$$

it can be seen that the group time delay τ_g is dependent on certain variables, which are mostly set by the existing ring design. Seeing that the power coupling ratio κ is a large determinant of time delay, this parameter is the one that is modified to facilitate tuning of the time delay. There are several physical attributes of the ring that change the power coupling, including the coupler length, gap, and MZ heater dimensions. The MZ heater causes a difference in power at the second coupler, and can in turn modulate the coupling ratio.

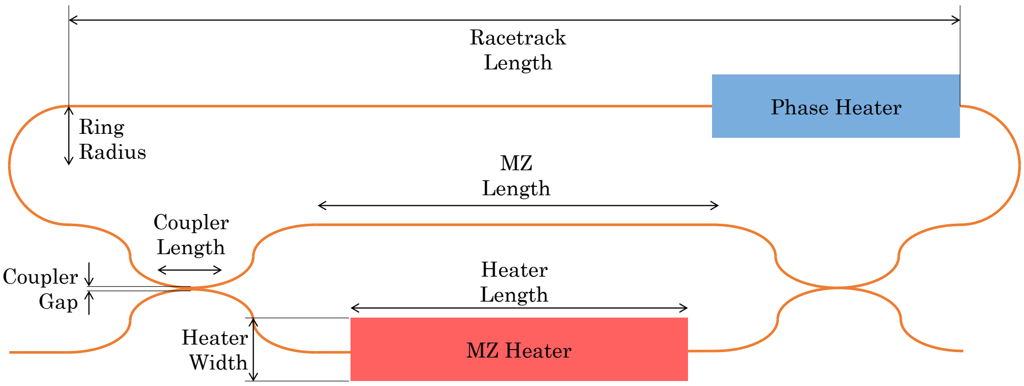

FIGURE 4.14: Delay ring schematic showing various variables.

The objective was to design a delay ring capable of 30-80 ps delay. This range is of interest for OBFNs, as it allows for certain common angles of transmission from a phased-array [86]. These delays are measurable by the existing setup using the VNA, described in Section 3. To achieve a delay of that quantity, a contour plot of the group delay time τ_g was created and shown in Figure 4.15, with wavelength λ (frequency converted to wavelength) and power coupling κ as variables. The round-trip time is kept constant as the design of the ring itself is not modified, and phase shift was fixed at 0. As expected with any ORR, there are resonant wavelengths at which group delay approaches infinity due to light energy being completely confined or trapped in the ring. That being said, this model does not account for loss in the system, so this infinite group delay cannot be reached in reality, as this would mean an infinite Q factor, which is physically impossible. The contour plot shows maximum delay between 0 and 10% power coupling. To better understand the behaviour, a 2D plot can be made at one of the resonances of the graph, at constant wavelength, to see what power coupling ratio is required for a delay of 30-80 ps.

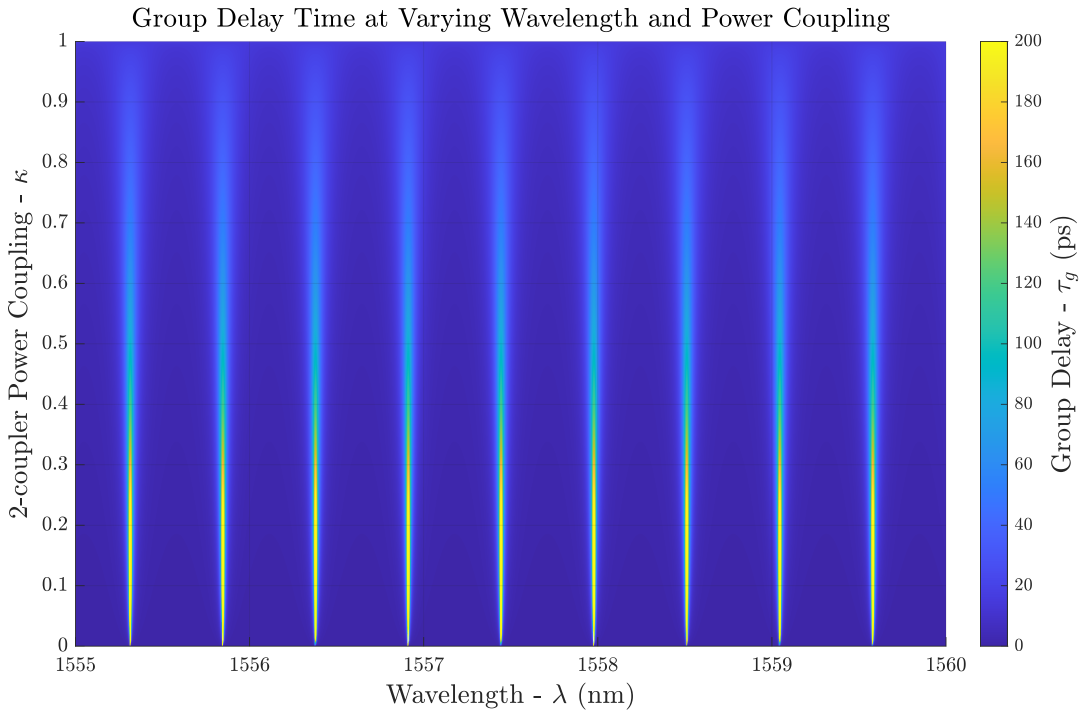

FIGURE 4.15: Group delay time versus power coupling and wavelength.

Figure 4.16 shows the delay profile at a resonant wavelength (at which the delay ring would operate). This graph is simply a vertical cross-section of the contour plot shown in Figure 4.15. It can be seen that to obtain a delay of 30 ps, a power coupling of 0.66 would be required, and for a group delay of 80 ps, a power coupling of 0.33 would be required. From this, the coupling gap and coupling length of the ORR can be found, trying to somewhat match the coupling range required, while ensuring the MZ structure can change the coupling sufficiently to shift between these two values.

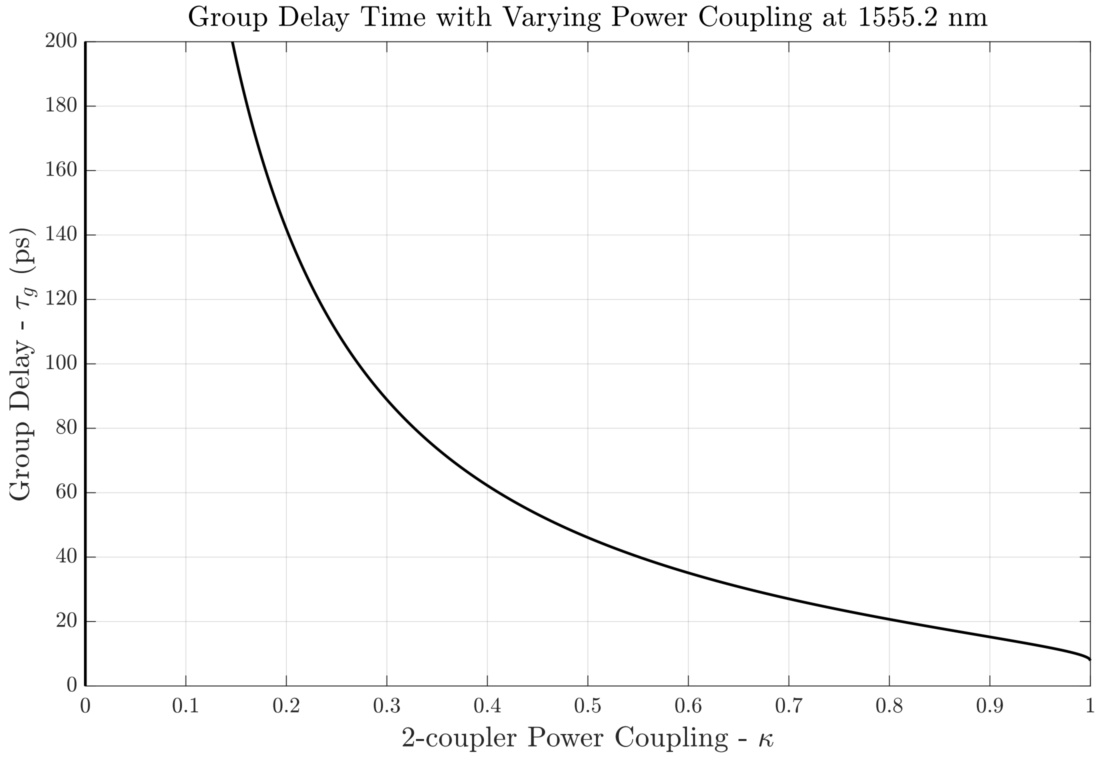

FIGURE 4.16: Group delay time versus power coupling at constant wavelength.

Firstly, the effect of the coupler gap was studied. To do this, a finite-difference time-domain (FDTD) simulation was done (Lumerical FDTD [87]) to determine the exact coupler configuration used, with the same s-bends seen in Figure 4.14. Figure 4.17 demonstrates the single coupler behaviour of strip and rib waveguides, at varying coupling gaps (distances) in nanometers, as well as at different coupling lengths described in Figure 4.14. The strip waveguide leads to less coupling when compared to the same parameters in a rib waveguide pair. It can also be seen that for the rib waveguide, at long coupling lengths such as 10 µm to 20 µm, the coupling does increase before it ultimately falls with coupling distance. This odd trend is due to the points at which the simulation was done, below the Nyquist frequency limit for the data, producing what is known as aliasing in the measurement. In reality at longer lengths, the power coupling is allowed to go from 0% to 100% power coupling, and then back down as many times as the length permits, sinusoidally. From this graph, a 200 nm gap was chosen, as it is accessible for fabrication, while allowing for a reasonable coupling length.

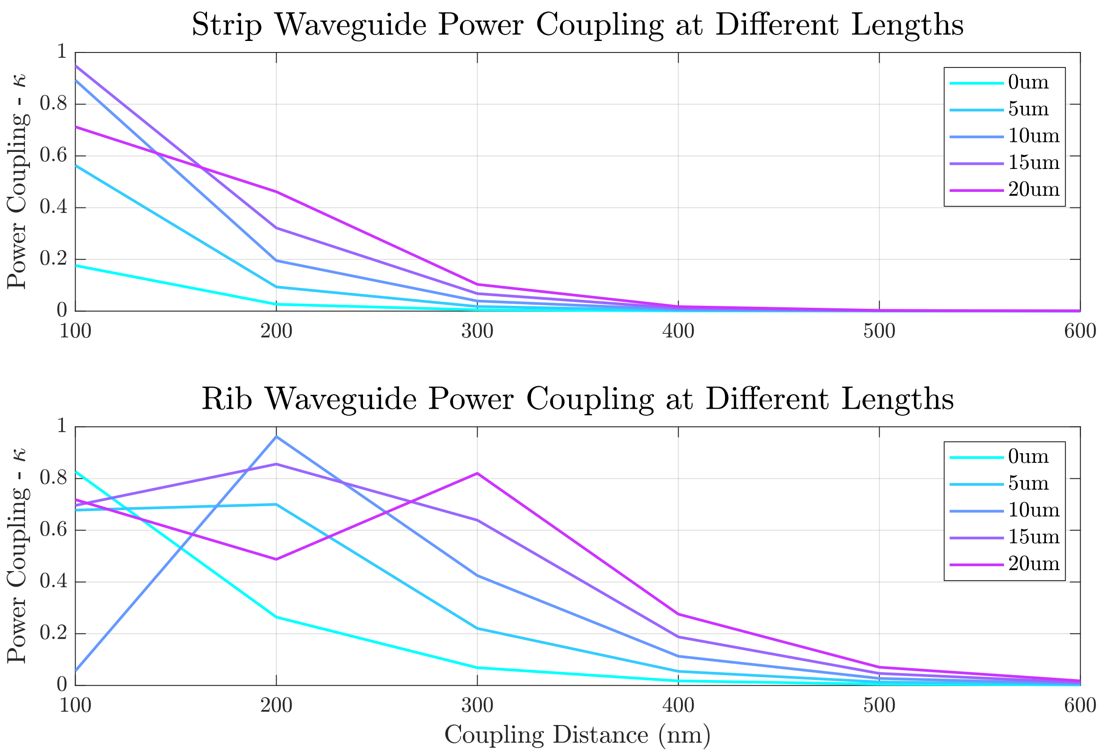

FIGURE 4.17: Strip and rib coupling versus waveguide gap and length.

Figures 4.18 demonstrate the power coupling after one and two couplers with a 200 nm gap, as a function of coupler length. These results were also simulated via FDTD, it can be seen that the results match those of the 200 nm gap in Figure 4.17. It can be clearly seen that two couplers will always start out with higher coupling, as there is more of a chance for coupling to occur when two couplers are involved. Nevertheless, coupling does reach a maximum, and then drops after reaching this maximum, which can be seen close to a power coupling of 1. The power coupling does not reach 1 in this instance as

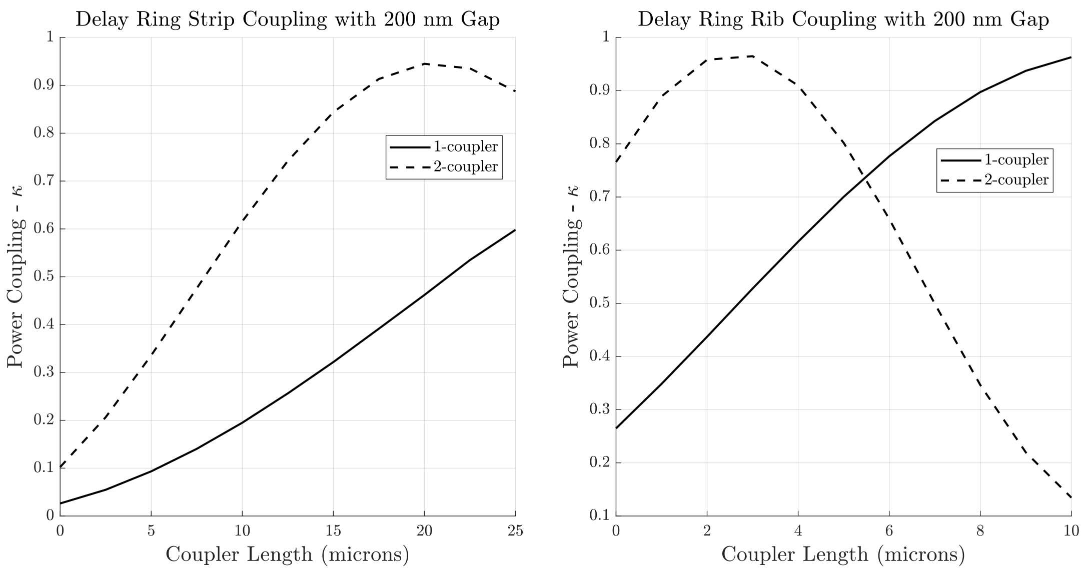

(A) Strip coupling

(B) Rib coupling

FIGURE 4.18: 1 and 2-coupler power coupling versus coupler length.

this simulation is not using ideal waveguides, coupling loss is happening as well. Looking at each graph separately, Figure 4.18a shows the strip waveguide behaviour, it is plotted to 25 µm in length as it takes a long distance to obtain higher levels of coupling, for the same reasons indicated previously. Rib waveguides on the other hand, shown in Figure 4.18b, demonstrate much higher coupling ratios. This is why the graph is plotted to 10 µm. Rib waveguides were ultimately chosen for the design of the delay rings, as the coupling regions could be made shorter, and therefore in a smaller footprint of the PIC. Although rib waveguides were chosen, there are some foundries that can only fabricate strip waveguides, as a slab region is not supported, in which case a strip coupler would suffice. Because the rib waveguide was chosen, it was possible to make a choice in coupler length. 5 µm-long couplers were chosen, as the power coupling after two couplers was 0.8. This value can be tuned.

The most important part of design of the delay rings is that the power coupling ratio could be tuned enough to achieve the required group delay time. The coupling

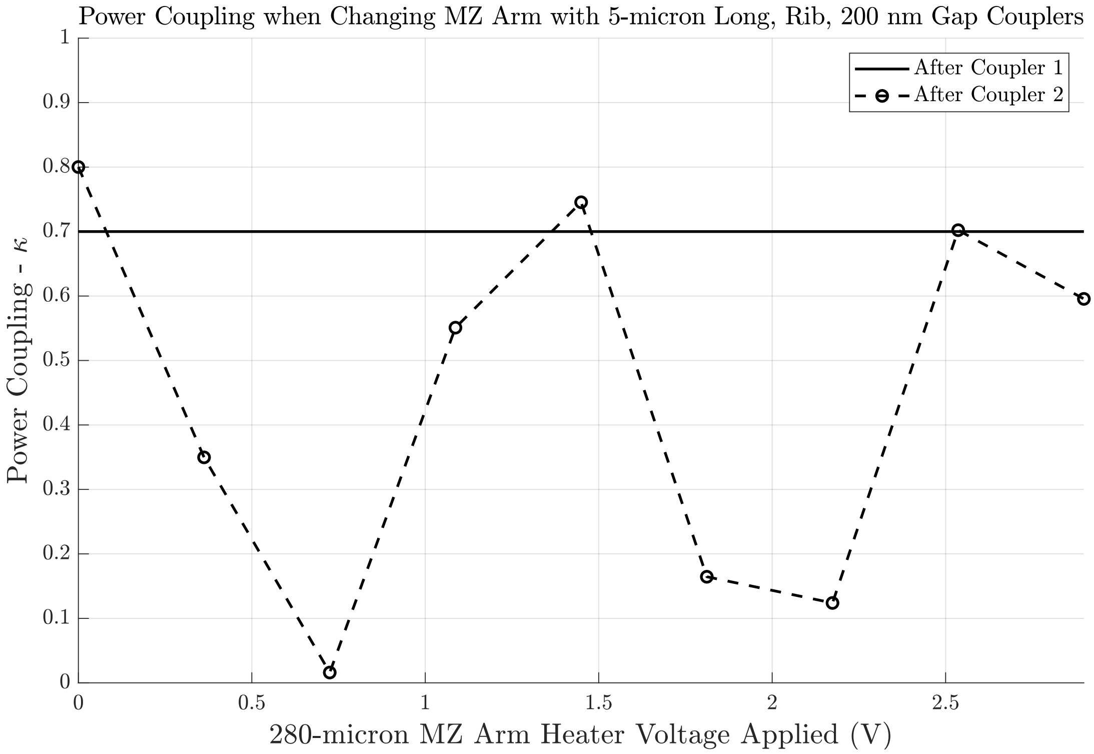

FIGURE 4.19: Power coupling versus voltage applied to MZ.

ratio is tuned using the MZ heaters. The specifications of the Advanced Micro Foundry (AMF) TiN heaters are accessible (but not shared here due to confidentiality). Using the heater resistance and π-phase shift power, one can find what refractive index change is necessary for such a π-shift. From this, knowing the resistance and power, an applied bias can be calculated. Therefore, the circuit was simulated, again, using FDTD, but changing the refractive index of the waveguide area underneath the MZ heater. The simulation yielded new power coupling ratios, and the refractive index changes were simply converted to applied voltages, whose graph is shown in Figure 4.19. It can be seen in this graph (coinciding at 0 V applied with the 5-micron value in Figure 4.18b), that the 0.8 coupling ratio decreases with voltage applied, and then goes up, following a sinusoidal pattern. Even with the few points simulated, it was already clear that the power coupling could easily span the range between 0.66 and 0.33 power by applying less than 0.5 volts into the MZ heater.

4.3.2 Experimental Performance

The delay ring was characterized using two methods. One was the optical method, which looks at the optical transfer function of the delay ring. The other method looks at the delay it produces, which is found by modulating a signal from the VNA, into a photodetector which feeds back into the VNA.

The optical transfer of the delay ring varied greatly with applied bias on the MZ heater. Figure 4.20 demonstrates the measurements made using the tunable laser. At 0 V bias applied to the MZ heater, it can be seen that an ER of about 0.5 dB exists, which is small and easily confused with the background noise. The ring is clearly not in its critical coupling state. Reaching 2.8 V (30 mW), the ER increased to 1.25 dB, at 3.1 V (36 mW) to 2.5 dB. Critical coupling was achieved at 3.33 V (42 mW) as a higher bias led to a decrease in ER. Similarly, prior work in literature demonstrates that a power of 45 mW applied to the MZ heater achieves a full π cycle of coupling [67], comparable to what is depicted in Figure 4.19. At critical coupling the extinction ratio was about 5 dB. The free spectral range (FSR) is inversely proportional to optical path length and is therefore a function of group delay time. The FSR is given by Equation 2.11, reproduced here:

$$\mathrm{FSR} = \frac{\lambda^2}{n_g \Delta L}$$

FSR values in prior work with similar ORR structures are of 0.63 nm, while structures measured in this work are 0.58 nm. This similarity demonstrates the optical path length is similar to that in literature. Solely using Equation 2.14 shown in Figure 4.15, the FSR was found to be about 0.55 nm, which deviates by a small amount from experimental results. This is due to imperfect calculation of the round-trip time τ_r, likely due to differences in group indices from literature [17] and real group index in the measured chip.

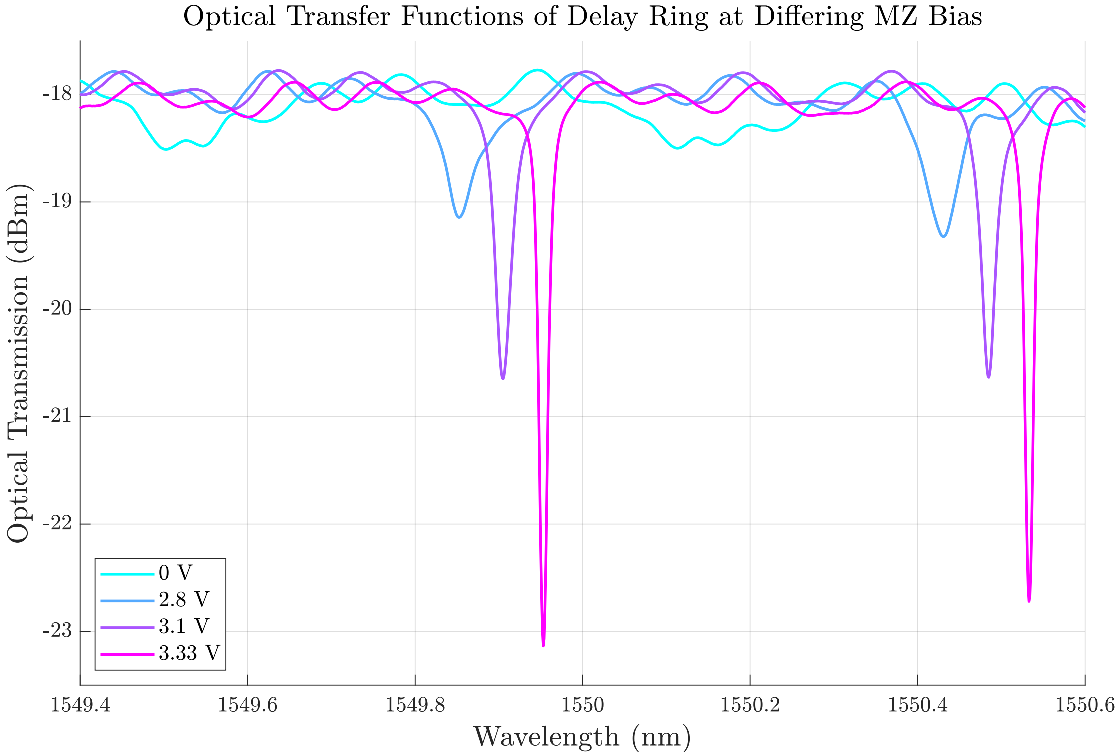

FIGURE 4.20: Optical transfer of delay ring at different MZ biases.

The 1.25 dB, 2.5 dB, and 5 dB ER transfer functions were used for determining delay created by the delay ring. The delay is a function of RF phase response, observed by the VNA. This phase response can be seen in Figure 4.21. The larger the extinction ratio in Figure 4.20, the larger the phase response given by the ring. This makes physical sense, as more of the light is trapped within the optical cavity, therefore it spends more time inside it, and it takes longer to be released. The group delay in picoseconds can be obtained from the RF phase response in degrees using [67]:

$$\tau(\lambda) = \frac{\phi_{21}^{T}(\lambda)}{\omega_{RF}} \tag{4.1}$$

a simplification of Equation 2.14 given before that only works on linear systems. Here, $\phi_{21}^{T}(\lambda)$ is the transmitted RF phase shift as a function of wavelength, measured by a VNA. Meanwhile, ω_{RF} is the input RF angular frequency used for the modulation of the signal. In this case, the modulation frequency used was 200 MHz. This frequency is set for the coarseness or fineness of a needed measurement, a large delay (nanosecond range) measurement could use a low frequency, a small delay would necessitate a high frequency [67]. The frequency is often limited by the instrumentation used, therefore measurements of a few picoseconds of delay are out-of-reach with the measurement method employing the VNA used.

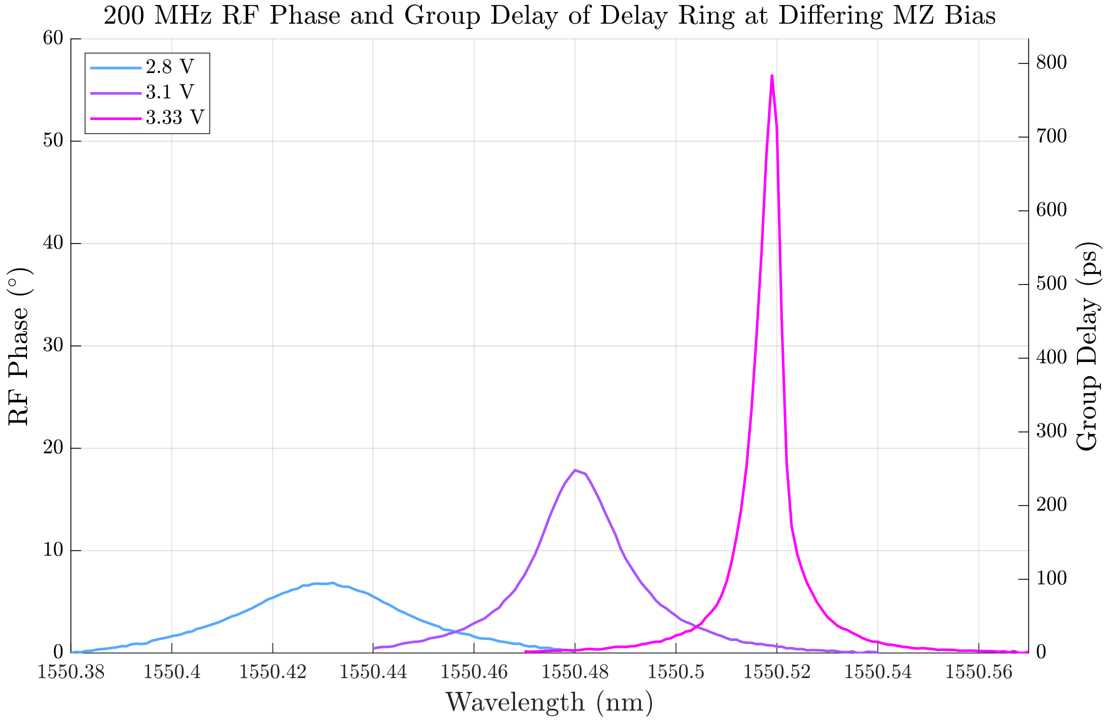

FIGURE 4.21: RF Phase and delay at delay ring at different MZ biases.

Bias (V)	Power (mW)	ER (dB)	Phase (°)	Delay (ps)
2.80	30	1.25	6.8	94
3.10	36	2.5	17.9	248
3.33	42	5	56.4	784

TABLE 4.3: Group delay times produced by delay ring.

RF phase shift in degrees is shown in Figure 4.21, converted to group delay in second y-axis. Table 4.3 summarizes the data shown in Figure 4.21. As seen, a delay of up to 784 ps was achieved at critical coupling of the ring, with 5 dB extinction ratio. This delay

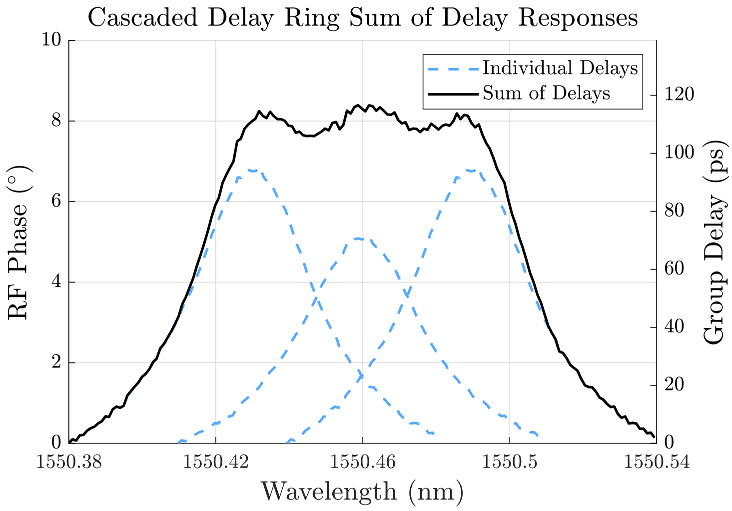

FIGURE 4.22: Cascaded delay rings and their sum.

is high and largely exceeds the discussed 30-80 ps delay. This delay still has its place in OBFNs, but consumes power, so other passive components can produce this delay passively, such as spirals [84]. When leaving critical coupling though, the delay quickly decreases, to the point of 94 ps at 1.25 dB ER, which is the closest value measured to the range required. This value is similar to those reported in literature [67]. From this, it can be deduced that the desired delay range can be achieved by simply lowering the heater bias applied, and therefore the extinction ratio. One concern that comes with this is that the Q factor decreases with decreasing ER, and therefore, a larger shift in wavelength would be required to trim delay, and subsequently steer the signal from the phased-array. This approach does come with the benefit of additional or finer granularity and control of the delay applied. Another approach is to set the working wavelength shifted from the resonance peak, and obtain the wanted delay, simply biasing the phase heater rather than the MZ heater to change the resonance (and therefore delay). Figure 4.21 demonstrates this is possible, the peak delay is at 1550.43 nm, but a delay of 77 ps can be achieved by shifting the working wavelength by 0.1 nm in either direction. Relying on an off-resonance wavelength may not be possible in certain situations such as cascaded ring operation as seen in Figure 4.22, because the overlapping group delay functions would modify the resulting sum of functions [54]. The sum of delays function has a bandwidth of wavelengths that can be used for a certain delay, operating outside this bandwidth nulls the purpose of cascading. Such cascades are leveraged for situations where more wavelength bandwidth is required, and therefore more wavelengths can be utilized.

4.4 Summary

A modulation depth of 21 dB was obtained at 1.11 V from a micro-ring modulator which was simulated and tested for forward bias operation. The forward bias operation limited the 3 dB bandwidth of the modulator to 500 MHz, but with a driving voltage amplitude of 50 mV, it proved to be quite linear, with a second harmonic power 19 dB lower than the first. The true time delay ORR yielded a 784 ps delay at 3.33 V heater MZ bias applied, but can be tuned to lower voltages to produce a lower required delay.

Chapter 5

Photonic Packaging

5.1 Introduction

Photonic packaging is a complex subject. Multiple approaches exist, many of which were discussed in Chapter 1. Packaging is often neglected in the academic sector due to cost. Packaging tools are very expensive, and contract manufacturers that offer packaging do not see value in small volume development [88].

While aligning fibers to photonic integrated circuits (PICs) these days is not too challenging, permanent attach to a chip is a much more complex task [89]. Requiring ultraviolet (UV) curable epoxy that sticks a fiber to a chip.

5.2 Design Requirements of This Work

Our goal was to design a photonic chip packaging solution for use by research institutions and those wishing to package low-volumes. To start, a list of requirements (specifications) was created. Most importantly, the packaging solution needed to maintain a low cost. It would have been a very simple solution to obtain an expensive nanolithography system to create photonic wire-bonds such as Vanguard Automation's solution [90], but this is not accessible to most. It was assumed that modern photonic labs included some expensive equipment as standard, such as a laser, detector, x-y-z stages. We also sought flexibility in a process that can incorporate any chip.

Less crucial aspects were performance and complexity. Firstly, performance did not need to rival state-of-the-art processes, as high-performance alternatives exist, at a high price. Process complexity could be relatively high, as this process did not need to reach mass-scale production. This means that packaging could be performed by individuals rather than automated solutions.

The design had to enable edge coupling from two sides of a chip. Inspiration could be drawn from existing optical measuring setups already used in our lab, seen in Figure 5.1. As seen, fibers come from the sides, to couple light into the chip laterally. Furthermore, a microscope can be used to enable the alignment process. The fibers needed to be able to be attached to the chip without shifting of the fiber tip. Furthermore, if an adhesive, usually in liquid form such as UV epoxy, were to be used, the liquid would need to be pooled somewhere for curing and not leak out.

The principal roadblock with making a packaging solution for any possible chip is the custom nature of the solution. Packaging should be possible with any chip, of any size (x, y and z dimensions) and input and output do not need to be aligned (not in same lateral position, but only parallel). Because 3D printing has gained a large foothold in various fields in technology, approaches including the use of custom parts created with a 3D printer were explored. Finally, the solution should have also enabled the use of electrical interconnects, wire-bonding or electrical probing.

5.3 Design Iterations

There were multiple iterations to the design of our packaging solution. The design was iterated in order to make the solution as successful as possible. At first, a design for just

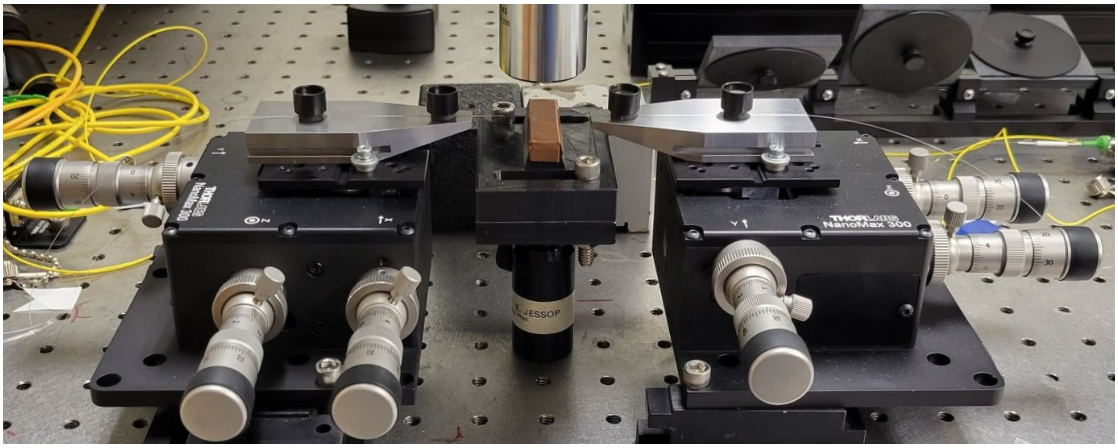

(A) Stages used, holding fibers, microscope

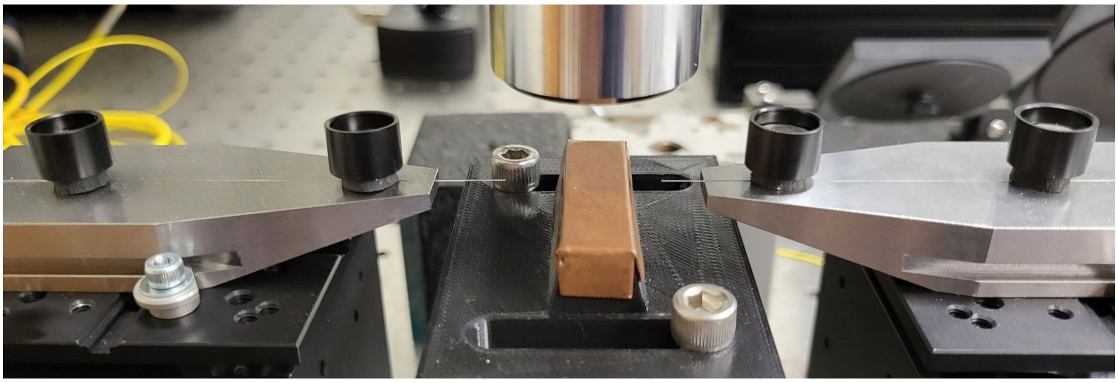

(B) Zoom-in of setup

FIGURE 5.1: Optical setup using tapered fibers on either end.

one input was devised. Figure 5.2 shows the setup, where a 3D printed platform in red held the silicon chip in place. A V-groove chip would be able to encapsulate the fiber in place. The V-groove chip is a silicon piece that has a long groove along the middle. This groove can then house the fiber core and cladding. This can easily be made with a lithographic pattern and an anisotropic KOH etch, or are also standard parts that can be purchased [91]. The V-groove chip is a common theme in this chapter, along with the 3D printed component. The problem with this design was that the 3D printed part would require very high precision, as the fiber would need to be placed exactly where the silicon chip had its waveguide input. This sort of precision is not possible with consumer 3D printing. Furthermore, if one would want to align a custom area of the silicon chip, it would have been impossible without modifying the 3D printed base.

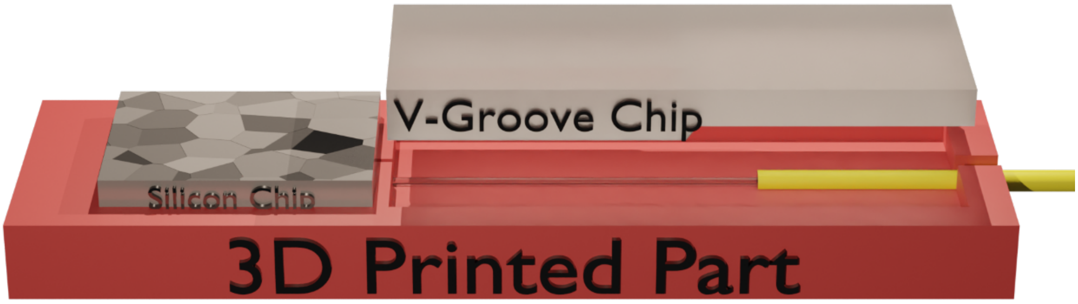

FIGURE 5.2: First iteration of the fiber-to-chip setup.

Because the 3D printer lacks the precision needed to place a fiber with a tolerance of within a micrometer, the design (shown in Figure 5.3) was later upgraded to allow for movement of the chip in the x, y and z directions. The y direction could move back and forth with the help of two "probes" in white, on either side, and the z direction could easily move up and down with one probe and the help of gravity. The only issue was with the x direction, where the chip could only be pushed forward, and not pulled backward. The other side of this setup had a V-groove assembly, that fit neatly into the 3D printed part. This assembly can also be purchased [91], it comes with the V-groove chip, the fiber (with connector on the other end), and a glass lid to ensure the fiber stays in place in the V-groove. More range of motion was possible with this approach, but alas, was not robust enough to work, as the x axis had only one direction of movement.

By simply sticking the silicon PIC to a probe underneath shown in Figure 5.4, one can get x, y and z motion in both directions. The only requirement was that there must be a larger opening underneath, through the 3D printed part. A problem with such a setup is that the probe would need to stay with the whole package, which is not an issue in itself, but there is no way to disconnect it from an external stage. This is where external interfacing started to become a challenge. Furthermore, any adhesive added would leak through the hole beneath.

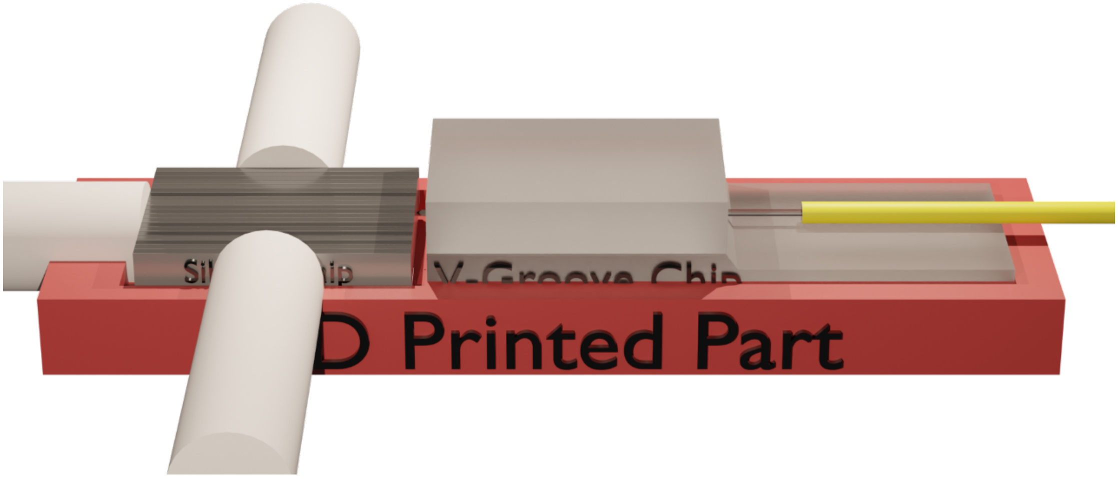

FIGURE 5.3: Second iteration of the fiber-to-chip setup.

FIGURE 5.4: Third iteration of the fiber-to-chip setup.

An intermediate iteration of the setup was to build everything in-house in the clean room. Figure 5.5 shows the idea, where a [100] silicon wafer (crystal orientation is key to V-groove creation) could be processed. Firstly, a hole larger than the PIC itself through the whole wafer would need to be made. Secondly, trenches of roughly 300 µm in depth could be made on either end for fiber jackets to fit, and V-groove sections connecting the trenches to the hole. This process could be done with a lithography tool, a deep reactive ion etcher (DRIE) and KOH. A lid could be placed on the fiber tip to keep it in place, as shown on the left on Figure 5.5. The silicon chip could be again moved by a probe, this time in yellow, such as in the previous approach in Figure 5.4. This approach was not pursued though, as it is quite complex, and the idea of making a system that is accessible to most, might not overlap well with facilities that have a clean room available to them, much less with a DRIE.

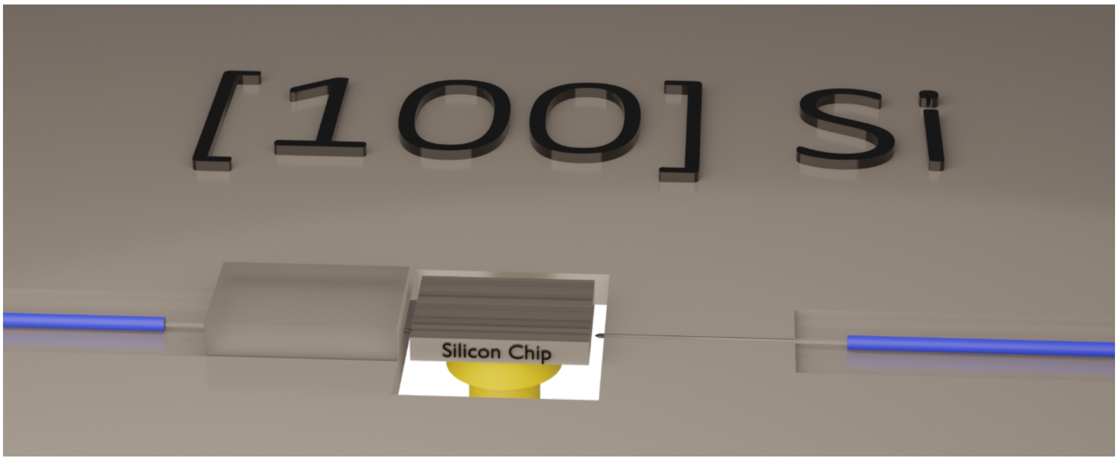

Figure 5.5: Spin-off of third iteration of the fiber-to-chip setup.

A common area where the aforementioned designs fell short was the ability to couple more than one fiber into the chip. Many PICs require inputs and outputs, especially in research and development phases. This led to the idea of moving the fibers themselves, and not the PIC. This more closely resembled the optical fiber measurement setup in Figure 5.1. A new design was constructed, shown in Figure 5.6, which has a similar approach to the third iteration, but the silicon chip is now static, with the fibers moving instead. The very useful part about V-grooves being in the design is that one can manipulate their tips rather than the fiber from far away, which means that if adhering the fibers, one has more control on the fiber tip and can keep it in place. There were issues that came from the probes attaching from below, which not only meant that the epoxy would leak through the hole underneath, but the probes would need to disconnect from the external stage without moving the fiber at all.

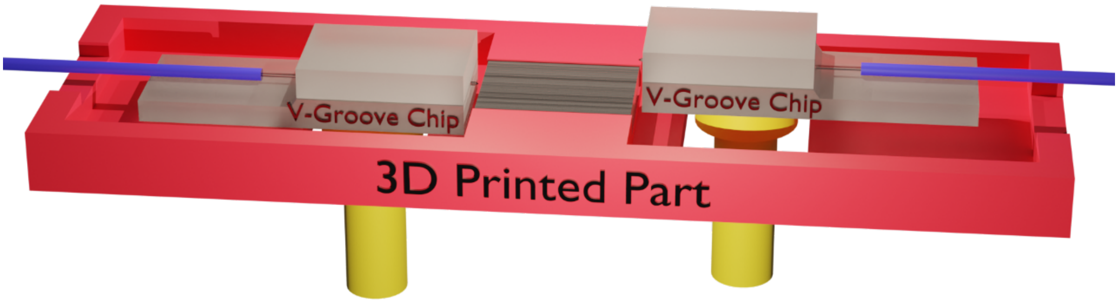

Figure 5.6: Fourth iteration of the fiber-to-chip setup.

The final iteration is shown in Figure 5.7. This design included the probes from the top rather than the bottom. This made the 3D printed part much simpler. To disconnect from the external stage from the probe, pick-and-place tools needed to be looked at. The pick-and-place tools themselves are often prohibitively expensive for many research institutions [92], therefore another alternative was required. It was found that vacuum tweezers could grab onto the V-groove assembly glass covers (as they are smooth) and move them. Furthermore, these vacuum tweezers could disconnect from the fiber tip easily by releasing the vacuum.

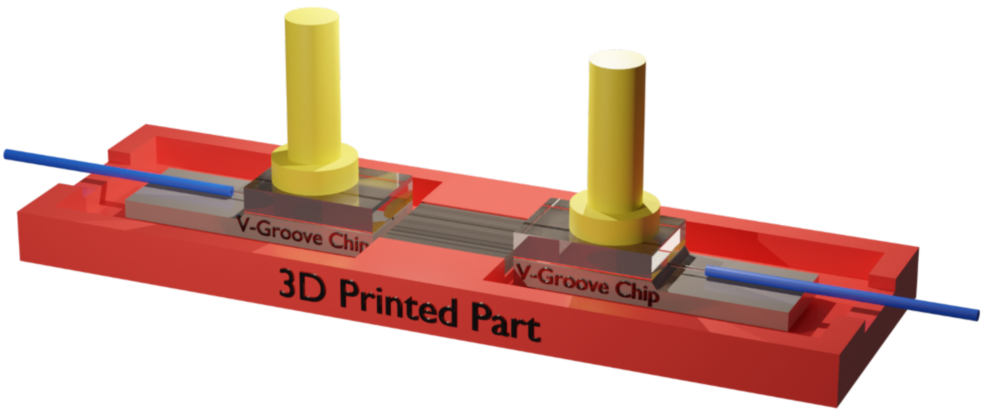

Figure 5.7: Fifth and last iteration of the fiber-to-chip setup.

5.4 Experimental Implementation

Figure 5.8 shows the physical implementation of the first setup. The first implementation used fiber-to-chip coupling, but there was only one optical-in port, and an electrical-out port. The PIC used was a photodetector. This made it simpler for the proof-of-concept. A Newport 460A-XYZ was used as an xyz-stage. This positioned a Virtual Industries TV-1000 vacuum tweezer, held by a custom-made 3D printed component. There were multiple 3D printed parts used, as seen, to lift the xyz-stage to a desired location, to hold the tweezer, to lift the PIC packaging stage and the packaging stage itself. All these parts took less than a day to print, were very inexpensive, and integrated well with the existing lab setup and optical table. On the other side, electrical direct current (DC) probes were positioned to connect to the chip. The V-groove assembly was used to couple into the chip, and finally, the microscope on top was used to make coupling possible (all parts needed to be brought up to enter the focal plane of the microscope).

To make for good adhesion, UV epoxy was used. The adhesion was done between silicon (the V-groove chip itself) and plastic (the packaging stage itself, made of polylactic acid (PLA)). Three different adhesives were tested, Norland Optical Adhesive (NOA) 61, 81 and 68 [93]. These are all UV curing epoxies, with different curing properties. Some were designed to cure quickly, some to bond to plastics better. It was found that NOA 61 was the most stable and best adhering out of the three, after testing of curing time at different UV light source distances and angles.

The biggest problem with coupling was visibility. Because the V-groove assembly has a glass lid on top of it, it has a refractive index different than that of air. This means that when using a microscope, one can be focused on the surface of the chip where the waveguide is, but the fiber inside the V-groove will not be in focus, as the light goes through another medium (the glass lid). This makes it very hard to visually check if the fiber is aligned in the y and z directions, as the whole fiber is out of focus and not visible.

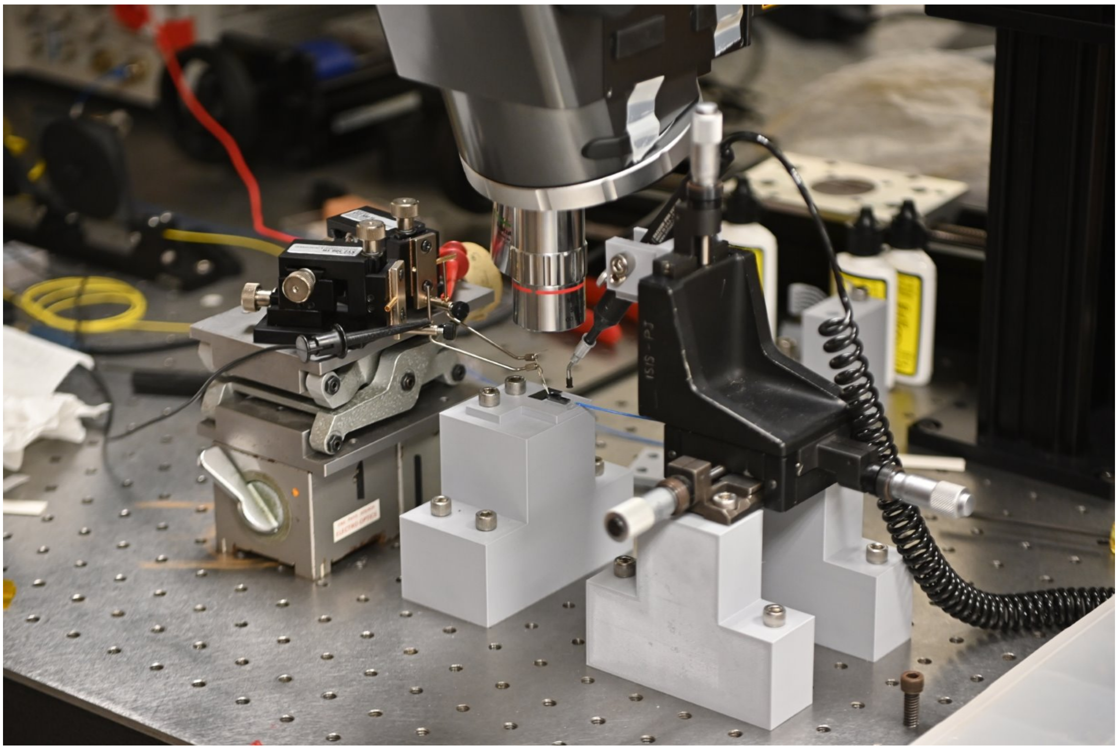

Figure 5.8: Implementation of fiber-to-chip setup.

Some issues arose because the PIC was mounted on carbon tape rather than being glued on the surface of the stage, which caused shifting and the PIC to become uncoupled when the DC probes would move or (dis)connect. Other issues that arose were that the fiber length would pull on the fiber tip and would rotate the V-groove around the vacuum tweezer, so the rubber vacuum tweezer tip being somewhat malleable was a problem. These issues were overcome. The PIC was glued with a fast-acting adhesive “super glue”, where only one drop is needed to stick and cures in seconds, which prevented any later movement and uncoupling. The fiber moving the whole V-groove assembly was first thought to require a higher-pressure vacuum, as well as stronger rubber tips, but to avoid their use, a guide was printed and attached to the vacuum tweezer holder itself. This made sure the fiber stayed in place relative to the tip as the whole stage moved. This solution can be seen in Figure 5.9a.

The actual process of applying the UV epoxy and curing was a challenge also. As seen in Figure 5.9b, epoxy would be put under the V-groove chip. Too little would not make contact with the V-groove, but too much would display the surface tension creeping upward shown in Figure 5.9b. This would ruin the coupling between chip and fiber. What was found to work best was to apply a small amount, and move the V-groove side-to-side (depth-wise in Figure 5.9b), and then cure. The curing process is non-trivial. As the vacuum tweezer tip has some lash-back, as it is made of rubber, the V-groove and glass lid would shift when the UV epoxy cured. A solution to this was to cure 15 seconds at a time, re-coupling in-between curing. After about ten cures (dependent on distance, angle, and amount of epoxy), the fiber would be at the best possible alignment and attached.

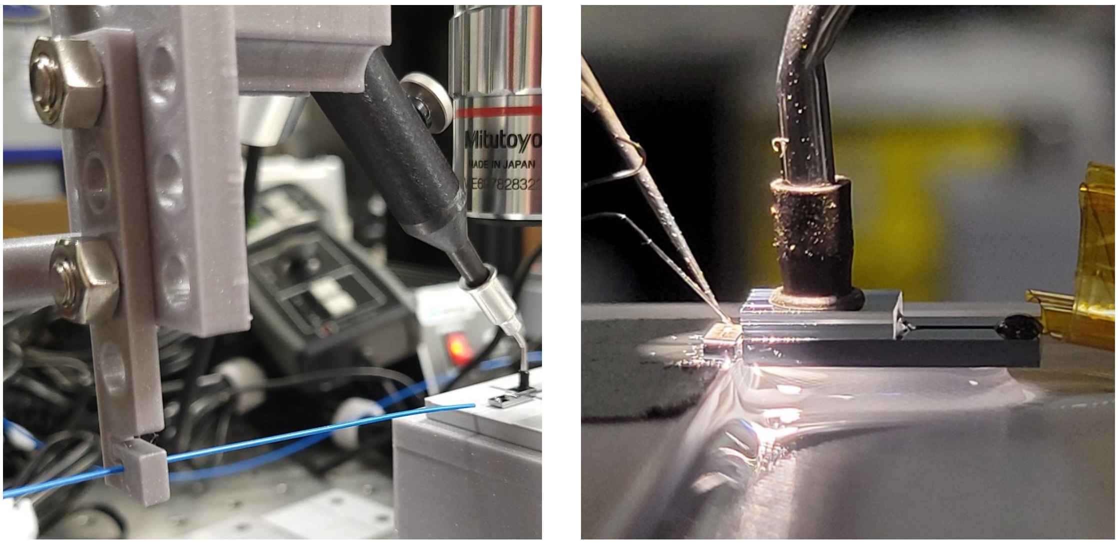

(A) Guide for fiber to move with stage

(B) Epoxy under V-groove

Figure 5.9: Solutions and roadblocks in the fiber-to-chip setup.

Another area of improvement was the xyz-stages, which, due to their age, were having issues with vibration and excessive movement when adjusting micrometers due to old springs. Newport 9064 stages were installed and used, and automated actuators (piezo) were opted for, the Newport 8302 actuators. These actuators have a good resolution due to their piezo nature, but allow for quicker manual coarse adjustment also. To control the actuators, controllers were needed to be procured, although these were strategically chosen as they have USB connection and libraries in order to automate processes in the future.

For optical-to-optical connections, the same general setup was followed, but instead of using DC probes, another fiber and stage is set on the other side, just like an optical measurement setup shown in Figure 5.1. If DC probes are still required, which they were at times, the probes can be mounted at the back, as shown in Figure 5.10.

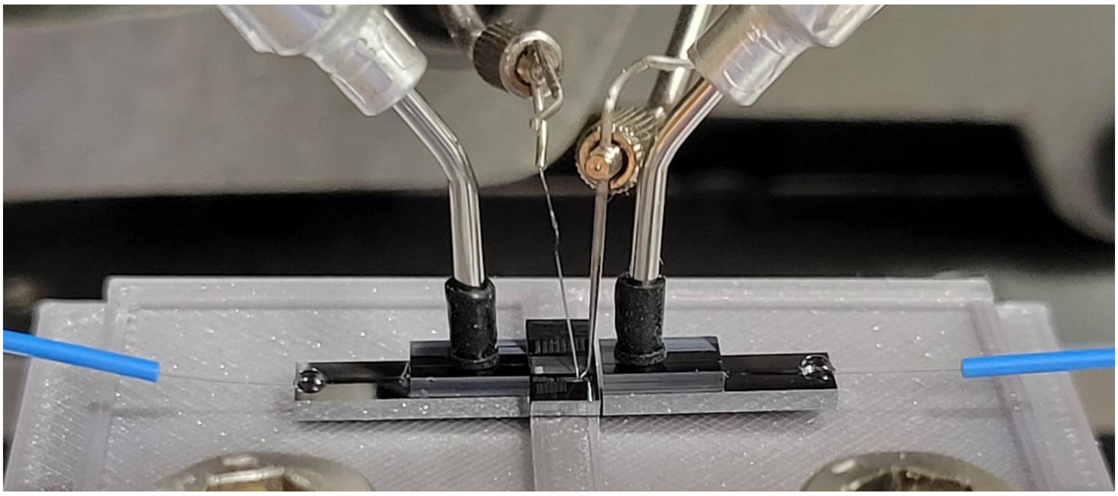

Figure 5.10: Two-optical connections and a DC connection.

5.5 Performance

The starting setup was one-optical input, going into a photodetector in the PIC, and DC probing on the other end, as shown in Figure 5.8. The packaging approach had multiple stages, for which the photocurrent through the detector was measured, for better understanding how the alignment changed throughout steps. The first measurement is often a direct tapered fiber into the chip, for characterization of the detector itself. Afterwards, the whole packaging stage is set up, and a free V-groove fiber is coupled with the waveguide (free as in no epoxy applied, but still held by the vacuum tweezer and controlled by the xyz-stage). A free fiber measurement shows the highest-possible coupling without the influence of epoxy. After the epoxy was applied, another measurement was taken. This measurement can show how the epoxy and its surface tension might force the V-groove surface downward, applying a force, as seen in Figure 5.9b. Once the epoxy is cured, another measurement is made. Many times, extra epoxy was applied at the back of the V-groove assembly and especially the fiber itself, to better secure them to the 3D printed package. Once these were done, the vacuum tweezer is removed, and another measurement made. At this point in time, the packaging is complete. Measurements were made 2 days later, and after moving the packaging and shaking it (to a moderate degree). The measurements made at each of these stages are shown in Figure 5.11.

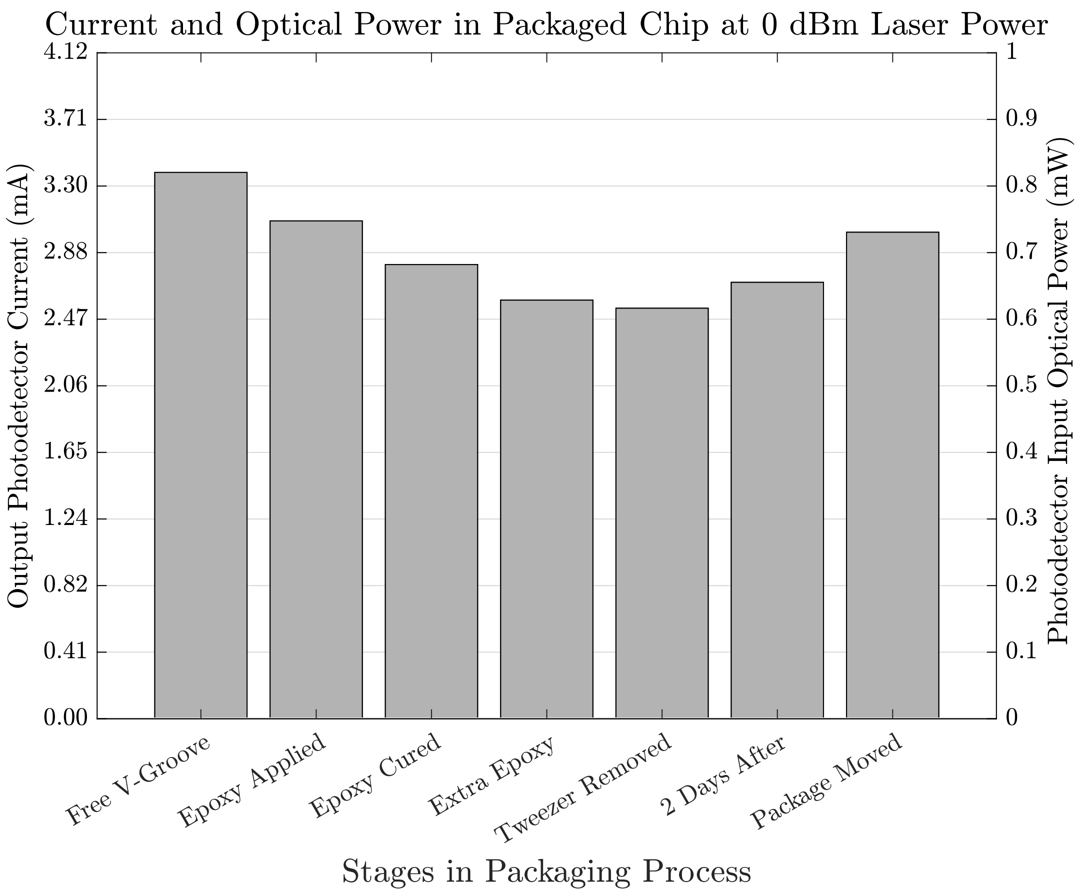

FIGURE 5.11: Packaged PIC current and power at different stages.

An interesting pattern emerges in Figure 5.11, but the photocurrents do not mean much in optical terms without extra information about the detector and system. What is needed is to know how much loss is incurred at each of these different stages. To do this, the responsivity of the photodetector used was found to be $4.12\,\mathrm{A\,W^{-1}}$, including gain, as the detector was an avalanche photodetector (APD). This responsivity was found by measuring the photocurrent. The the input power is not the output power of the laser, rather, the input into the detector. Therefore, more information was needed, the taper-to-taper fiber power, and power through a straight waveguide of the same chip (which includes propagation loss and coupling loss to the chip). With this, 0 dBm or 1 mW optical power from the laser translated to 0.587 mW power into the detector. This power converted to 2.42 mA current, and therefore a responsivity of $4.12\,\mathrm{A\,W^{-1}}$ for the detector was obtained.

It can be seen from Figure 5.11 that there is a small amount of variation in coupled power in-between stages.

The power lost (and gained) in dB can also be found for every stage, shown in Figure 5.12. As seen, the power lost in dB is not too large, and a final loss of just 2.8 dB was found after packaging and moving the package around after a few days. This is a relatively good result, considering the low cost and accessible nature of the process. Best results utilizing high-throughput automated tools and state-of-the-art pick-and-place tools and lithographic systems obtain a loss per facet of 0.5 dB in comparison [94]. Figures 5.14a and 5.14b demonstrate a finalized packaged chip, ready to be connected to a laser. A printed circuit board (PCB) could be incorporated below it and wire-bonded to make electrical connections easier.

While one-optical-port coupling was successful, two-port coupling was unsuccessful. Coupling with one optical port is considerably easier as the detector output is measured with the DC probes and ammeter, and only one fiber needs to be aligned. Coupling

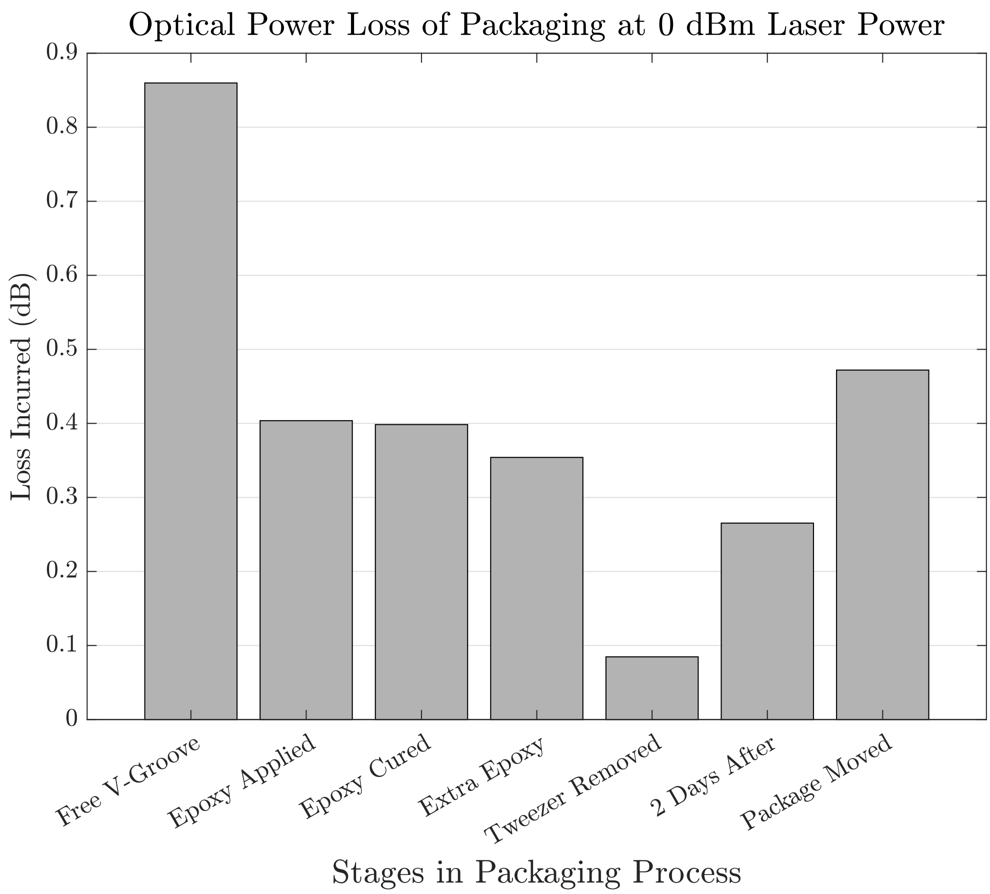

FIGURE 5.12: Optical power loss PIC at different stages.

is already complex with one optical input due to the inability to focus on both the waveguide and fiber at the same time, as described previously. This makes it more complex for two-way coupling, as one is blind to both. What was done during one-port coupling was to detect with the photodetector. Figure 5.13a shows a microscope camera side-view of the coupling process. One can see the glass and silicon, and the transition, but not the fiber itself. Looking at a diagonal view in Figure 5.13b, one can see that the V-groove dip (and therefore fiber itself) is slightly lower than the silicon-glass interface. This knowledge can therefore be used for easier determination of the correct z position. That being said, it was still extremely difficult to try to couple two fibers at a time. The issue is that light will tend to couple into the SiO_2 cladding rather than the waveguides themselves, and still yield a result. The optical power typically observed was approximately −30 dBm. A ring-resonator on a straight waveguide was used as a test PIC for coupling, if the ring is being coupled to, the correct waveguide was therefore coupled (and therefore one could see the ring's transmission spectrum at the detector end). Coupling was not possible after multiple attempts, with multiple different chips.

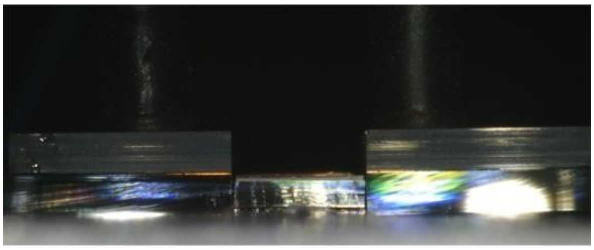

(A) Two-port coupling of a chip

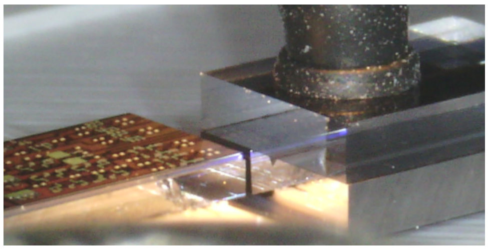

(B) Front of a V-groove assembly

FIGURE 5.13: Issues faced with V-grooves in 2-port coupling.

One final option could be to couple one optical port at a time, one could use an on-chip detector while coupling, as with the one-port process. This would necessitate a detector on the waveguide, with enough absorption to yield a photocurrent, but not enough to attenuate all the light so it reaches the other port. The coupling would necessitate the laser output to be switched from one fiber to another once one is aligned. This would also need fibers on both sides, and DC probes at the back, all with the microscope on top (and possibly the microscope camera at the front). This is a complex setup that requires ample space and planning. This was not possible to be arranged in the time of this project, but would be an interesting aspect of future work.

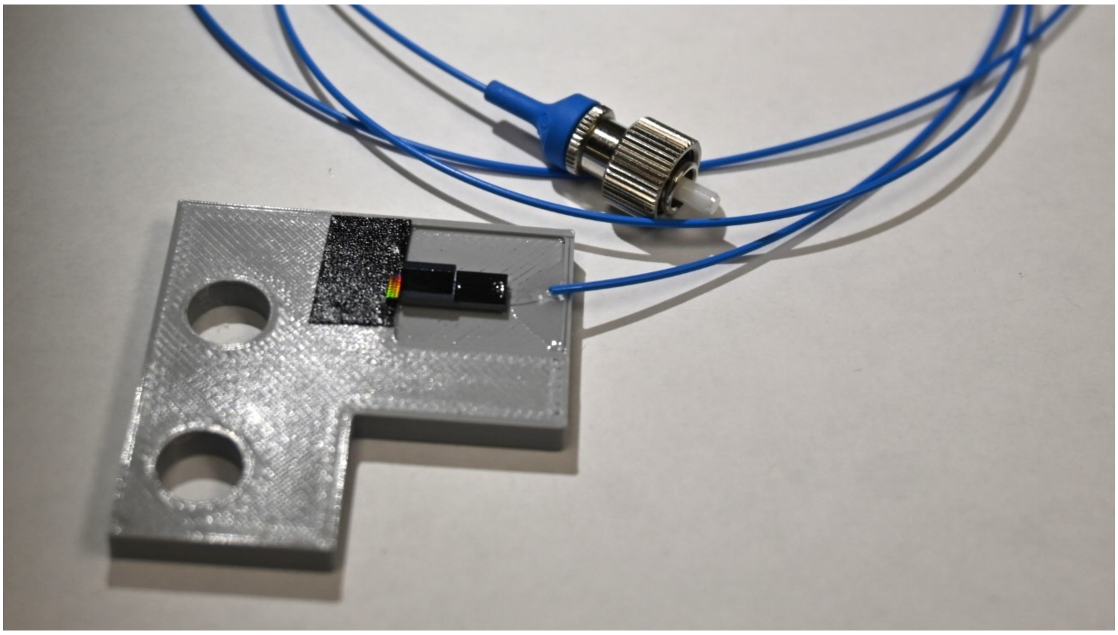

(a) Packaged chip with FC/PC connector

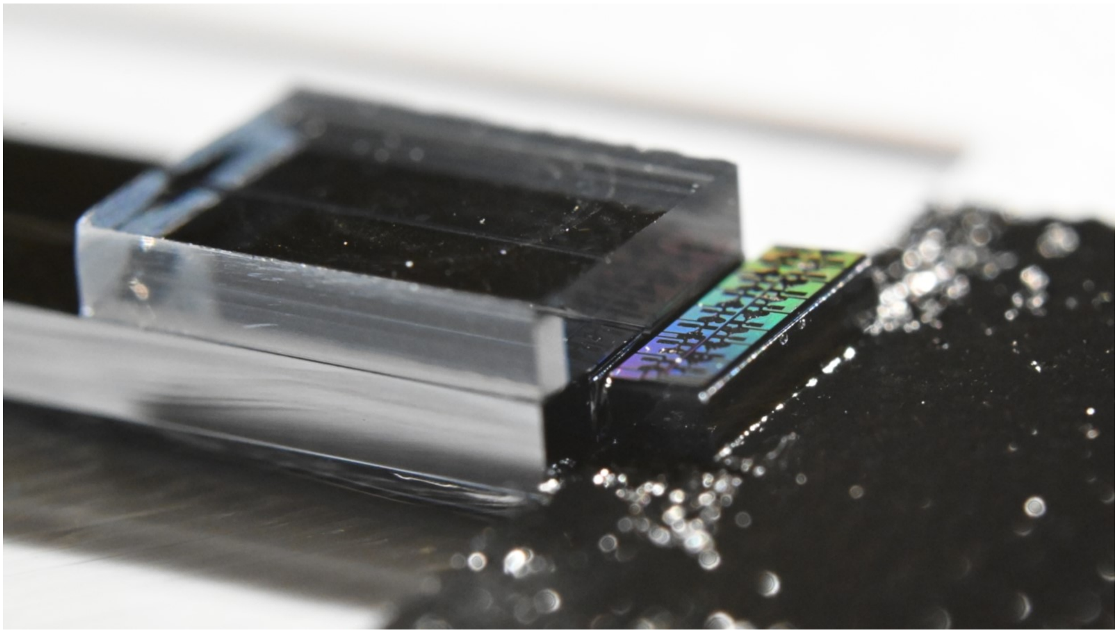

(b) Zoom in of chip and coupled fiber

Figure 5.14: First successful packaged PIC.

5.6 Electromagnetic Interference Cage

Shielding chips from radio frequency (RF) interference is non-trivial. To this end, RF enclosures, known as electromagnetic interference (EMI) shields are leveraged. Shielding can be expensive to implement, with many of the existing solutions utilizing solid metal boxes (often made of gold). We used 3D printing in this work to investigate cheaper solutions.

It is widely known that making a Faraday cage around a chip is sufficient to shield it from EMI, due to there being no electric field inside a cavity of a conducting material if no net charge is present [95]. This is why metal enclosures exist for most RF devices. It was hypothesized that a low-cost solution could be to make a metal enclosure with just enough metal to shield from EMI, but not enough to make it costly. The idea of skin depth δ is therefore introduced:

$$\delta = \sqrt{\frac{\rho}{\pi f \mu_0 \mu_r}} \tag{5.1}$$

dependent on material (resistivity ρ and permeability μ), and frequency f of the interference. The skin depth determines what thickness of conductive material (often material dependent) is needed to block $1/e$ of external EMI. Skin depths for common materials for are shown in Table 5.1. Therefore, the thickness of aluminum on an EMI shield, to protect from RF noise of 10 GHz and above, should be at least of 820 nm. This will only let 37% of noise penetrate, but two or three times the thickness would allow less, 13% and 5% respectively. The thickness can be set according to necessity.

Frequency (GHz)	Gold (nm)	Aluminum (nm)
10	753	820
20	533	580

TABLE 5.1: Skin depths of aluminum and gold at 10 GHz and 20 GHz.

Because an enclosure with a thickness of less than a micrometer would never be structurally sound, a base 3D printed box could be custom-made and then have conductive material deposited on it. This means that instead of a custom-made metal box being milled to size, one could create a plastic box with less than a micron of metal on top. Not only is the plastic light-weight and easy to prototype, it is incredibly inexpensive compared to a full-metal box. Deposition systems are often found in academic and research institutions, making this approach accessible.

To test the EMI shielding enclosure, an RF chip designed as a 10 GHz band-pass filter was used. The RF filter is a parallel coupled lines filter that utilizes a copper pattern with specific dimensions to only transmit certain frequencies. On either side was an SMA connector. Figure 5.15a shows the parallel coupled lines filter with SMA connectors, inside the enclosure. The 3D printed plastic enclosure closes and is secured by nuts and bolts, and the filter is held by extrusions within the enclosure. Such extrusions also alleviate stress on the SMA-filter soldering joint. The finalized closed package, connected, is shown in Figure 5.15b. Designing and 3D printing the enclosure was straightforward. Any gaps in the metal material (gap between top and bottom of enclosure, as well as gaps between connectors and opening for them) have an upper limit in size. In this circumstance, any gaps must be smaller than the wavelengths of the RF frequency of the EMI to effectively block them. This means, at 20 GHz, the smallest wavelength of EMI tested, has a wavelength of 1.5 cm. This is too large to give issues here.

Another challenge was the deposition itself. The sputter device used for deposition of the metal (in this case aluminum), did not necessitate high-temperature exposure for the package. Adhesion was found to be good enough, though it can be seen that in Figure 5.15b, there are flakes that fell away. This can be due to the small thickness applied, and the rough handling of the enclosure. This scaling is still smaller than the wavelength of RF waves used, so should not pose problems. The metal deposition was done on a spinning stage, mostly from above and sides. A challenge that can arise is that the metal would not equally distribute on the faces of the shield. Thus, higher thicknesses than

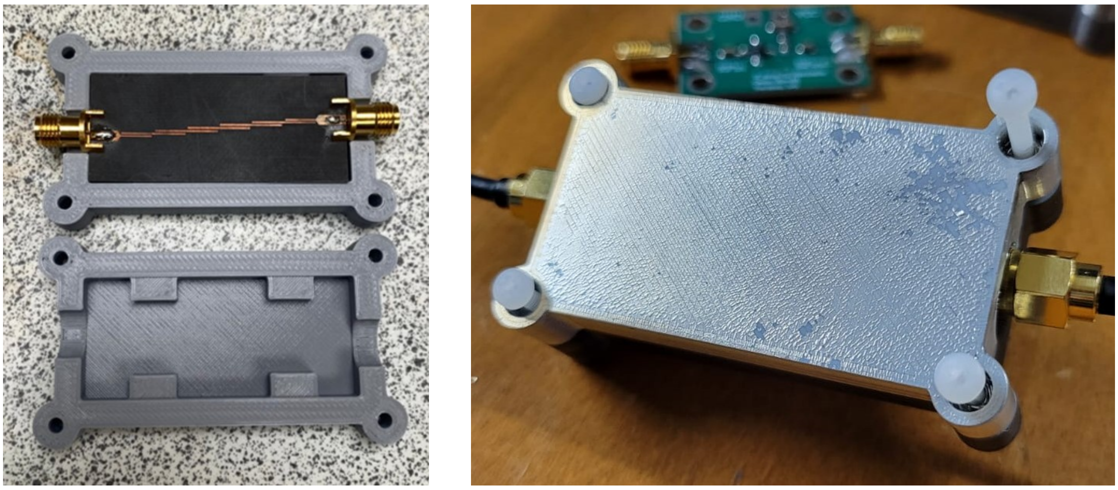

(A) Open enclosure (B) Connected closed enclosure

FIGURE 5.15: RF EMI enclosure.

designed should be deposited to make sure all sides have enough shielding material.

RF measurements were made with a vector network analyzer (VNA), the out-port was connected to the filter, and the other connector was connected to the in-port. A frequency sweep was performed, to see the performance of the filter. The same frequency sweep was performed using the enclosure. After this, the same measurements were made with an RF antenna aimed at the filter, and the measurements redone, without and with the enclosure again. The antenna was given a noise spectrum (mostly flat) between 3 GHz to 14 GHz, shown in Figure 5.16. The spectrum was collected from the out-port of a PNA Network Analyzer (Agilent E8363B) and then fed through an RF amplifier into the RF antenna.

Measurements are shown in Figure 5.17. These graphs show the RF transmission magnitude through the filter in dB scale, where the 0 dB reference is at the red line. The RF antenna EMI source was held on top of the filter at a constant distance for the measurements that used it. A specialized 3D printed structure was created to hold the antenna at a constant distance from the filter, as fluctuations in distance and position

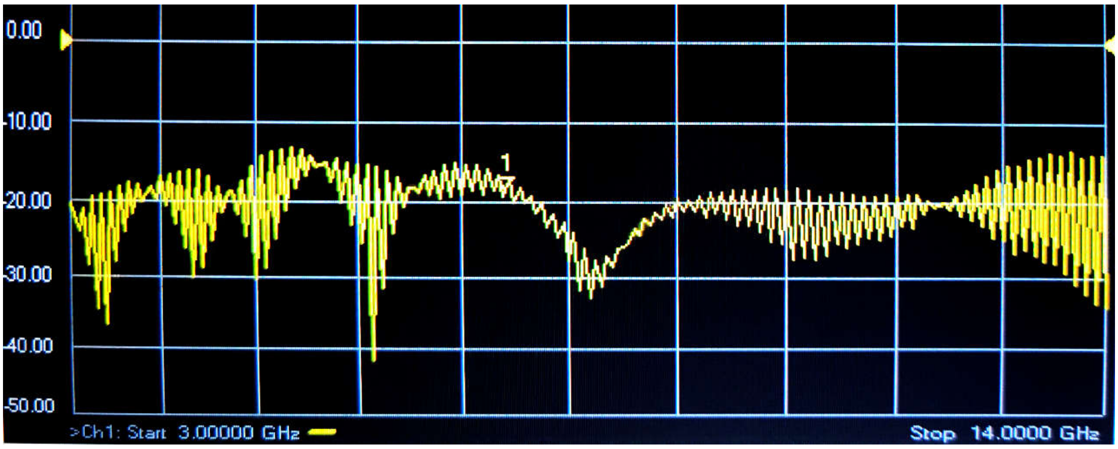

FIGURE 5.16: RF Input to the band-pass filter for measurements.

changed the RF spectrum dramatically.

As seen in Figure 5.17a, the spectrum of the original RF band-pass filter is quite pronounced, with a 3 dB bandwidth from roughly 7.5-11 GHz. The filtered-out regions sit at around −60 dB. Now comparing this to the spectrum of the same filter but with EMI shown in Figure 5.17b, it can be seen that the filtered regions (band rejection region) have been boosted by 10 dB. Furthermore, there seems to be a slight boost and dip in RF amplitude just before the start of the band-pass region, which can be attributed to the rise and dip in the EMI spectrum at that frequency range shown in Figure 5.16.

With the filter in an EMI shield, Figures 5.17c and 5.17d, with and without EMI applied, look almost identical in response. This is a very good result. It demonstrates that the shield is working by blocking out unwanted powerful external RF interference from the antenna. However, the spectrum is changed from the raw filter. It can be observed that the filtered regions are smoother, at times 5 dB higher than the original (10 dB higher at 13.5 GHz). The band-pass region is also less flat, with undulation happening in the dB scale. Causes for this could be that the metal shielding is too close to the filter itself and exhibiting coupling or inducing the RF signal from the parallel coupled lines from the filter. To solve this, a slightly wider enclosure could be built,

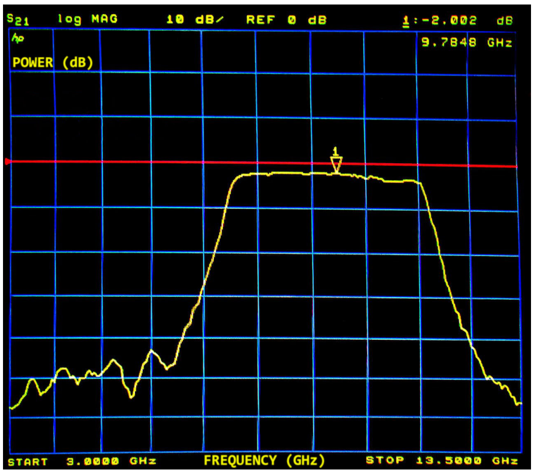

(A) No shield, no EMI

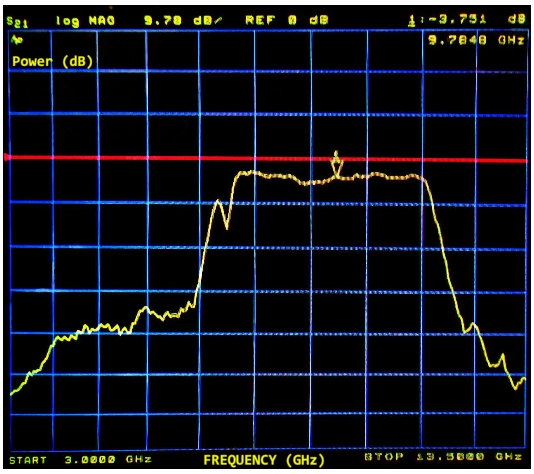

(B) No shield, with EMI

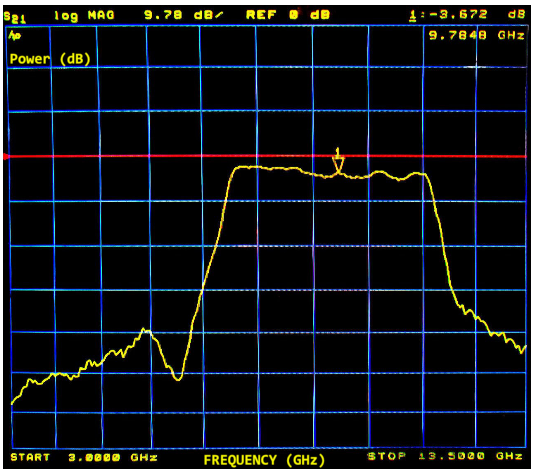

(C) With shield, no EMI

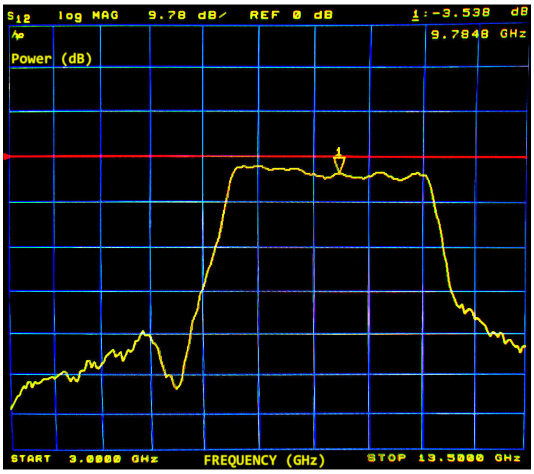

(D) With shield, with EMI

FIGURE 5.17: Spectra of RF filter with and without shield and EMI.

which would not change the fabrication process or cost at all.

5.7 Summary

A single optical input low-cost photonic packaging solution was designed and implemented using 3D printing that yielded a 2.8 dB coupling loss. A novel accessible enclosure for blocking RF EMI was created, which was able to block interference, but introduced interference of its own.

Chapter 6

Conclusion

6.1 Results

The main objective of this thesis was to design and fabricate processes and components for optical beamforming network (OBFN) on a chip, where a phased-array can be created. This involved designing components for the OBFN, including a time delay device and modulator, as well as creating a photonic packaging solution.

A ring modulator was simulated and measured for forward bias performance for better modulation depth. A somewhat linear performance was possible at 1.11 V forward bias, with a 3 dB bandwidth of about 500 MHz, and a modulation depth of 21 dB. The modulation wavelength was tested at multiple positions and found to work best at the blue side of the optical transfer function, with a modulation amplitude of 50 mV. A true time delay device was designed and tested. A heater on the optical ring resonator (ORR) was biased at different voltages to achieve variable group delay time at its output, enabling an on-chip OBFN. A maximum delay of 784 ps was achieved at 3.33 V bias, able to tune the delay to any amount under this value by changing bias.

A novel photonic packaging approach was developed using low-cost parts and leveraging 3D printing. A one-optical-in packaging solution was successful multiple times, and yielded a total power loss of 2.8 dB per facet when coupling. While this approach does not rival the 0.5 dB per facet loss from industrial packaging, it is extremely accessible and attainable by any research group looking to package a photonic integrated circuit (PIC). An electromagnetic interference (EMI) enclosure was also designed using 3D printing at low cost. The enclosure was successful at stopping EMI, but also introduced its own modification to the transmission of radio frequency (RF) power.

6.2 Suggested Future Work

The coupling power coefficient should change for the ring modulator in order to have critical coupling happen at a lower forward bias, and therefore enable higher bandwidths and better linearity of the response. The delay ring can be modified to produce a smaller amount of delay, the coupling power specifically. This smaller maximum delay would allow for better fine tuning of the delay itself.

For photonic packaging, the logical next step is to move forward with an optical-to-optical setup. The limiting factor is the ability to couple light into both input and output concurrently, as coupling just one input is much more feasible. To ease two-optical coupling, a detector can be embedded into the waveguide being coupled into, but this requires the chip to be custom-made for this setup. Another possibility is to change the whole setup, which can add complexity and cost. Furthermore, there can be work done to automate the procedure of alignment using c-mount cameras mounted on the microscope along with machine vision, reading data from the laser detector, and controlling the motorized xyz-stages. To solve issues where the RF shield modifies the transmission spectrum inside it, changes to the physical characteristics and dimensions of the enclosure can be tested.

Bibliography

[1] (2004) Fiber-Optic Technologies - A Brief History of Fiber-Optic Communications. Cisco Press. [Online]. Available: https://www.ciscopress.com/articles/article.asp?p=170740

[2] First Optical Transatlantic Cable TAT-8. IEEE Communications Society. [Online]. Available: https://www.comsoc.org/node/19856

[3] K. Kincade. ESnet Launches Next-Generation Network to Enhance Collaborative Science. Berkeley Lab. [Online]. Available: https://newscenter.lbl.gov/2022/10/11/esnet-launches-next-generation-network/

[4] Speedtest Global Index – Internet Speed around the world. Speedtest Global Index. [Online]. Available: https://www.speedtest.net/global-index

[5] G. Bennett. All You Ever Wanted to Know About Optical Transmission Bands. Infinera. [Online]. Available: https://www.infinera.com/blog/all-you-ever-wanted-to-know-about-optical-transmission-bands/tag/optical/

[6] M. Roser and H. Ritchie, "Moore's Law Transistor Count 1970-2020," 2020. [Online]. Available: https://commons.wikimedia.org/wiki/File:Moore%27s_Law_Transistor_Count_1970-2020.png

[7] A. Honardoost, K. Abdelsalam, and S. Fathpour, "Rejuvenating a Versatile Photonic Material: Thin-Film Lithium Niobate," *Laser & Photonics Reviews*, vol. 14,

no. 9, p. 2000088, 2020.

[8] A. Kitai. (2018) Principles of Solar Cells, LEDs and Related Devices: The Role of the PN Junction, 2nd Edition | Wiley. Wiley.com.

[9] Silicon nitride-based photonics. IMEC. [Online]. Available: https://www.imec-int.com/en/what-we-offer/development/system-development-technologies/Integrated-photonics/silicon-nitride-based-photonics

[10] D. Marpaung, J. Yao, and J. Capmany, "Integrated microwave photonics," *Nature Photonics*, vol. 13, no. 2, pp. 80–90, 2019.

[11] Cisco Annual Internet Report - Cisco Annual Internet Report (2018–2023) White Paper. Cisco. [Online]. Available: https://www.cisco.com/c/en/us/solutions/collateral/executive-perspectives/annual-internet-report/white-paper-c11-741490.html

[12] (2021) Silicon Photonics Market Size, Revenue Growth Drivers, Opportunities 2031. MarketsandMarkets. [Online]. Available: https://www.marketsandmarkets.com/Market-Reports/silicon-photonics-116.html

[13] What is the Bosch Process (Deep Reactive Ion Etching)? Samco Inc. [Online]. Available: https://www.samcointl.com/what-is-the-bosch-process-deep-reactive-ion-etching/

[14] B. E. Deal and A. S. Grove, "General Relationship for the Thermal Oxidation of Silicon," *Journal of Applied Physics*, vol. 36, no. 12, pp. 3770–3778, 1965.

[15] M. Bruel and B. A. Auberton-Hervé, "Smart-Cut: A New Silicon On Insulator Material Technology Based on Hydrogen Implantation and Wafer Bonding," *Japanese Journal of Applied Physics*, vol. 36, p. 1636, 1997.

[16] Y. A. Vlasov and S. J. McNab, “Losses in single-mode silicon-on-insulator strip waveguides and bends,” *Optics Express*, vol. 12, no. 8, pp. 1622–1631, 2004.

[17] L. Chrostowski and M. Hochberg, *Silicon Photonics Design: From Devices to Systems.* Cambridge University Press, 2015.

[18] J. J. Ackert, A. S. Karar, D. J. Paez, P. E. Jessop, J. C. Cartledge, and A. P. Knights, “10 Gbps silicon waveguide-integrated infrared avalanche photodiode,” *Optics Express*, vol. 21, no. 17, pp. 19 530–19 537, 2013.

[19] J. J. Ackert, D. J. Thomson, L. Shen, A. C. Peacock, P. E. Jessop, G. T. Reed, G. Z. Mashanovich, and A. P. Knights, “High-speed detection at two micrometres with monolithic silicon photodiodes,” vol. 9, no. 6, pp. 393–396, 2015.

[20] N. Margalit, C. Xiang, S. M. Bowers, A. Bjorlin, R. Blum, and J. E. Bowers, “Perspective on the future of silicon photonics and electronics,” *Applied Physics Letters*, vol. 118, no. 22, p. 220501, 2021.

[21] S. Fikar, R. Bogenberger, and A. L. Scholtz, “A 100GHz Bandwidth Matched Chip to PCB Transition Using Bond Wires for Broadband Matching,” in *2008 12th IEEE Workshop on Signal Propagation on Interconnects.* IEEE, 2008, pp. 1–4.

[22] E. Topak, J.-Y. Choi, T. Merkle, S. Koch, S. Saito, C. Landesberger, R. Faul, and K. Bock, “Broadband interconnect design for silicon-based system-in-package applications up to 170 GHz,” in *2013 European Microwave Conference.* IEEE, 2013, pp. 116–119.

[23] W. Heinrich, M. Hossain, S. Sinha, F.-J. Schmückle, R. Doerner, V. Krozer, and N. Weimann, “Connecting Chips With More Than 100 GHz Bandwidth,” *IEEE Journal of Microwaves*, vol. 1, no. 1, pp. 364–373, 2021.

[24] A. Noriki, I. Tamai, Y. Ibusuki, A. Ukita, S. Suda, D. Shimura, Y. Onawa, H. Yaegashi, and T. Amano, "Mirror-Based Broadband Silicon-Photonics Vertical I/O With Coupling Efficiency Enhancement for Standard Single-Mode Fiber," *Journal of Lightwave Technology*, vol. 38, no. 12, pp. 3147–3155, 2020.

[25] C. Wan, J. L. Gonzalez, T. Fan, A. Adibi, T. K. Gaylord, and M. S. Bakir, "Fiber-Interconnect Silicon Chiplet Technology for Self-Aligned Fiber-to-Chip Assembly," *IEEE Photonics Technology Letters*, vol. 31, no. 16, pp. 1311–1314, 2019.

[26] E. Berikaa, A. Janta-Polczynski, B. Sow, L. Xu, N. Liu, D. Deptuck, Y. Wang, C. Li, P. G.-Q. Lo, and D. V. Plant, "Net 67 Gbps Transmission Over 2 km at Sub 1 Vpp Using Packaged Silicon Photonic MZM," *IEEE Photonics Technology Letters*, vol. 34, no. 21, pp. 1139–1142, 2022.

[27] A. Janta-Polczynski, E. Cyr, R. Langlois, P. Fortier, Y. Taira, N. Boyer, and T. Barwicz, "Solder-Reflowable, High-Throughput Fiber Assembly Achieved by Partitioning of Adhesive Functions," in *2018 IEEE 68th Electronic Components and Technology Conference (ECTC)*. IEEE, 2018, pp. 1109–1117.

[28] Guide to 3D Printing in 2019: Types of 3D Printers, 3D Printing Materials, and Applications. Formlabs. [Online]. Available: https://formlabs.com/3d-printers/

[29] R. M. Stark, B. Lovelace, D. Dykes, K. Allen, B. Yang, A. Stark, and D. Brown, "Insertion Loss of 3D Printed Microspheres on Photonic Integrated Circuits," in *2019 IEEE Avionics and Vehicle Fiber-Optics and Photonics Conference (AVFOP)*. IEEE, 2019, pp. 1–2.

[30] M. Blaicher, M. R. Billah, J. Kemal, T. Hoose, P. Marin-Palomo, A. Hofmann, Y. Kutuvantavida, C. Kieninger, P.-I. Dietrich, M. Lauermann, S. Wolf, U. Troppenz, M. Moehrle, F. Merget, S. Skacel, J. Witzens, S. Randel, W. Freude, and

C. Koos, “Hybrid multi-chip assembly of optical communication engines by in situ 3D nano-lithography,” *Light: Science & Applications*, vol. 9, no. 1, p. 71, 2020.

[31] N. Lindenmann, G. Balthasar, D. Hillerkuss, R. Schmogrow, M. Jordan, J. Leuthold, W. Freude, and C. Koos, “Photonic wire bonding: A novel concept for chip-scale interconnects,” *Optics Express*, vol. 20, no. 16, pp. 17 667–17 677, 2012.

[32] K. Y. Park, M. I. M. Ghazali, N. Wiwatcharagoses, and P. Chahal, “Thick 3D Printed RF Components: Transmission Lines and Bandpass Filters,” in *2018 IEEE 68th Electronic Components and Technology Conference (ECTC)*, 2018, pp. 2186–2191.

[33] L. Hernandez, Y. He, A. Kaur, J. Papapolymerou, and P. Chahal, “Low-loss RF filter through a combination of additive manufacturing and thin-film process,” in *2017 IEEE Radio and Wireless Symposium (RWS)*. IEEE, 2017, pp. 114–116.

[34] K. Chizari, M. Arjmand, Z. Liu, U. Sundararaj, and D. Therriault, “Three-dimensional printing of highly conductive polymer nanocomposites for EMI shielding applications,” *Materials Today Communications*, vol. 11, pp. 112–118, 2017.

[35] J. Capmany and D. Novak, “Microwave photonics combines two worlds,” *Nature Photonics*, vol. 1, no. 6, pp. 319–330, 2007.

[36] K. Ogawa, H. Ishihara, K. Goi, Y. Mashiko, S. T. Lim, M. J. Sun, S. Seah, C. E. Png, T.-Y. Liow, X. Tu, G.-Q. Lo, and D.-L. Kwong, “Fundamental characteristics and high-speed applications of carrier-depletion silicon Mach-Zehnder modulators,” *IEICE Electronics Express*, vol. 11, no. 24, pp. 20 142 010–20 142 010, 2014.

[37] G. Li, A. V. Krishnamoorthy, I. Shubin, J. Yao, Y. Luo, H. Thacker, X. Zheng, K. Raj, and J. E. Cunningham, “Ring Resonator Modulators in Silicon for Interchip

Photonic Links," *IEEE Journal of Selected Topics in Quantum Electronics*, vol. 19, no. 6, pp. 95–113, 2013.

[38] S. Lischke, A. Peczek, J. S. Morgan, K. Sun, D. Steckler, Y. Yamamoto, F. Korndörfer, C. Mai, S. Marschmeyer, M. Fraschke, A. Krüger, A. Beling, and L. Zimmermann, "Ultra-fast germanium photodiode with 3-dB bandwidth of 265 GHz," *Nature Photonics*, vol. 15, no. 12, pp. 925–931, 2021.

[39] J. Capmany, I. Gasulla, and D. Perez, "Microwave photonics: The programmable processor," *Nature Photonics*, vol. 10, pp. 6–8, 2015.

[40] N. C. Harris, J. Carolan, D. Bunandar, M. Prabhu, M. Hochberg, T. Baehr-Jones, M. L. Fanto, A. M. Smith, C. C. Tison, P. M. Alsing, and D. Englund, "Linear programmable nanophotonic processors," *Optica*, vol. 5, no. 12, pp. 1623–1631, 2018.

[41] Y. Xie, Z. Geng, L. Zhuang, M. Burla, C. Taddei, M. Hoekman, A. Leinse, C. G. H. Roeloffzen, K.-J. Boller, and A. J. Lowery, "Programmable optical processor chips: Toward photonic RF filters with DSP-level flexibility and MHz-band selectivity," *Nanophotonics*, vol. 7, no. 2, pp. 421–454, 2018.

[42] G. Serafino, A. Bogoni, C. Porzi, S. Pinna, M. N. Malik, P. Ghelfi, J. Klamkin, A. D'Errico, and M. Puleri, "A beam-forming network for 5G systems based on precise optical clock and phase shifting," in *2016 International Conference on Optical Network Design and Modeling (ONDM)*. IEEE, 2016, pp. 1–4.

[43] M. Reza, A. Mohammad, G. Serafino, C. Roeloffzen, P. vanDijk, H. Mohammadhosseini, A. Abbasi, B. Desoete, and P. Ghelfi, "Design of an Integrated-Photonics RF Beamformer for Multi-Beam Satellite Synthetic Aperture Radar," in *2020 International Topical Meeting on Microwave Photonics (MWP)*. IEEE, 2020, pp.

87–90.

[44] A. B. Smolders, A. Dubok, N. M. Tessema, Z. Chen, A. Al Rawi, U. Johannsen, T. Bressner, D. Milosevic, H. Gao, E. Tangdiongga, G. Gerini, P. G. M. Baltus, M. Geurts, and A. M. J. T. Koonen, "Building 5G Millimeter-Wave Wireless Infrastructure: Wide-Scan Focal-Plane Arrays With Broadband Optical Beamforming," *IEEE Antennas and Propagation Magazine*, vol. 61, no. 2, pp. 53–62, 2019.

[45] L. Zhuang, C. G. H. Roeloffzen, A. Meijerink, M. Burla, D. A. I. Marpaung, A. Leinse, M. Hoekman, R. G. Heideman, and W. vanEtten, "Novel Ring Resonator-Based Integrated Photonic Beamformer for Broadband Phased Array Receive Antennas—Part II: Experimental Prototype," *Journal of Lightwave Technology*, vol. 28, no. 1, pp. 19–31, 2010.

[46] G. T. Reed and A. P. Knights, *Silicon Photonics: An Introduction.* Wiley, 2004.

[47] F. L. Pedrotti, L. M. Pedrotti, and L. S. Pedrotti, *Introduction to Optics*, 3rd ed. Cambridge University Press, 2017.

[48] AMF Silicon Photonics General-Purpose Fabrication Process. CMC Microsystems. [Online]. Available: https://www.cmc.ca/amf-silicon-photonics-general-purpose/

[49] Applied Nanotools (ANT) NanoSOI Fabrication Process. CMC Microsystems. [Online]. Available: https://www.cmc.ca/ant-nanosoi-fabrication-process/

[50] Single Mode Fiber. Thorlabs. [Online]. Available: https://www.thorlabs.com/newgrouppage9.cfm?objectgroup_id=949

[51] Adiabatic optical coupling. IBM Research Europe. [Online]. Available: https://www.zurich.ibm.com/st/photonics/

[52] A. La Porta, J. Weiss, R. Dangel, D. Jubin, N. Meier, J. Hofrichter, C. Caer, F. Horst, and B. J. Offrein, "Silicon photonics packaging for highly scalable optical interconnects," in *2015 IEEE 65th Electronic Components and Technology Conference (ECTC)*, 2015, pp. 1299–1304.

[53] H. C. Frankis, K. M. Kiani, D. Su, R. Mateman, A. Leinse, and J. D. B. Bradley, "High-Q tellurium-oxide-coated silicon nitride microring resonators," *Optics Letters*, vol. 44, no. 1, pp. 118–121, 2019.

[54] A. Meijerink, C. G. H. Roeloffzen, R. Meijerink, L. Zhuang, D. A. I. Marpaung, M. J. Bentum, M. Burla, J. Verpoorte, P. Jorna, A. Hulzinga, and W. vanEtten, "Novel Ring Resonator-Based Integrated Photonic Beamformer for Broadband Phased Array Receive Antennas—Part I: Design and Performance Analysis," *Journal of Lightwave Technology*, vol. 28, no. 1, pp. 3–18, 2010.

[55] R. L. Chao, J. W. Shi, A. Jain, T. Hirokawa, A. S. P. Khope, C. Schow, J. E. Bowers, R. Helkey, and J. F. Buckwalter, "Forward bias operation of silicon photonic Mach Zehnder modulators for RF applications," *Optics Express*, vol. 25, no. 19, pp. 23 181–23 190, 2017.

[56] A. Ayazi, T. Baehr-Jones, Y. Liu, A. E.-J. Lim, and M. Hochberg, "Linearity of silicon ring modulators for analog optical links," *Optics Express*, vol. 20, no. 12, pp. 13 115–13 122, 2012.

[57] R. B. Emmons, "Avalanche-Photodiode Frequency Response," *Journal of Applied Physics*, vol. 38, no. 9, pp. 3705–3714, 1967.

[58] D. F. Logan, P. E. Jessop, and A. P. Knights, "Modeling Defect Enhanced Detection at 1550 nm in Integrated Silicon Waveguide Photodetectors," *Journal of Lightwave Technology*, vol. 27, no. 7, pp. 930–937, 2009.

[59] J. Ackert, "High-speed silicon detector structures for photonic integrated circuits," Thesis, McMaster University, Hamilton, Ontario, Canada, 2015.

[60] Original Prusa MINI+. Prusa3D. [Online]. Available: https://www.prusa3d.com/category/original-prusa-mini/

[61] Autodesk Fusion 360. Autodesk. [Online]. Available: https://www.autodesk.ca/en/products/fusion-360/overview

[62] Autodesk Inventor Software. Autodesk. [Online]. Available: https://www.autodesk.ca/en/products/inventor/overview

[63] PrusaSlicer. Prusa3D. [Online]. Available: https://www.prusa3d.com/page/prusaslicer_424/

[64] UltiMaker Cura. UltiMaker. [Online]. Available: https://ultimaker.com/software/ultimaker-cura

[65] Advanced Micro Foundry. Advanced Micro Foundry. [Online]. Available: https://www.advmf.com/

[66] Applied Nanotools Inc. Applied Nanotools Inc. [Online]. Available: https://www.appliednt.com/

[67] R. Das, Y. Xie, H. Frankis, K. Chen, H. Rufenacht, G. Lamontagne, J. D. B. Bradley, and A. P. Knights, "Gain-enabled optical delay readout unit using CMOS-compatible avalanche photodetectors," *Photonics Research*, vol. 10, no. 10, pp. 2422–2433, 2022.

[68] Chetvorno, "Animation showing how a phased array antenna works," 2016. [Online]. Available: https://commons.wikimedia.org/wiki/File:Phased_array_animation_with_arrow_10frames_371x400px_100ms.gif

[69] S. Saeedi and A. Emami, "A 10Gb/s, 342fJ/bit micro-ring modulator transmitter with switched-capacitor pre-emphasis and monolithic temperature sensor in 65nm CMOS," in *2016 IEEE Symposium on VLSI Circuits (VLSI-Circuits)*, 2016, pp. 1–2.

[70] J. C. Rosenberg, W. M. J. Green, A. V. Rylyakov, C. L. Schow, S. Assefa, B. G. Lee, C. Jahnes, and Y. A. Vlasov, "Ultra-low-voltage micro-ring modulator integrated with a CMOS feed-forward equalization driver," in *2011 Optical Fiber Communication Conference and Exposition and the National Fiber Optic Engineers Conference*, 2011, pp. 1–3.

[71] J. Sun, R. Kumar, M. Sakib, J. B. Driscoll, H. Jayatilleka, and H. Rong, "A 128 Gb/s PAM4 Silicon Microring Modulator With Integrated Thermo-Optic Resonance Tuning," *Journal of Lightwave Technology*, vol. 37, no. 1, pp. 110–115, 2019.

[72] S. Han, S. Ji, I. Kang, S. C. Kim, and C. You, "Millimeter wave beamforming receivers using a Si-based OBFN for 5G wireless communication systems," *Optics Communications*, vol. 430, pp. 83–97, 2019.

[73] M. Kolawole, *Satellite Communication Engineering*, 2nd ed. CRC Press, 2016.

[74] K. Roush. The Dirty Little Secret About Ka vs Ku Frequencies. Honeywell. [Online]. Available: https://aerospace.honeywell.com/us/en/about-us/blogs/ka-band-vs-ku-band-the-difference-between-ku-and-ka

[75] S. Rungta, M. Ali, and B. Horner. (2020) Affordably Increase Network Bandwidth with Optics. Intel. [Online]. Available: https://www.intel.com/content/www/ca/en/it-management/intel-it-best-practices/affordably-increase-network-bandwidth-with-optics-brief.html

[76] A. Rahim, A. Hermans, B. Wohlfeil, D. Petousi, B. Kuyken, D. V. Thourhout, and R. G. Baets, "Taking silicon photonics modulators to a higher performance level: State-of-the-art and a review of new technologies," *Advanced Photonics*, vol. 3, no. 2, p. 024003, 2021.

[77] R. Dubé-Demers, J. St-Yves, A. Bois, Q. Zhong, M. Caverley, Y. Wang, L. Chrostowski, S. LaRochelle, D. V. Plant, and W. Shi, "Analytical Modeling of Silicon Microring and Microdisk Modulators With Electrical and Optical Dynamics," *Journal of Lightwave Technology*, vol. 33, no. 20, pp. 4240–4252, 2015.

[78] Lumerical CHARGE | 3D Charge Transport Solver. Ansys. [Online]. Available: https://www.ansys.com/products/photonics/charge

[79] Lumerical MODE | Optical Waveguide & Coupler Design Software. Ansys. [Online]. Available: https://www.ansys.com/products/photonics/mode

[80] Lumerical INTERCONNECT | Photonic Integrated Circuit Design Software. Ansys. [Online]. Available: https://www.ansys.com/products/photonics/interconnect

[81] J. A. delAlamo and R. M. Swanson, "Modelling of minority-carrier transport in heavily doped silicon emitters," *Solid-State Electronics*, vol. 30, no. 11, pp. 1127–1136, 1987.

[82] R. G. Hunsperger, *Integrated Optics*. Springer, 2009.

[83] B. Cao, D. J. S. Beckett, D. Logan, and J. Hauenschild, "Apparatus and method of resonance wavelength alignment for ring modulators," patentus 20 170 139 236A1, 2017.

[84] Y. Li, X. Song, Y. Xu, and Y. Li, "Spiral Optical Delay Lines in Silicon-on-Insulator," in *Asia Communications and Photonics Conference 2016*. Optica Publishing Group, 2016.

[85] M. R. Watts, J. Sun, C. DeRose, D. C. Trotter, R. W. Young, and G. N. Nielson, "Adiabatic thermo-optic Mach–Zehnder switch," *Optics Letters*, vol. 38, no. 5, pp. 733–735, 2013.

[86] G. Choo, C. K. Madsen, S. Palermo, and K. Entesari, "Automatic Monitor-Based Tuning of an RF Silicon Photonic 1X4 Asymmetric Binary Tree True-Time-Delay Beamforming Network," *Journal of Lightwave Technology*, vol. 36, no. 22, pp. 5263–5275, 2018.

[87] Lumerical FDTD | Simulation for Photonic Components. Ansys. [Online]. Available: https://www.ansys.com/products/photonics/fdtd

[88] P. O'Brien, L. Carrol, C. Eason, and J. S. Lee, "Packaging of Silicon Photonic Devices," in *Silicon Photonics III*, ser. Topics in Applied Physics, L. Pavesi and D. J. Lockwood, Eds. Springer, 2016.

[89] H. Lu, J. S. Lee, Y. Zhao, C. Scarcella, P. Cardile, A. Daly, M. Ortsiefer, L. Carroll, and P. O'Brien, "Flip-chip integration of tilted VCSELs onto a silicon photonic integrated circuit," *Optics Express*, vol. 24, no. 15, pp. 16 258–16 266, 2016.

[90] Photonic wire bonding. Vanguard Automation. [Online]. Available: https://www.vanguard-automation.com/photonic-wire-bonding-2/

[91] V-Groove Assemblies. OZOptics. [Online]. Available: https://www.ozoptics.com/ALLNEW_PDF/DTS0083.pdf

[92] FINEPLACER lambda 2. Finetech. [Online]. Available: https://www.finetechusa.com/products/finetech-product-overview/sub-micron-bonder-lambda2/

[93] Norland Ultraviolet Curing Adhesives | Optical, Electronic, and Lens Cold Blocking Adhesives. Norland Products. [Online]. Available: https://www.norlandprod.com/uvdefault.html

[94] T. Barwicz, T. W. Lichoulas, Y. Taira, Y. Martin, S. Takenobu, A. Janta-Polczynski, H. Numata, E. L. Kimbrell, J.-W. Nah, B. Peng, D. Childers, R. Leidy, M. Khater, S. Kamlapurkar, E. Cyr, S. Engelmann, P. Fortier, and N. Boyer, "Automated, high-throughput photonic packaging," *Optical Fiber Technology*, vol. 44, pp. 24–35, 2018.

[95] D. J. Griffiths, *Introduction to Electrodynamics*, 5th ed. Cambridge University Press, 2017.